Final Report

FHWA/IN/JTRP-2004/6

EVALUATION OF SURFACE (TOP DOWN) LONGITUDINAL WHEEL PATH CRACKING

By

Terhi K. Pellinen
Professor of Civil Engineering
School of Civil Engineering
Purdue University

Geoff Rowe
President
Abatech, Inc.

and

Kalapi Biswas
Graduate Research Assistant
School of Civil Engineering
Purdue University

Joint Transportation Research Program
Project No. C-36-31P
File No. 2-11-16
SPR-2788

Conducted in Cooperation with the
Indiana Department of Transportation
and the U.S. Department of Transportation
Federal Highway Administration

Purdue University
West Lafayette, Indiana
September 2004

TECHNICAL REPORT STANDARD TITLE PAGE

1. Report No.	2. Government Accession No.	3. Recipient's Catalog No.
FHWA/IN/JTRP-2004/6		

4. Title and Subtitle	5. Report Date
Evaluation of Surface (Top Down) Longitudinal Wheel Path Cracking	September 2004
	6. Performing Organization Code

7. Author(s)	8. Performing Organization Report No.
Terhi Pellinen, Geoff Rowe, Kalapi Biswas	FHWA/IN/JTRP-2004/6

9. Performing Organization Name and Address	10. Work Unit No.
Joint Transportation Research Program 1284 Civil Engineering Building Purdue University West Lafayette, IN 47907-1284	
	11. Contract or Grant No. SPR-2788

12. Sponsoring Agency Name and Address	13. Type of Report and Period Covered
Indiana Department of Transportation State Office Building 100 North Senate Avenue Indianapolis, IN 46204	Final Report
	14. Sponsoring Agency Code

15. Supplementary Notes

Prepared in cooperation with the Indiana Department of Transportation and Federal Highway Administration.

16. Abstract

The research involved evaluating three surface cracked pavements during 2002 and 2003. A 500m section of I-65 North of Lafayette was chosen as the first site (designated as Site 1), an I-65 section in downtown Indianapolis was the second site (Site 2), and US-421 in Madison was the third site (Site 3). Site 1 had 11-year old pavement, Site 2 had 12-year old pavement and Site 3 had 4.5-year old pavement. All these sites exhibited longitudinal wheel path cracking which was later identified as top-down cracking. All sites had excellent structural capacity indicating that the top-down cracking was confined in the pavement surface. This was confirmed by visual inspection of cores. The causes for top-down cracking in the surface layer were identified as follows: 1) non-uniformities in the material properties caused by construction practices such as segregation; 2) high in-situ air void content; 3) low amount of fines in mixtures, and 4) aging of binder. However, the study was not able to identify/verify any structural causes for top-down cracking.

17. Key Words	18. Distribution Statement
top-down cracking, binder stiffness, structural capacity, segregation, mix stiffness, modeling.	No restrictions. This document is available to the public through the National Technical Information Service, Springfield, VA 22161

19. Security Classif. (of this report)	20. Security Classif. (of this page)	21. No. of Pages	22. Price
Unclassified	Unclassified	161	

Form DOT F 1700.7 (8-69)

AKNOWLEDGEMENTS

The authors wish to acknowledge Ms. Haleh Azari at Federal Highway Turner Fairbank Research Center for her help in scanning the cracked cores using X-ray tomography. The authors also wish to acknowledge the computation work conducted by Mr. Mark Sharrock for the development of the routines and software used to produce these results and Dr. Ayesha Shah for the laboratory testing conducted at the North Central Superpave Center and Dr. Khaled Galal at Indiana Department of Transportation, Research Division. Also, the Study Advisory Committee members, Mr. Lee Gallivan, Federal Highway Administration, Mr. David Andrewski, Indiana Department of Transportation, Materials and Tests, Mr. Gerry Huber, Heritage Research Group, and Dr. Khaled Galal, Indiana Department of Transportation, Research Division for their valuable advice during the course of the research.

TABLE OF CONTENTS

LIST OF TABLES

LIST OF FIGURES

1 INTRODUCTION

1.1 Background

Surface-initiated longitudinal wheel path cracking in asphalt pavements, Figure 1, has been reported as a widespread mode of failure in asphalt concrete pavements. It is a phenomenon that has recently attracted a large amount of interest and very few theories have been presented so far that fully explain the phenomenon of the top-down cracking mechanism. Studies performed by various researchers have shown that the existing design and evaluation methods that use average conditions are inadequate for predicting this type of surface cracking. The mechanisms controlling surface cracking are related to the fracture properties of the asphalt mixture loaded by traffic and climate. Work in recent years has suggested several theories for understanding these mechanisms. However, additional studies of in-situ pavements are needed to develop a complete understanding of the top-down cracking phenomenon to develop better rehabilitation guides for these pavements.

Figure 1: Surface cracked major interstate highway (I-65 North) in Indiana.

1.2 Problem Statement

The maintenance need of cracked highway structures has relied upon bottom-up mechanistic design models for asphalt pavements. A badly cracked pavement will normally require a major maintenance program involving the removal and reconstruction of the highway. However, the repair of top-down cracked pavements can generally be confined to the replacement of the upper portion of the pavement structure with new materials. The correct identification of the type of cracking that is occurring in pavements will consequently make a significant impact upon the cost of rehabilitation of pavement sections. In addition, the selection of materials for the top-down cracked pavement is likely to be significantly different from those considered for deep, thick asphalt pavement sections.

1.3 Objective of the Study

The objective of the study was to evaluate top-down cracked pavements and assess their structural capacity as well as study in-place materials to propose the best identification of distress type, material selection, and rehabilitation methods to be used in Indiana.

1.4 Scope of Research

This research was primarily concerned with the formulation of a preliminary rehabilitation plan for top-down surface cracked pavements. The scope of the research was to identify sites in Indiana that exhibit surface top-down cracking and evaluate their condition, see Figure 2. From these sites, three particular sites exhibiting the top-down surface cracking distress on longitudinal wheel path were selected for further evaluation in the study. The evaluation included the structural response of the pavement section and analysis of material properties. Based on this evaluation a preliminary rehabilitation plan

for top-down surface cracked pavements was formulated. Based on findings of this research, a more comprehensive study plan will be developed if needed.

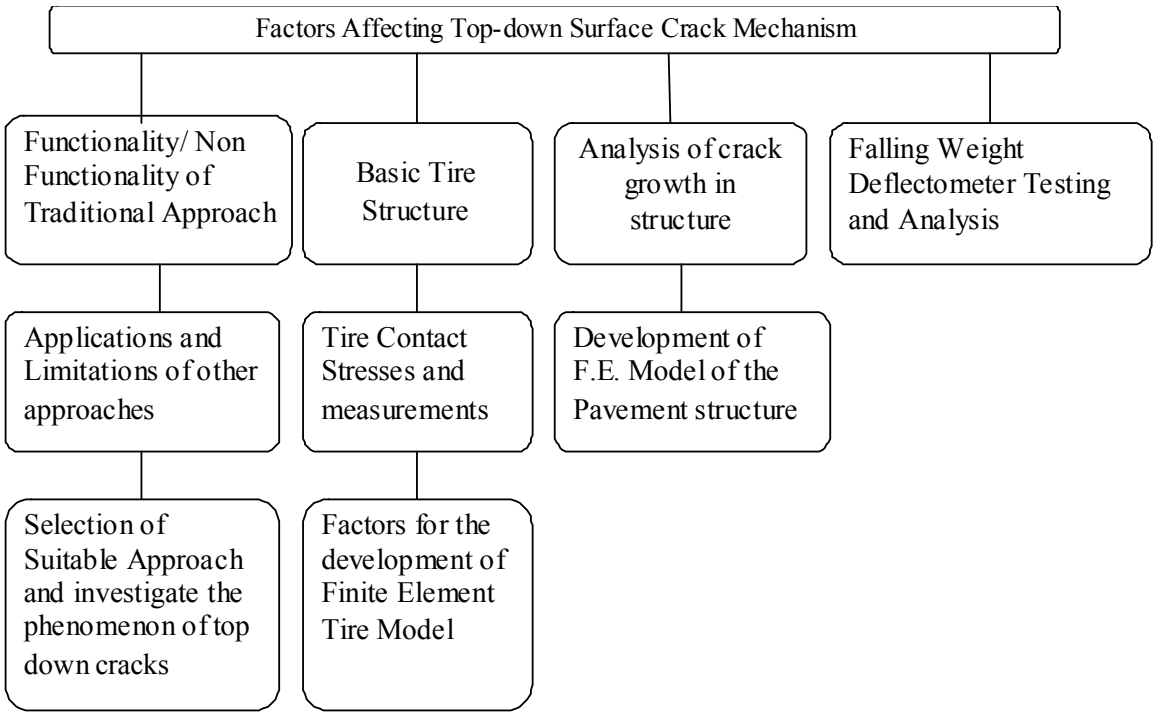

Figure 2: Flow Chart of Research Approach and Literature Review

2 LITERATURE REVIEW OF TOP-DOWN CRACKING

Mechanistic pavement design has historically relied upon engineering assumptions that include the use of a wheel load modeled by a uniformly loaded contact patch (or multiple patches) and a single modulus value assigned to an asphaltic layer in pavement design (Brown & Brunton, 1985; Shell International Petroleum Company, 1978). These assumptions are considered reasonable when determining stresses and strains at the underside of the pavement layers away from the loading points. Therefore, the current mechanistic-empirical pavement methods are based on the tensile strains at the bottom of asphalt layers to prevent bottom-up fatigue cracking and compressive strains at the top of the subgrade to prevent subgrade rutting. However, when trying to determine the pavement response close to the wheel loads this type of analysis will be incapable of capturing the effects of temperature depth gradients within the pavement structure and the effect of complex tire-pavement interactions. The analysis of these last two aspects is considered to be a key component to the understanding of the surface cracking phenomena similar to the surface rutting mechanisms in the asphalt pavements.

However, there are different views among researchers whether the surface cracking phenomena is caused only by the pavement surface stresses, as discussed above, or whether the pavement structure plays some role in the top-down cracking formation. Nevertheless, items that have been associated to the surface cracking phenomena include: 1) pavement tire loading such as load magnitude and tire type effects; 2) pavement temperature and temperature gradients; 3) asphalt binder and mix aging; 4) pavement structure; 5) mix properties and raw materials used; and 6) issues related to the construction such as segregation of mix.

2.1 Top-down Cracking Phenomenon

Top-down cracking in asphalt pavements initiates from the top and propagate downwards through the asphalt concrete layer over time. Svasidisant, Schorsch and Baladi

(2002) have defined three categorizers for the top-down cracking. In the first stage single short longitudinal cracks appear just outside the wheel path in the pavement surface. Over time the cracking reaches a second stage where the short longitudinal cracks grow longer and sister cracks develop parallel to and within 0.3 to 1.0 meters from the original cracks. At the third stage the parallel longitudinal cracks are connected via short transverse cracks.

Also, Myers, Roque and Ruth (1998) report the location of surface cracks being just outside the wheel path and the cracks penetrate to depths ranging from just under pavement surface to the entire depth of asphalt layer.

The Federal Highway Administration (FHWA) Accelerated Loading Facility (ALF) study (Stuart, Mogawer & Romero, 2001) for bottom-up fatigue cracking showed that the transverse bottom-up cracking started in the wheel path area. Longitudinal top-down cracks occurred at the outer edges of the wheel paths where the surface of the pavement has a high curvature. Also fatigue cracks were smaller at 28°C than at 19 and 10°C, indicating how crack propagation changes with temperature.

The time interval for the cracks to appear seems to be very versatile ranging from one year to five years. The study by Svasidisant et al. (2002) shows that surface cracks had propagated through all asphalt layers in a 15 year old pavement with rubblized base. In pavements with the same base structure but only 9 to 10 years old, surface cracks had propagated 100% through the surface layers but only about 50% and 20% through the intermediate and base layers, respectively.

2.2 Pavement Loading and Tire Effects

For the analysis of surface cracking, it is believed that lateral stresses initiate cracking at the pavement surface which somehow propagates downwards. These cracks are neither of the traditional fatigue nor reflective nature. Hugo and Kennedy (1985) attributed cracks to the presence of horizontal shear stresses induced on the pavement surface. Analytical work by Kunst (1990) illustrated how inward radial horizontal stresses could lead to tension at the edges of circular load.

Jacobs (1995) described the occurrence of maximum tensile stresses at the surface of the pavement through analytical evaluation and predicted tensile stresses at the edge of a truck tire on the pavement surface, which were sufficient to cause fracture. The tensile stresses were found to dissipate rapidly with increasing depth; i.e., they existed in the top 10 mm of the asphalt layer. Tensile stresses were generated at the edge of tire load because measurements were obtained from a bias ply truck tire.

Myers (2000) stated that longitudinal surface cracking appears to be initiated by significant tensile stresses (Mode I tensile failure) that are induced under radial truck tires. Thermal stresses contribute to the initiation mechanism as a secondary factor.

Research stated that cracks advance only in critical conditions. The mechanism of crack development is highly dependent of load spectra (magnitude and position) and differential pavement temperature gradients and pavement structure. Tensile stresses were found to be more significant in thicker and stiffer asphalt concrete pavements. Therefore the mill and fill rehabilitation technique may be more suitable to prevent surface cracking than overlay. However, use of a linear elastic layer analysis did not allow for analysis of crack growth or discontinuities in the pavement.

Myers (2000) also explained that the tire structure has significant influence on contact stresses. The stress state induced by radial or wide base radial tires were determined to be potentially more detrimental to pavement surface than the stress state induced by bias ply tires.

There are distinct differences in the fabrication of radial and bias-ply tires. In bias-ply tires, the air container is made from crisscrossing layers of rubberized fabric and in radial tires it is formed by radially running plies of rubberized cord or steel cord on commercial vehicle tires.

2.3 Temperature Depth Gradients

Temperature effects in asphaltic materials have very significant effects on the stiffness of the asphalt layers. The pavement structure will experience a wide range of

temperatures as a function of the daily and annual variation of temperature/climate. Climatic effects models can be used to predict the in-situ pavement temperatures. These models have been calibrated against real pavements and can be considered reasonably accurate.

In work conducted by Rowe, Sauber, Fee and Soliman (2001) it has been shown that by using layered elastic analysis and a uniform distributed load it is possible to compute significant tensile stress at the surface of the pavement adjacent to the wheel loading when temperature depth gradients are considered. Consequently, the use of proper temperature-depth information is also considered of prime importance as the correct definition of tire loading.

A paper by Svasidisant et al. (2002) reports 30°C diurnal temperature difference between the asphalt surface and base course during daytime and 10°C temperature difference during nighttime. These temperature differences cause differential stiffness values in the asphalt pavement.

Schorsch et al. (2001) report that negative temperature differences which are consistent of evening and nighttime temperatures produce the highest surface tensile stresses in the pavement. They also recommend that to prevent the effects of nighttime temperatures, the asphalt base course should be designed at higher stiffness than the asphalt surface course.

Usually it is expected for bottom-up cracking that thin pavements (<150 mm) are in strain control thus requiring softer binder and mix to prevent fatigue, and thick pavements (>150mm) are in stress control requiring stiffer binder and mix to prevent cracking. However, the FHWA-ALF study (Stuart et al. 2001) concluded that mixtures were most of the time in stress control regardless of the depth of the pavement structure and most of the cracking happened in the intermediate 19°C temperature and not in 28° or 10°C. Also, the model of loading changed from strain to stress for 100 mm pavement with a change in temperature from 28 to 19°C.

2.4 Pavement Structure

Structural issues affecting pavement age are more controversial. The study done by Matsuno and Nishizawa (1991) concluded that pavement cross section had little effect on high tensile strains that developed to the pavement surface due to the soft asphalt mix. They attributed to the top-down cracking caused by the mix properties at pavement surface. They concluded that in one to five year old pavements high tensile strains in hot pavement surface were causing cracking because at shadowy areas the cracking was absent. Also, Myers et al. (1998) have concluded that the pavement structure had little to do with the surface tensile stresses initiation, and surface cracking was caused by high tensile stresses generated at pavement surface by the radial truck tires. However, Myers (2000) concludes the pavement structure affects crack propagation.

In a study by Uhlmeyer et al (2000) three to eight year old pavements which were more than 160 mm (6.3 in) thick exhibited top-down cracking in and around the wheel paths. They concluded that the pavement thickness has an effect on the surface cracking initiation which contradicts the previous findings.

Svasidisant et al. (2002) studied asphalt overlays on top of rubblized concrete slabs. They concluded that differential stiffness differences in the asphalt pavement surface and base layers could result in significant tensile stresses at the pavement surface. The magnitude of the surface tensile stresses increases as:

- Ratio of asphalt surface course to the base course moduli increases
- Base layer moduli increases such as stabilized or rubblized base
- Thickness of the asphalt layer increases in pavements with conventional aggregate base

They also found that the quality of the rubblization process has a direct impact on the modulus of the rubblized layer which can vary from 200 to 13,000 MPa. The mechanistic analysis results also suggest that the rubblized layer underneath the asphalt layer may cause top-down cracking, although it reduces the rutting and bottom-up cracking potential.

2.5 Aging

The aging of asphalt binder has been attributed to be the major cause of top-down cracking in many studies such as Hugo & Kennedy (1985) in South Africa, Wambura et al. (1990) in Kenya, and Gerritsen (1987) in Netherlands. In South Africa and Kenya, severe age hardening occurred in two year old pavements that had high air void content, in this case around 8%. In Kenya the severe age hardening happened in the top few millimeters of the asphalt pavement surface. Studies in Netherlands (Gerritsen, 1987) also report severe age hardening of newly constructed pavement surface that was not properly compacted and also had low binder content.

2.6 Mix Composition and Raw Materials

Harvey and Tsai (1996) studied the effects of asphalt and air void content on mix fatigue and stiffness. The variables in the fatigue study were: one aggregate and asphalt source, five asphalt contents ranging from 4 to 6%, and three air void contents ranging from 1 to 3%, 4 to 6% and 7 to 9%. The test used was third-point controlled strain flexural beam test developed under the SHRP research program. A 10 Hz haversine wave was used and testing was carried out at 19°C (66°F) temperature. Two strain levels were used (300 and 150 micro-strains) with average fatigue life of 50,000 and 500,000 repetitions, respectively. They concluded that the results clearly indicate that the low air void content increased fatigue life and mixture stiffness. Increased asphalt content increased fatigue life and decreased stiffness.

Micromechanics study of top-down cracking by Myers, Mohammad and Fu (2003) state that rutting and cracking may be related and bottom-up and top-down cracking may not be the only patterns of cracking. They predicted tensile stresses inside the pavement below surface which is consistent to top-down cracking predicted by FEM analysis. Cracking took place at a higher temperature where rutting is usually assumed to be dominant. This finding can be supported by the findings by Matsuno and Nishizawa (1991)

who concluded that surface cracking took place at higher pavement temperatures.

The WesTrack experiment (Tsai, Harvey & Monismith, 2001) indicated that fine and fine-plus mixtures were less prone to bottom-up cracking than coarse graded mixtures. A study by Pellinen, Christensen, Rowe, and Scharrok (2004) suggests that the mix volumetric property that best correlated to the cracking in the WesTrack experiment was Voids Filled with Asphalt (VFA), although the correlation was at best moderate. Mixtures that had VFA above 53% had less cracking than mixtures with VFA below the average. The other volumetrics for crack resistant mixtures were $Vb_{eff} > 9\%$, air void content < 6%, and Voids in mineral Aggregate (VMA) < 14%.

Based on the report by the independent WesTrack evaluation group, "*Performance of Coarse Graded Mixes at WesTrack - Premature Rutting*" (FHWA Final Report, 1998), the mixture performance at WesTrack was different than typically seen on other high truck traffic pavements. Coarse mixtures cracked during the winter months and then rutted during the summer months. Evaluators noted that usually pavements that exhibit fatigue cracking do not exhibit significant plastic deformation. Also, the fatigue cracks developed first in the transverse direction and then in the longitudinal direction. They noted that usually, longitudinal cracks are the first sign of fatigue, followed by the transverse cracks (which indicates top-down cracking pattern).

2.7 Construction Issues

The construction issues have been reported to affect the formation of surface cracks. Surface defects can cause surface cracking based by Uhlmeyer et al. (2000). A study by Schorsch et al. (2001) found that surface cracks initiated from the segregate pavement areas. They conducted field and laboratory tests to quantify the segregation using nuclear gauge measurements to identify the air void differences in the segregated and non-segregated areas. Laboratory measurements included indirect tensile strength, gradation, and binder content measurements to verify segregation. Unfortunately loading time or test temperature was not reported for comparisons. Segregated spots had lower tensile strength

than non-segregated areas.

A poor pavement compaction has been cited as a source of surface crack initiation and propagation in pavements in several studies discussed above. Based on the research conducted in Africa, air void content around 8% was considered poor, while this is the typical required in-situ air void content in the U.S. The European mix design and construction specifications tend to require lower design and in-situ air void contents. For instance, in Finland the required in-situ air void content of the mix (measured using dry method) is less than 5% to prevent aging and moisture damage in the mix (PANK,1995).

Schorsch et al. (2001) found that in segregated pavements the air void content varied between 1.8 to 12%. The average air void content of the segregated pavements was 6.1% with standard deviation of 2.8%. The non-segregated control sections had an average of 3.8% air void with standard deviation of 2%. The highest measured air void content in the control cores was 8.1%. This suggests that the low air void content provides better resistance against cracking.

Based on the literature it can be concluded that the air void threshold for better performing mixtures seems to be less than 6%.

3 COLLECTION AND ANALYSIS OF SITE DATA

3.1 Site Selection

Several candidate pavement sites were evaluated based on visual survey and site inspections. The pavement sites that were selected for inspection were checked for the following factors: 1) pavement structure consisting of only unbound and asphaltic bound layers; 2) pavement with relatively heavy traffic; 3) pavements with minimal rutting; 4) materials used for the pavement to be typical for the state; and 5) thickness of the asphalt layers greater than 200 mm (8 inches).

Based on the preliminary visual survey and site inspection, three sites were selected for further evaluation. These three sites were:

1. Site 1- I-65 North of Lafayette, County: Jasper, District: La Porte
   Mile Post: 224-223
   Lanes/Direction: 2/ South Bound Lane
   Construction Let Date: January 12, 1993, pavement age 11 years
2. Site 2- I-65 Near Indianapolis, County: Marion, District: Greenfield
   Mile Post: 115/6
   Lanes/Direction: 3/ South Bound Lane
   Construction Let Date: November, 1992, pavement age 12 years
3. Site 3- US-421 Madison, County: Jefferson, District: Seymour
   Mile Post: 2
   Lanes/Direction: 2/ North Bound Lane
   Construction Let Date: May 18, 1999, pavement age 4.5 years

Based on the preliminary visual inspection, the I-65 North site had longitudinal cracking in the middle of the lanes and some wheel path cracking in all lanes for both directions. Cracks had been sealed with asphalt. The selected test section was in the south

bound lane between mileposts 224 and 223. The exact location was after the Ferry Oak Street bridge (looking from the north).

The I-65 Loop site had longitudinal and some low severity alligator cracking in all 6 lanes for both directions. The selected test area was in the south bound lane before the Martin Luther King Exit starting from milepost 115+6 after the Exit 115 sign.

US-421 in Madison had longitudinal outer wheel path cracking in the driving lane on upgrade in the north bound direction that had slower traffic. However, no cracking in the downhill direction where the traffic speed is higher was observed. Also in this site cracking was concentrated on the fill areas. Two possible coring locations, 1 & 2, were marked on the pavement in the northbound driving lane.

Table 1 summarizes the pavement structure for the sites selected for the top-down crack study. The design thickness of the pavement layers and the materials for each site were obtained from the INDOT database. The asphalt mix in the I-65 North and US-421 Madison site were constructed over rubblized concrete while the I-65 Loop near Indianapolis was constructed over granular base material. The overall design thickness for HMA for Site1, I-65 North, was 370 mm (14.5 inch), for Site 2, I-65 Loop, was 545 mm (21.5 inch), and for Site 3, US-421 Madison, was 200 mm (8 inch).

Location of the survey sites are marked on the Indiana map in Figure 3. The exact locations of the three selected sites are shown in the detailed maps in Figure 4, Figure 5, and Figure 6. These sites were subjected to detailed pavement evaluations.

Table 1: Design thicknesses for the study sites

SITE 1 I-65 NORTH OF LAFAYETTE			
LAYER NO	**DESIGN THICKNESS (in)**	**(mm)**	**DESCRIPTION**
1	1.5"	38.10	HMA Surface
2	13"	330.2	HMA Base
3	10"	254.0	Rubblized Concrete
4	6"	152.4	SubgradeTreatment Type 2

I-65 LOOP NEAR INDIANAPOLIS			
LAYER NO	**DESIGN THICKNESS (in)**	**(mm)**	**DESCRIPTION**
1	1"	25.40	60 kg/m^2 Bituminous Surface 11HV
2	3"	76.20	180 kg/m^2 Bituminous Binder 8 or 9 HV
3	14"	355.6	687.27 kg/m^2 Bituminous Base 2 HV
4	3.5"	88.90	218.18 kg/m^2 Bituminous Base 5D
5	12"	304.8	Compacted Aggregate Type O
6	6"	152.4	Subgrade Treatment Type O

US-421 MADISON SECTION			
LAYER NO	**DESIGN THICKNESS (in)**	**(mm)**	**DESCRIPTION**
1	1.25"	31.75	75 kg/m^2 HMA Surface 9.5mm
2	2.75"	69.85	165 kg/m^2 HMA Intermediate 19mm
3	4"	101.6	240 kg/m^2 HMA Base 25mm
4	9"	228.6	Rubblized Concrete
5	6"	152.4	Subgrade Treatment Type 2
60 kg/m^2 = 110 lb/syd			

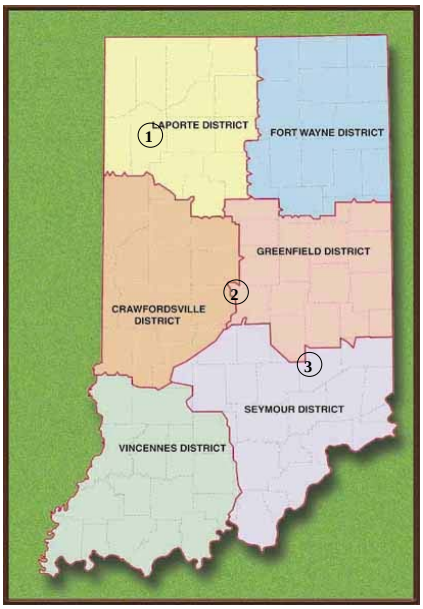

Figure 3: Map of Indiana with selected study sites

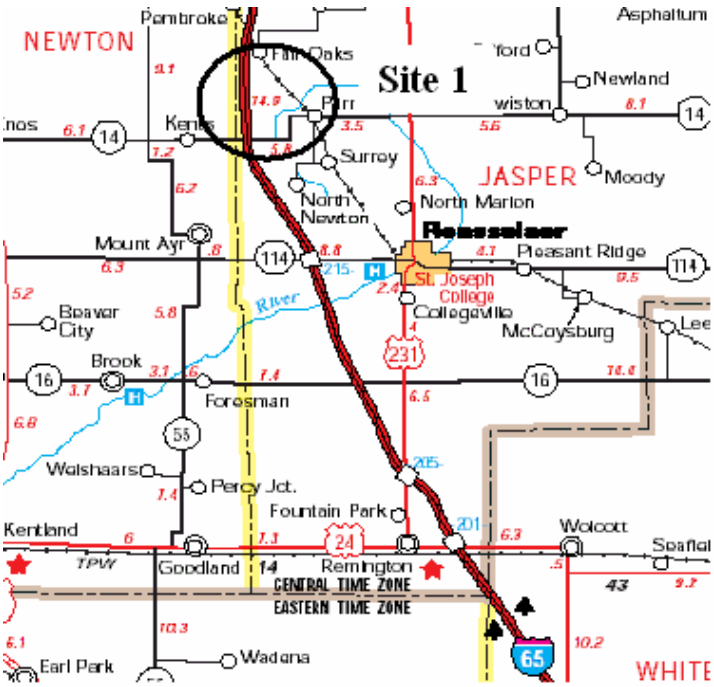

Figure 4: SITE 1 I-65 North of Lafayette

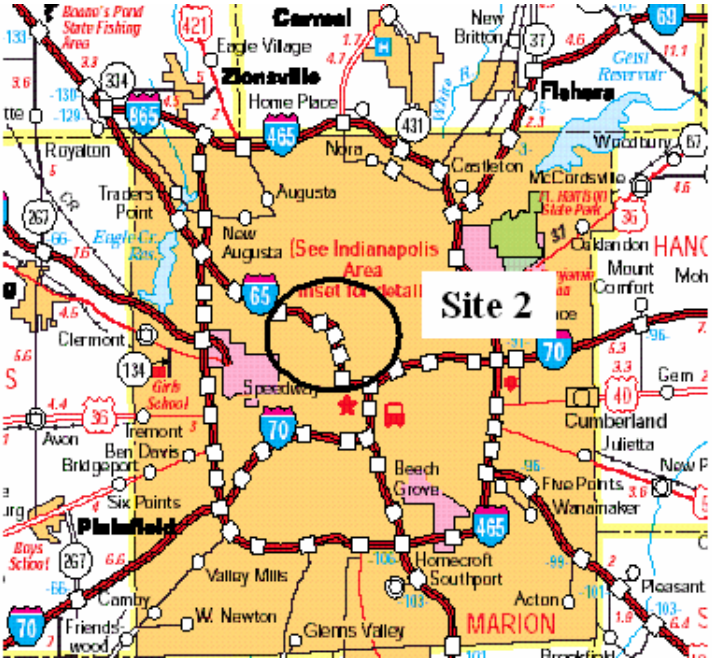

Figure 5: SITE 2 I-65 Near Indianapolis

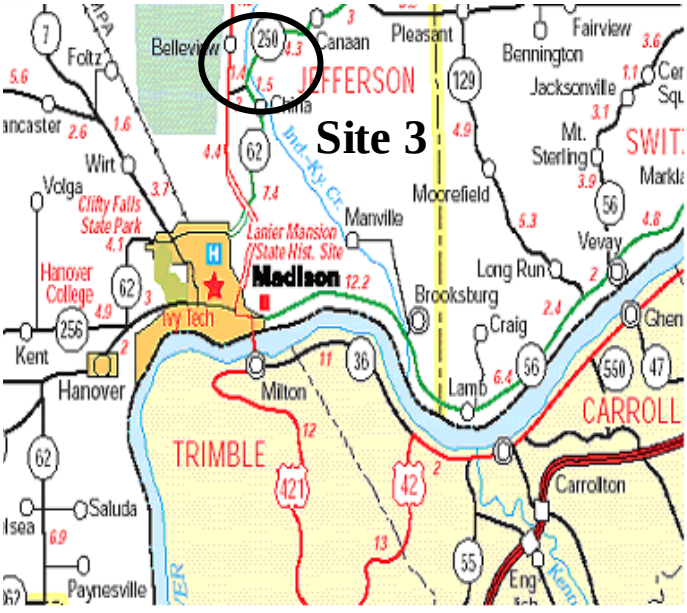

Figure 6: SITE 3 US-421 Madison

3.2 Visual Survey of Study Sites

3.2.1 Overall Distress Survey

For the three sites selected, visual survey included a detailed recording of distress data. The recorded distress information included fatigue cracking, alligator cracking, block cracking, edge cracking, wheel path longitudinal cracking, non wheel path longitudinal cracking, transverse cracking, rutting, and excessive bleeding for the flexible pavements. This data was then used to construct distress maps, which included the identified distress type and severity levels. Each data sheet contains two 15.25 m (50 ft) maps which represent 30.5 m (100 ft) of the test section. The detailed distress data survey sheets are provided in Appendix A.

The distress survey was conducted only for the driving lane. For each site, two sections of 15 m, being 500 m apart were surveyed. The detailed distress patterns were recorded for a distance of 20 m before and after the location from which the cracked cores were obtained. The *Distress Identification Manual* for the Long Term Pavement Performance Project was used as a standard guide for interpretation, identification, and rating of observed distresses.

Figure 7 to Figure 9 show the pictures of the three sites from where the cores were taken. Figure 7(a) shows severe longitudinal cracking on the wheel path as well as on the centerline of pavement of Site 1, I-65 North. Most of the wide cracks were sealed with bitumen and most of the centerline cracking was sealed with bitumen. Figure 7(b) shows a close up of the location on the wheel path from where the cracked samples No. 1 and No. 2 were obtained.

Figure 8(a) shows longitudinal surface cracking on left side of left wheel path on Site 2, I-65 loop near Indianapolis. The figure is marked with locations from where the cracked cores were obtained. Figure 8(b) shows a closer view of the hair line cracked pavement location.

Figure 7 (a) I-65 North

Figure 7 (b) I-65 North

Figure 7: Site 1 I-65 North of Lafayette

Figure 8(a) I-65 Near Indianapolis	
Figure 8(b) I-65 Near Indianapolis	

Figure 8: Site 2 I-65 near Indianapolis

Figure 9 (a) US 421 Madison

Figure 9 (b) US 421 Madison

Figure 9: Site 3 US 421 Madison

Figure 9(a) shows the surface cracked left wheel path line with low severity alligator cracking and Figure 9(b) shows the cracked pattern near the wheel path of Site 3, US-421 near Madison.

A summary of the distress survey is shown in Table 2. The distress types associated with asphalt concrete surface pavements, as per the distress identification manual, are shown in the left column. The units of measurement for each of the distress types are also identified in the left column. The extent of the measured distress for each particular level of severity is entered in the severity level columns identified as low, moderate, or high. The value "0" is entered for any distress types or severity levels not existing on the visual survey.

It was observed that Site 1, I-65 North, had the most distresses while the other two sites, Site 2, I-65 near Indianapolis, and Site 3, US-421 Madison, had very negligible distresses. The average longitudinal crack length for Sites 1, 2 and 3 were 126 m, 102.5 m, and 83 m, respectively.

3.2.2 Location of Longitudinal Surface Cracks

Inspection of distress survey maps and photos taken from the pavements indicate those surface cracks were not located the same way in each studied pavement. In Site 1 and 3 surface cracks were located in the wheel path while in Site 2 cracks were approximately 0.5 m outside the wheel path. However, for Sites 2 and 3 cracking seemed to be concentrated more on the left side of the pavement lane. Table 3 summarizes the findings.

Based on literature review, top-down cracks may initiate from the segregated areas in the pavement, which exhibit weaker material properties. Based on the visual survey, none of the sites seem to have exhibited load-end segregation as Figure 10, Figure 11 (a), and Figure 11 (b) show. Load-end segregation manifests itself as coarser and more open mat texture repeating about 25 to 30 meter intervals. However, this finding was not verified by laboratory testing.

Table 2: Report of distress data of study sites

DISTRESS SURVEY FOR PAVEMENTS WITH ASPHALT CONCRETE SURFACES							
Site		Site 1 I-65 North Of Lafayette			Site 1 I-65 North Of Lafayette		
Section ID		Section 1			Section 2		
Date of Distress Survey (mm/dd/yy)		9/26/2002			9/26/2002		
Surveyors		K.B.			K.B.		
Photos, video or both with survey (P, V, B)		P			P		
OBS. NO.	DISTRESS TYPE	SEVERITY LEVEL			SEVERITY LEVEL		
		LOW	MODERATE	HIGH	LOW	MODERATE	HIGH
1	Fatigue Cracking (Square Meters)	15.5	7.5	0	6	0	0
2	Block Cracking(Square Meters)	2.75	0	0	0	0	0
3	Edge Cracking (Meters)	5	0	0	0	0	0
4	Longitudinal Cracking (Meters)	41	0	0	85	0	0
	4a Wheel Path Length Sealed (Meters)	22	0	0	0	0	0
	4b Non-Wheel Path Length Sealed (Meters)	19	0	0	55	0	0
5	Transeverse Cracking (Meters)	10.5	6.2	0	5	11.25	0
	5a Number of cracks	4	2	0	2	4	0
	5b Length Sealed (Meters)	10.5	6.2	0	3.5	11.25	0
Site		Site 2 I-65 Loop near Indianapolis			Site 2 I-65 Loop near Indianapolis		
Section ID		Section 1			Section 2		
Date of Distress Survey (mm/dd/yy)		10/1/2002			10/1/2002		
Surveyors		K.B.			K.B.		
Photos, video or both with survey (P, V, B)		P			P		
OBS. NO.	DISTRESS TYPE	SEVERITY LEVEL			SEVERITY LEVEL		
		LOW	MODERATE	HIGH	LOW	MODERATE	HIGH
1	Fatigue Cracking (Square Meters)	5	0	0	22.5	0	0
2	Block Cracking(Square Meters)	0	0	0	0	0	0
3	Edge Cracking (Meters)	0	0	0	0	0	0
4	Longitudinal Cracking (Meters)	50	0	0	52.5	0	0
	4a Wheel Path Length Sealed (Meters)	0	0	0	0	0	0
	4b Non-Wheel Path Length Sealed (Meters)	0	0	0	0	0	0
5	Transeverse Cracking (Meters)	0	0	0	0	0	0
	5a Number of cracks	0	0	0	0	0	0
	5b Length Sealed (Meters)	0	0	0	0	0	0
Site		Site 3 SR 421 Madison			Site 3 SR 421 Madison		
Section ID		Section 1			Section 2		
Date of Distress Survey (mm/dd/yy)		9/26/2002			9/26/2002		
Surveyors		S.C.			S.C.		
Photos, video or both with survey (P, V, B)		P			P		
OBS. NO.	DISTRESS TYPE	SEVERITY LEVEL			SEVERITY LEVEL		
		LOW	MODERATE	HIGH	LOW	MODERATE	HIGH
1	Fatigue Cracking (Square Meters)	0	0	0	2.2	0	0
2	Block Cracking(Square Meters)	0	0	0	0	0	0
3	Edge Cracking (Meters)	0	0	0	0	0	0
4	Longitudinal Cracking (Meters)	29	0	0	54	0	0
	4a Wheel Path Length Sealed (Meters)	24	0	0	39	0	0
	4b Non-Wheel Path Length Sealed (Meters)	0	0	0	0	0	0
5	Transeverse Cracking (Meters)	0	0	0	0	0	0
	5a Number of cracks	0	0	0	0	0	0
	5b Length Sealed (Meters)	0	0	0	0	0	0

Table 3: Location of Surface Cracks.

LOCATION OF SURFACE CRACKING	SITE-1	SITE-2	SITE-3	POSSIBLE SEGREGATION
Lane width (m)	3.5	4.0	3.5	-
Left wheel path	Yes	No	Most	Yes – screed extensions
Right wheel path	Yes	No	Some	Yes – screed extensions
Outside of left wheel path	No	Most	No	Yes – screed extensions
Outside of right wheel path	No	Some	No	Yes – screed extensions
Centerline cracking	Yes	No	No	Yes – auger gear box

Longitudinal surface cracking in Site 3 was systematically located in the left wheel path area with some symmetrical cracking in the right wheel path; see Figure 11 (b). This may indicate some longitudinal mix segregation caused by screed extensions in the paver. The width of the paving lane is approximately 3.5 meters, which means that screed extensions were used to cover the entire paving width with one paver pass. The screed extensions can cause segregation of the mix depending on the specifics of the screed used and segregation tendency of the mix.

For Site 2 the outside wheel path cracking may also be initiated by segregation caused by screed extensions and edges of tunnel similarly as described for Site 3 above. In this case the weak area of the pavement is 0.5 meters outside of the wheel path which is consistent with the wider paving lane width of 4 meters; see Figure 11 (a).

For Site 1 the centerline cracking may be caused by segregation by the auger gear box in the center of the paver screed. The gear box may cause segregation as the mix is transported from the tunnel to the augers. The wheel path cracking may also be initiated from the areas of segregated mix, although in this case it seems to be less likely; see Figure 10.

General view of he Site 1	

Figure 10: Site 1, I-65 North of Lafayette.

Figure 11 (a): General view of he Site 2	
Figure 11 (b): General view of he Site 3	

Figure 11: Site 2, I-65 Loop and Site 3, US-421 Madison.

3.3 Distress Data Collection from INDOT PMS

The INDOT collects distress information for the interstates every year and for non-interstates every alternate year for the Pavement Management System (PMS). The distress data is obtained from the Path Runner data collection vehicle. The vehicle includes sensors, cameras, computers and other related equipment. It collects data at a speed of 70 mph and stores road condition data and images in real time in the on-board computer hard disk. The detailed distress data record obtained from the Path Runner data collection vehicle is provided in Appendix B. The distress information is gathered for a 500 foot section of road beginning each reference post. The results from the survey measurements displayed as an output are:

1. The IRI (International Roughness Index): It is the measure of the ride of the pavement. It measures the "bumpiness" of the pavement in terms of inches per mile.
2. Rut: It is the measure of the average depth of ruts in the wheel paths of the pavement. Rutting is most common on bituminous pavements and a severely rutted pavement would have average ruts of 6.3 mm (0.25 inch) or larger.
3. PCR (Pavement Condition Rating): It is the measure of the distresses on a pavement surface. These distresses include transverse cracking, longitudinal cracking, blocking cracking, etc. The pavement is reviewed at each reference post for 500 feet, the distresses are rated for severity and quantity, and a value is determined
4. Roadway horizontal and vertical curve information

An overall Pavement Condition Rating (PCR) index is calculated using the following equation:

$$PCR = 100 - \text{Total deduct points} \quad \textbf{(1)}$$

The deduct points are composed of weight value, severity and extent of the distress. The PCR is a composite index of all the varying types of distresses ranked on a scale of 100 to 0, with 100 being perfect and zero being impassable. A PCR of 50 is generally

considered unacceptable. The distress ratings are presented in Appendix B.

As a summary, the average values of IRI, PCR and Rut Depth over the respective mileposts were calculated for the three study sites, see Table 4. Site 1 had moderately good PCR rating, whereas Site 2 and Site 3 showed good pavement condition with low severity distresses. Site 2 had the lowest measured rut depth, 1.9 mm, although the other two sites also had very little rutting. Overall, the PMS survey results are in good agreement with the visual survey results discussed earlier.

Table 4: Pavement Condition Parameters

SITE ID	MILE POST	SURVEY YEAR	Average IRI (in/mile)	PCR (Scale 100-0)	Average RUT (mm) / (in)
Site 1 I-65	223-224	2001	74	93.33	4.2 / 0.167
Site 2 I-65	115.6-118	2001	115	99.80	1.9 / 0.076
Site 3 U-421	1.0-3.0	2001	54	99.00	4.1 / 0.163

3.4 Falling Weight Deflectometer (FWD) Testing

3.4.1 FWD Testing

Falling Weight Deflectometer (FWD) testing enables determination of the stiffness moduli of the pavement layers by measuring the pavement deflected shape (deflection basin) under applied load, as illustrated in Figure 12, whereas Figure 13 shows the FWD in use on Site 1 (I-65, north of Lafayette).

FWD deflection testing was conducted along three test lines for each site - lane center, left and right hand wheel paths. The lane center testing was conducted at 25 m spacing throughout the entire 500 m section. The testing in the wheel paths was concentrated at the crack locations where testing was at 10 m centers. The adopted spacing ensured a sufficient number of samples to back-calculate the pavement layer stiffness moduli. The testing used stress levels of approximately 450, 600, and 750 kPa. A

schematic example of the testing plan is shown in Figure 14.

The response of the pavement to impulse loading was measured with a set of nine velocity transducers (geophones) placed on different radial distances from the center of the loaded area, see Table 5. The data is normally reduced to three deflection parameters that relate to the different structural components of the pavement, e.g., foundation and bound layers. The assumption made is that the outer deflection sensors relate to the soil foundation while the shape of the deflection bowl close to the center of loading relates to the strength of the upper pavement layers. A summary of pavement response parameters is presented in Table 6.

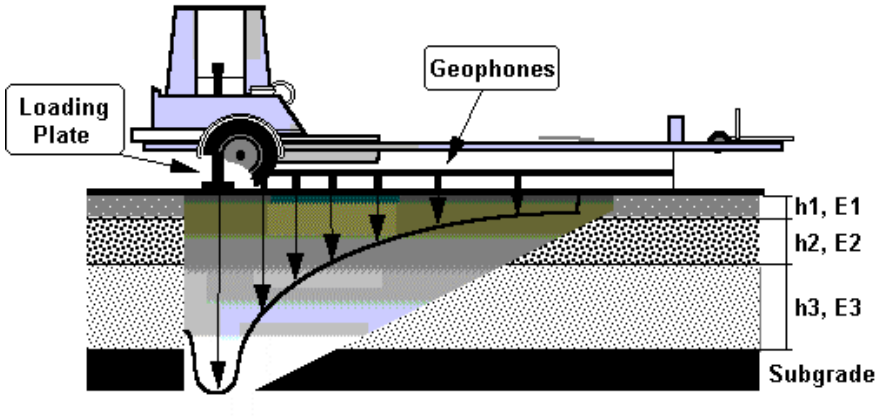

(Note: This schematic shows seven deflection readings. The work on this project made use of equipment with nine measurements)

Figure 12: Schematic of standard loading configuration and deflection basin

Figure 13: FWD testing on Site 1 (I-65 North of Lafayette).

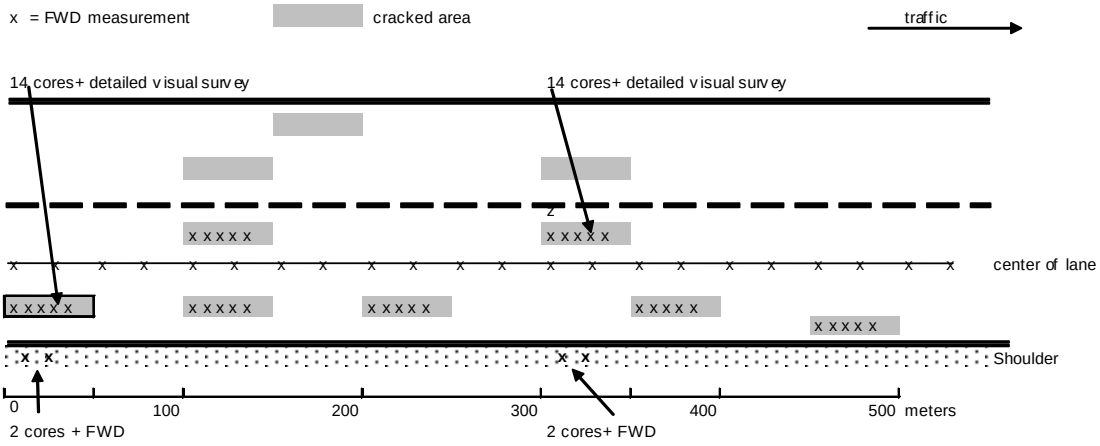

Note: Cores were not taken from the shoulder of site 1

Figure 14: Illustration of the locations for FWD measurements

Table 5: Geophone spacing

TRANSDUCER	RADIAL DISTANCE (mm)	RADIAL DISTANCE (in)
d1	0	0
d2	203	8
d3	305	12
d4	457	18
d5	610	24
d6	914	36
d7	1219	48
d8	1524	60
d9	1828	72

Table 6: Observations made from deflection

DEFLECTION PARAMETER	PAVEMENT RESPONSE
d1	Provides an indication of total pavement performance. The overall pavement structure appears to be reasonably uniform.
d1-d3	Provides an indication of the condition of upper pavement layers.
d7	Provides an indication of the soil stiffness.

Figure 15, Figure 16, and Figure 17 illustrate deflection profiles for Sites 1, 2 and 3, respectively. The figures show the deflection bowls are plotted as a function of twenty-one test stations.

From these plots of the deflection parameters we can summarize the pavement deflection response, as follows:

- Site 1 – The overall performance of this pavement (d1) indicates a reasonably high degree of variability. The variation in performance is associated with changes in deflection response of both the soil foundation and the rubblized base layers. The design thickness was 370 mm.

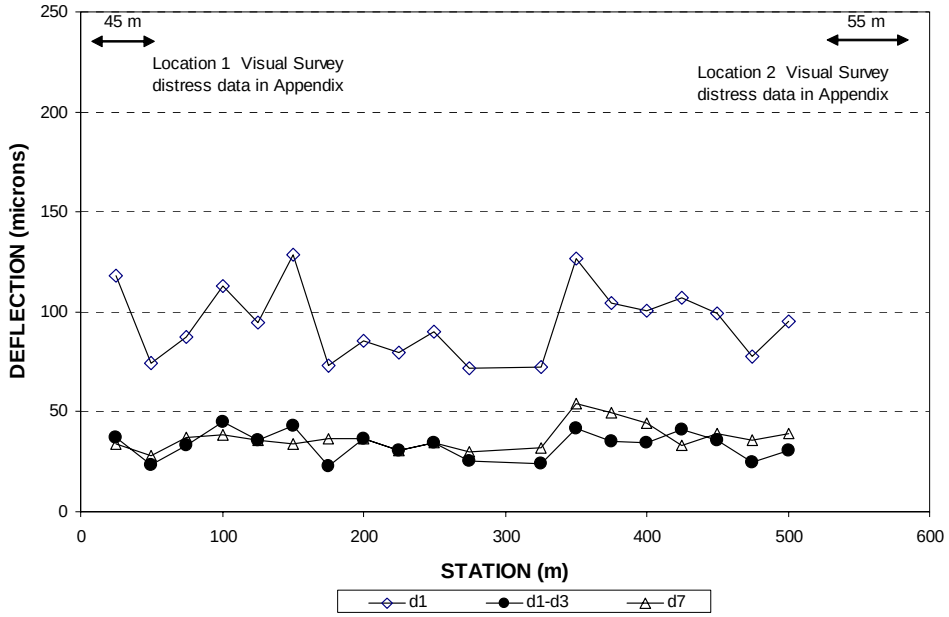

Figure 15: Inspection of Deflection Profile, Site 1 I-65 North

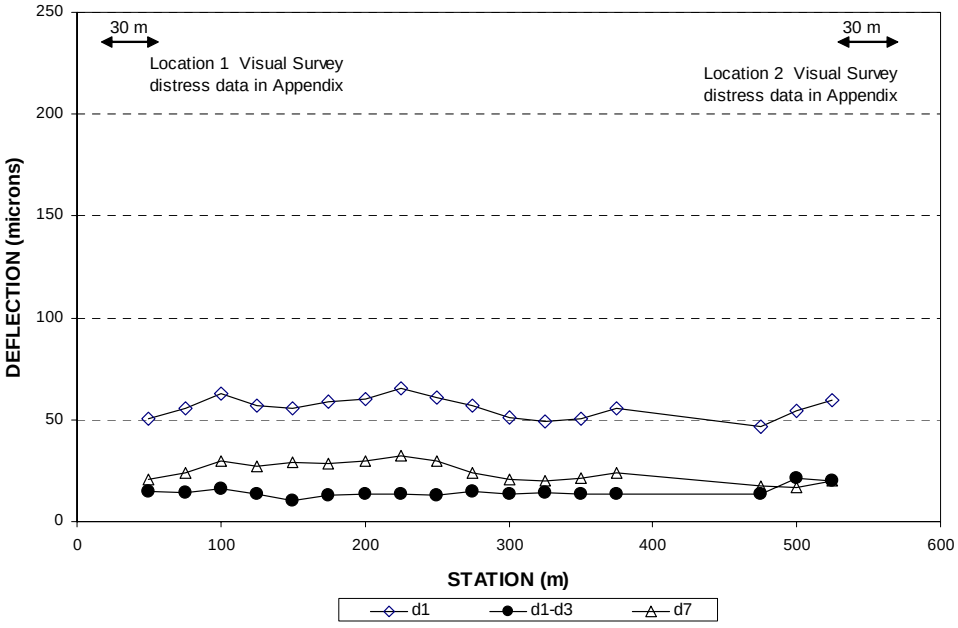

Figure 16: Inspection of Deflection Profile, Site 2 I-65 Loop

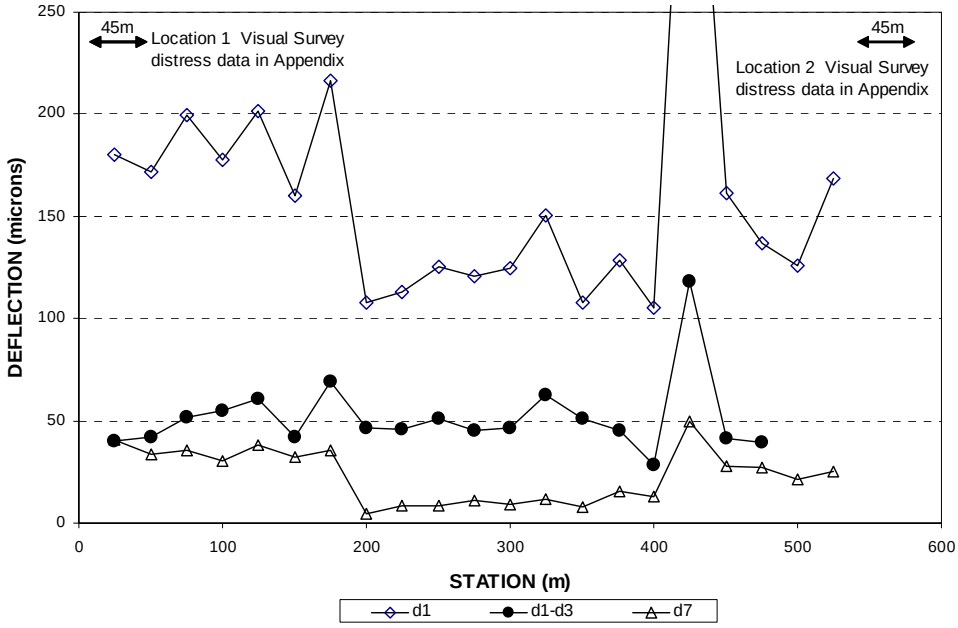

Figure 17: Inspection of Deflection Profile, Site 3 US 421 Madison

- Site 2 - This section has a relatively low and uniform deflection, due to the flexible base and thickness of construction used. The design thickness was 545 mm.
- Site 3 - At test point 400 there is a large peak in deflection. This could be caused by a crack or some other local defect. The deflection response indicates higher deflections for the two thirds end, whereas the middle third has lower and more uniform deflections. The deflection profile d7 indicates a change in construction at two test points in the rubblized base layer. The design thickness was 200 mm.

3.4.2 Back-calculation of Stiffness Moduli

The stiffness moduli of the pavement layers were determined from the FWD deflection data using back-calculation software DAPS™ (Deflection Analysis of Pavement Software). This software models the pavement as a quasi-static problem representing the stiffnesses of the various layers by linear elastic moduli (with a Poisson's ratio) in an

axisymetric layered elastic analysis.

In the determination of stiffness of the pavement layers the effect of the soil structure and method of modeling has been found to be of considerable importance (Rohde et al., 1992) on the fit of the deflection bowl. This aspect is considered in the software used by allowing selection of different soil models to represent the soil foundation. Selected deflection data was analyzed using the various methods allowed to assess which model best accounted for the deflection response. Based upon this analysis a model that computes a linear subgrade modulus with a specified depth resting over a rigid half space was adopted for the entire analysis; see Figure 18.

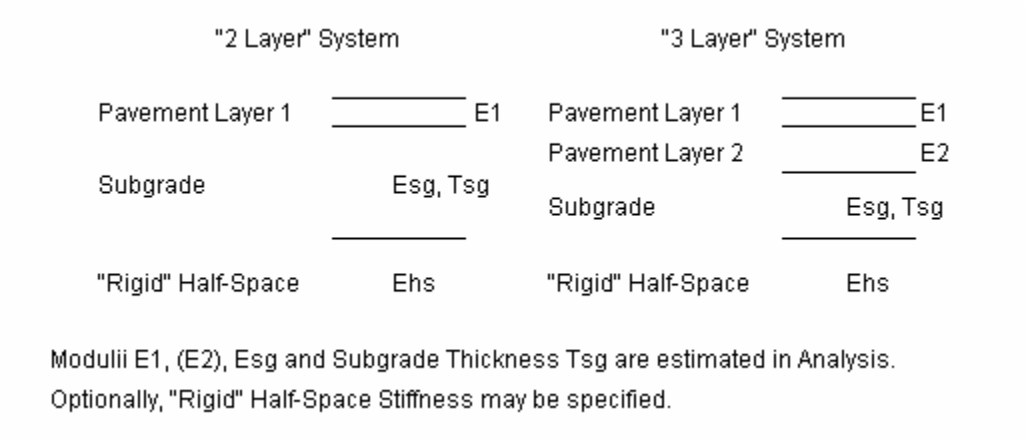

Figure 18: Definition of Rigid Half-Space and Subgrade Stiffness Model

The stiffness optimization uses a singular decomposition matrix analysis technique. In this process seven deflections for each bowl were used in the analysis. Checks for linearity in the pavement structural response indicated that the pavement could be treated as a linear system and that stress dependent effects on soil material properties did not significantly affect the analysis. Consequently, the best-fit solution from the back analysis was used from the analysis of the three tests at each test location, i.e., the bowl fit with the lowest rms (root-mean-square) error.

A least-square solution process was applied, employing seven of the nine measured

deflections as parameters characterizing the bowl. The rigid base (half-space) beneath the subgrade allows, to some extent, for known effects of non-linearity within the subgrade soil. Rohde et al., (1992) noted the importance of including a depth-to-bedrock calculation and the effect that this can have on surface deflections. The rigid base depth is used as an unknown to be solved for, along with the layer stiffness. After experimentation with different soil models and bedrock stiffness values, a constant value of 10,000 MPa stiffness was assigned to bedrock in the calculation procedures. A least-square solution to these simultaneous equations was obtained by an iterative process using an over-determined equation set and Singular Value Decomposition technique (Press et al., 1986).

In the equations, the partial derivatives are estimated numerically, by elastic layer analysis. The deflection analysis provides the measured deflection bowl and the resulting fitted back-calculated bowl. A typical result is illustrated in Figure 19.

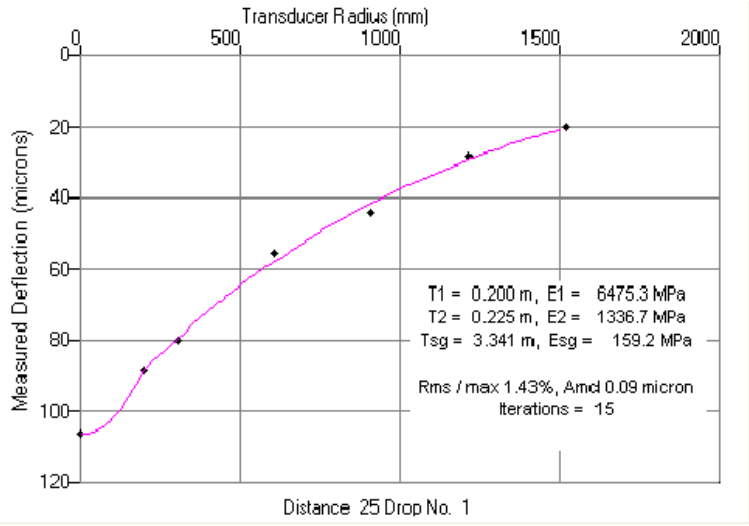

Figure 19: Example of fitted and measured FWD bowls, Site 3 US-421 Madison.

The results from this analysis are summarized in Table 7 for the median and 15-percentile properties. The median is quoted rather than the mean since gross errors that often result in misleading values are excluded. For pavement design and rehabilitation a value similar to the 15-percentile is often adopted since this gives a lower measure of the

pavement stiffness and allows for the variability in materials to be considered.

For Site 1, both wheel paths had stiffer mix than the center area, while for Site 2 and 3 the opposite was true. The modulus values shown in Table 7 are not temperature corrected so comparison between the sites cannot be made.

Table 7: Statistical Analysis of FWD data.

LOCATION OF TESTING AND STATISTIC		STIFFNESS (MPa)		
		ASPHALT	SUBBASE	SOIL
SITE 1: I-65 North of Lafayette				
Left Wheel Path	Median	11,602	1,175	306
	15 percentile	9,487	498	274
Center	Median	7,995	799	319
	15 percentile	5,356	291	234
Right Wheel Path	Median	9,696	479	295
	15 percentile	7,747	234	255
Avg. Median Modulus		9,764	818	307
Avg. 15% Modulus		7,530	341	254
SITE 2: I-65 Indianapolis				
Left Wheel Path	Median	8,421	407	437
	15 percentile	7,049	103	131
Center	Median	10,901	96	681
	15 percentile	9,633	41	303
Right Wheel Path	Median	9,518	177	589
	15 percentile	8,635	70	390
Avg. Median Modulus		9,613	227	569
Avg. 15% Modulus		8,439	71	275
SITE 3: US-421 Madison				
Left Wheel Path	Median	3,062	622	259
	15 percentile	2,681	488	158
Center	Median	4,917	1490	239
	15 percentile	4,086	675	130
Right Wheel Path	Median	3,268	642	276
	15 percentile	2,758	500	179
Avg. Median Modulus		3,749	918	258
Avg. 15% Modulus		3,175	554	155

3.4.3 Structural Capacity

The structural capacities were assessed using AASHTO 1993 Pavement Design guide methodology (Huang, 2002) by estimating the effective structural number SN_{eff} of the studied pavements. By knowing the effective structural capacity of the pavement the additional structural capacity can be estimated to upgrade the pavement condition to the desired serviceability, p_1.

The structural capacity was first assessed by estimating layer coefficients a_i for different pavement layer using the back-calculated modulus values. Table 8 shows the measured pavement surface and air temperatures during FWD testing. Pavement temperatures were calculated using Equation (3) at 1/3 depth of each total asphalt layer thickness.

Table 8: Air and pavement temperatures for FWD back-calculation.

SITE	TEST LINE	SURFACE TEMP. (^{0}C)	AIR TEMP. (^{0}C)	DEPTH (mm)	PAVEMENT TEMP. (°C)
1	Left	12.5	16.0	122.7	14.4
1	center	9.1	12.7	122.7	11.0
1	right	14.7	18.0	122.7	16.6
AVG.		12.1	15.6	122.7	14.0
2	left	2.3	6.0	176.7	4.3
2	center	2.9	5.8	176.7	4.4
2	right	3.2	6.3	176.7	4.9
AVG.		2.8	6.1	176.7	5.0
3	left	29.3	25.6	66.7	27.7
3	center	25.6	24.2	66.7	24.8
3	right	32.5	26.6	66.7	30.1
AVG.		29.1	25.5	66.7	28.0

Table 9 shows the back-calculated temperature corrected HMA modulus values and back-calculated base and subgrade values for the three sites. Modulus values were corrected to 20°C temperature. Temperature correction was done using the Witczak et al. (Andrei, Witczak & Mirza, 1999) stiffness predictive model by using relative stiffness

ratios between the measured and targeted pavement temperatures. Based on the magnitude of the asphalt mix modulus, a structural number $a_1 = 0.44$ was assigned to the asphalt layers. For Site 1 and 3, which had the rubblized Portland Cement Concrete base layer, the layer coefficient $a_2 = 0.22$ was assigned following INDOT's pavement design practice. For Site 2, the $a_2 = 0.15$ was assigned estimating the layer coefficient from the back-calculated modulus value using Equation (2). Using Equation (3) and assuming the drainage coefficient m = 1, the effective structural numbers SN_{eff} were computed. In Equation (3), D is the thickness of the layer. All back-calculated modulus values were average modulus values obtained from Table 7.

$$a_2 = 0.249(\log E_2) - 0.977 \quad (2)$$

$$SN_{eff} = a_1 D_1 + a_2 D_2 m \quad (3)$$

Table 9: SN_{eff} based on assigned layer coefficient values.

E_{AC} (MPa) @ 20°C	E_{Base} (MPa)	M_R (MPa)	HMA LAYER		BASE LAYER		SN_{eff}
			a_1	D_1 (in)	a_2	D_2 (in)	
6,752	818	307	0.44	14.5	0.22	16.0	9.9
3,923	227	569	0.44	20.9	0.15	18.0	11.9
6,263	918	258	0.44	8.0	0.22	15.0	6.8

According to AASHTO 1993 Design Guide, an alternative way of estimating the effective structural number is to use deflection far from the load to obtain the subgrade resilient modulus M_R. Deflection sensors d7 and d1 were used in the analysis, and all deflection values were temperature corrected using the AASHTO temperature correction tables.

Table 10 shows the back-calculated subgrade modulus values using this method. The SN_{eff} was computed using Equation (4) where D is the total pavement layer thickness, and E_p is the effective modulus of all pavement layers above the subgrade.

$$SN_{eff} = 0.0045 D \sqrt[3]{E_p} \quad (4)$$

Deflection sensors d7 and d1 were used in the analysis, and all deflection values were temperature corrected using the AASHTO temperature correction tables.

Table 10: SN_{eff} based on deflection sensors d7 and d1.

SUBGRADE M_R (MPa)	E_p (MPa)	D (in)	SN_{eff}
287	2,046	30.5	9.1
423	2,212	38.8	12.0
474	1,016	23.0	5.5

The highest pavement thickness in the AASHTO guide temperature correction tables is only 240 mm and only Site 3 complied with this. The other two sites, however, were much thicker. Therefore, the analysis was also done using the deflection temperature correction based on the relative pavement stiffness approach described above. The SN_{eff} was also computed using back-calculated M_R values with Equation (4) and estimating E_p using Equation (5) and then applying Equation (4). Table 11 summarizes results from all methods giving the average SN_{eff} values of 8.5, 10.2, and 6.1 for Sites 1, 2 and 3, respectively. It can be assumed that their average values are closest to the actual structural numbers of the sites.

$$E_p = \frac{E_n}{h^3} \left(\sum_{i=1}^{n} h^i \sqrt[3]{\frac{E_i}{E_n}} \right)^3 \quad (5)$$

where:

h = existing layer thickness

n = number of sublayers for which modulus values are computed

i = sublayer for which a modulus value is computed

Table 11: Average Effective Structural Number and traffic carrying capacity.

SITE	E_p (MPa)	SUBGRADE M_R (MPa)	SN_{eff}	W_{18} 10^8 ESALs
1	2,187	271	8.5	22.6
2	1,682	462	10.2	341
3	2,274	287	6.1	2.61

The 18-kip ESALs traffic W_{18} was computed using AASHTO 1993 flexible pavement design equation (Huang, 2002) with $S_0 = 0.35$, Reliability = 95%, and $\Delta PSI = 1.7$. The subgrade M_R values shown in Table 11 are corrected by C = 0.33 for the analysis.

After modulus temperature correction, Site 1 had the highest asphalt layer stiffness followed by Site 3 and 2, as Table 9 shows. The lower stiffness in Site 2 can be explained by the thick open graded asphalt layer that was used at the bottom of the layer. In the mix analysis it was assumed that the air void content of the open graded layer was 18%.

The cracked wheel paths did not have a lower modulus compared to the center of the pavement lane, as would be expected if the top-down cracking had weakened the pavement structure. All sites have excellent structural capacity despite the surface cracking. Based on the computed structural numbers and estimated traffic levels, Site 2 is a perpetual pavement based on the AASHTO 1993 Pavement Design Guide methodology.

4 LABORATORY TESTING

4.1 Coring

Several 150 mm (6 inch) diameter cores were obtained from the surface cracked pavements of each site to check the existence of top-down cracking and to measure mixture and binder properties. Three cores from the cracked area, nine to eleven cores from the un-cracked section around it, and two cores from the shoulder were obtained. Since there were two test locations per site, the total number of cores ranged from 29 to 32 depending on the study site.

The coring locations, mile posts, and exact distances between cores for the three sites are mapped in the distress data sheets presented in Appendix A. Figure 20 shows the coring location for Site 1 (I-65 North of Lafayette).

Figure 20: Coring locations in the pavement, Site 1.

Appendix C presents a detailed log in sheet for the obtained cores for the three sites. It also shows results of the core ID numbers, measured core thicknesses, inspection notes, and a detailed plan of testing responsibilities.

4.2 Laboratory Test Plan

Material testing followed a scheme that would enable mixture properties to be tied to the fundamental performance prediction properties, see Figure 21. Only the upper portion of the pavement section that exhibited surface cracking was included in the analysis for material properties.

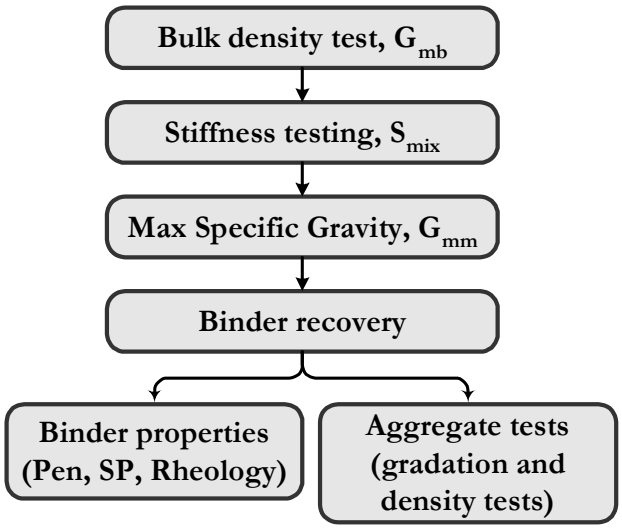

Figure 21: Laboratory testing plan for cores

The laboratory testing program was carried out with the help of North Central Superpave Center (NCSC). Test plan included binder and mixture consistency and mechanical tests to identify the mix properties that might affect the top-down cracking. The various mix parameters relating to different mixture properties are shown in Table 12. Table 12 also indicates the test method used for each parameter tested and test conditions.

Appendix C shows a detailed plan of testing with respect to the testing agency, the amount of material needed for binder testing, and results of the core thickness measurements and sample condition inspections.

Table 12: Measured parameters and test procedures

TEST METHOS	PARAMETER	TESTING ORDER	NUMBER OF CORES PER SITE TO BE TESTED	NOTES	TESTING AGENCY
AASHTO T166	Bulk Sp.Gravity, G_{mb}	1	all 22 intact cores per site	22 per site, 66 total	Purdue
AASHTO TP7	Shear Stiffness |G*|	2	2 cores per site, 4, 10, 20, 40 and 55 °C	2 |G*| per site, 6 total	NCSC
AASHTO TP9	Creep Compliance D(t)	2	6 cores per site, -20, -10, 0 °C (2 cores per temperature)	6 D(t) per site, 18 total	NCSC
AAHTO TP9	Indirect tensile strength	2	6 cores using same specimen as for D(t), 2 cores per temperature, -20, -10, 0 °C	6 Strength values per site, 18 total	NCSC
AASHTO T 209	Maximum specific gravity, G_{mm}	3	-combine 2 to 3 cores to get one 1.5 kg G_{mm} sample -make 2 samples per site	2 G_{mm} per site, 6 total	Purdue
AASHTO TP2	Extraction to get binder content, P_b	4	-use G_{mm} samples to get respective binder content	2 P_b per site, 6 total	NCSC
AASHTO TP2	Binder recovery	4	-all 28 cores per site if needed -recover G_{mm} samples separately to obtain P_b	one "set" of binder samples (rheological) per site using all cores	NCSC
AASHTO T11& T27	Gradation	5	Use recovered aggregate from both G_{mm} samples	2 gradations per site, 6 total	Purdue
AASHTO T49	Penetration at 2 temp	6	one test per site (note each test normally includes three needles in tin)	2 Pen per site, 6 total	NCSC
AASHTO T53	Softening Point	6	2 replicates per site	2 $T_{R\&B}$ per site, 6 total	NCSC
AASHTO TP5	DSR frequency sweep at 5 temperatures	6	2 replicates per site tests at 76, 35, 64, 52, 40, 25 and 15 °C in range 0.1 rad/sec to 10 rad/sec. Use IP standard to get strain levels.	2 test per site, 6 total	NCSC
AASHTO TP3	DTT at 2 temperatures	6	1 replicates per site (needs 6 specimens per test), -6, -12 and –18 °C	6 test per site, 18 total	NCSC

4.3 Measured Layer Thicknesses

The pavement structure in each study site consisted of full depth asphalt. Sites I-65 North and US-421 had rubblized concrete base, and I-65 near Indianapolis had compacted subgrade base. The structural design thicknesses for the full depth asphalts were 370 mm, 530 mm, and 200 mm, respectively. The obtained cores were inspected and different pavement layers in the cores were measured using a caliper.

The measured pavement layer thicknesses are summarized in Table 13. It was observed that the average measured thickness of full depth asphalt converged in the case of Site 3, US-421 Madison, where the design thickness was 200 mm. For Site 2, the difference between the measured HMA thickness of 474 mm and design thickness of 530 mm was 75 mm. By inspection it was obvious that the cores were not obtained through the full thickness of the pavement, because the last layer was the large aggregate drainage layer designated as Bituminous Base 2 HV, instead of the finer base layer of Bituminous Base 5 D (see Table 1). For Site 1, the difference between measured HMA thickness of 311 mm and design thickness of 370 mm is 59 mm. Again, it can be assumed that the obtained core did not include a full thickness of the designed base layer.

Table 13: Measured layer thicknesses.

SITE 1: I-65 North			**SITE 2: I-65 Loop**			**SITE 3: US-421 Madison**		
LAYER	**THICKNESS**		**LAYER**	**THICKNESS**		**LAYER**	**THICKNESS**	
	(mm)	**(in)**		**(mm)**	**(in)**		**(mm)**	**(in)**
Surface 9.5	30.6	1.2	Surface 9.5	30.6	1.2	Surface 12.5	33.2	1.3
Interm 12.5	114.8	4.5	Interm 12.5	66.3	2.6	Interm 19.0	76.5	3.0
Interm 19.0	89.3	3.5	Interm 19.0	122.4	4.8	Base 25.0	89.3	3.5
Base 25.0	76.5	3.0	Base 63.6*	255.0	10.0	-	-	-
Total	311.1	12.3	Total	474.3	18.7	Total	198.9	7.8

* Maximum aggregate size

Also the maximum nominal aggregate size of each mix was estimated measuring the nominal maximum aggregate size (NMAS) of the mixtures. The estimated nominal maximum aggregate is given next to the layer type information in Table 13. Estimation was done by randomly measuring the size of aggregates from the cores.

4.4 Inspection of Cracks from Cores

4.4.1 Visual Inspection

The three cores obtained from the cracked locations of pavement were examined to investigate the length of the top-down cracks and their orientation in the pavement. The visual inspection indicated that cracks did not seem to penetrate deeper than the thin surface layer.

Figure 22 shows pictures of three cracked cores, one core from each test site. For Site 1, the core ID is S2, for Site 2 the core ID is S20, and for Site 3 the core ID is S21. It is evident that the surface cracks did not penetrate visibly through the cores. The figure also shows the various pavement layers and aggregate size of the mix. Note that the core shown for Site 2 and 3 does not present the full depth of the pavement because the bottom part of the core was not retrieved during coring.

A detailed crack inspection was done for all cracked cores. Figures 23, 24, and 25 show obtained core, core location, and measured crack length for the three sites. Figure 23 shows Site 1 with visible cracking in the surface of the core. The thickness of the crack was 20 mm and crack orientation was downward skewed. The visible surface crack did not seem to penetrate further to the pavement than to the surface course.

Site 1: Core height 300 mm Site 2: Core height 430 mm Site 3: Core height 200 mm

Figure 22: Surface cracked cores obtained from the studied pavement sites.

Figure 24 shows typical cracking of Site 2, where the cracks were more like narrow hairline cracks with a low visibility. Again, the crack does not seem to penetrate further to the pavement than to the surface layer. The length of the crack was 22 mm and it was oriented vertically downward. The core shown in this figure is not a full length core because the large size aggregate layer created a weaker joint and layers were separating during handling of the cores.

Figure 25 shows a typical cracking of Site 3, where the cracks were more visible being in the centerline of the pavement. The core shown in this figure was taken from the left wheel path from a thin hairline cracked section. The crack length was 15 mm being half of the surface layer thickness, and the crack was oriented vertically downward.

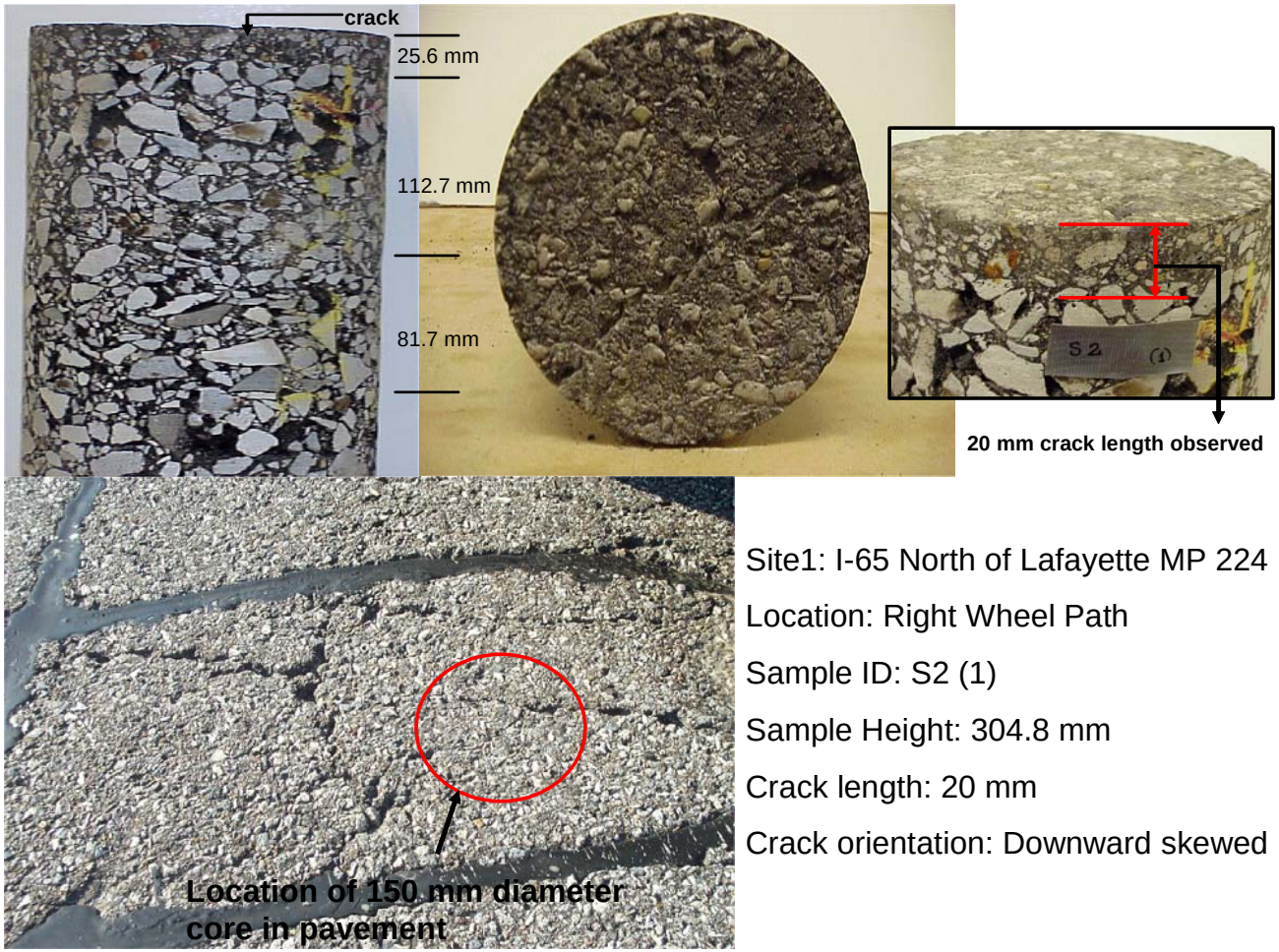

Site1: I-65 North of Lafayette MP 224

Location: Right Wheel Path

Sample ID: S2 (1)

Sample Height: 304.8 mm

Crack length: 20 mm

Crack orientation: Downward skewed

Figure 23: Inspection of Cracks, Site 1, I-65 North.

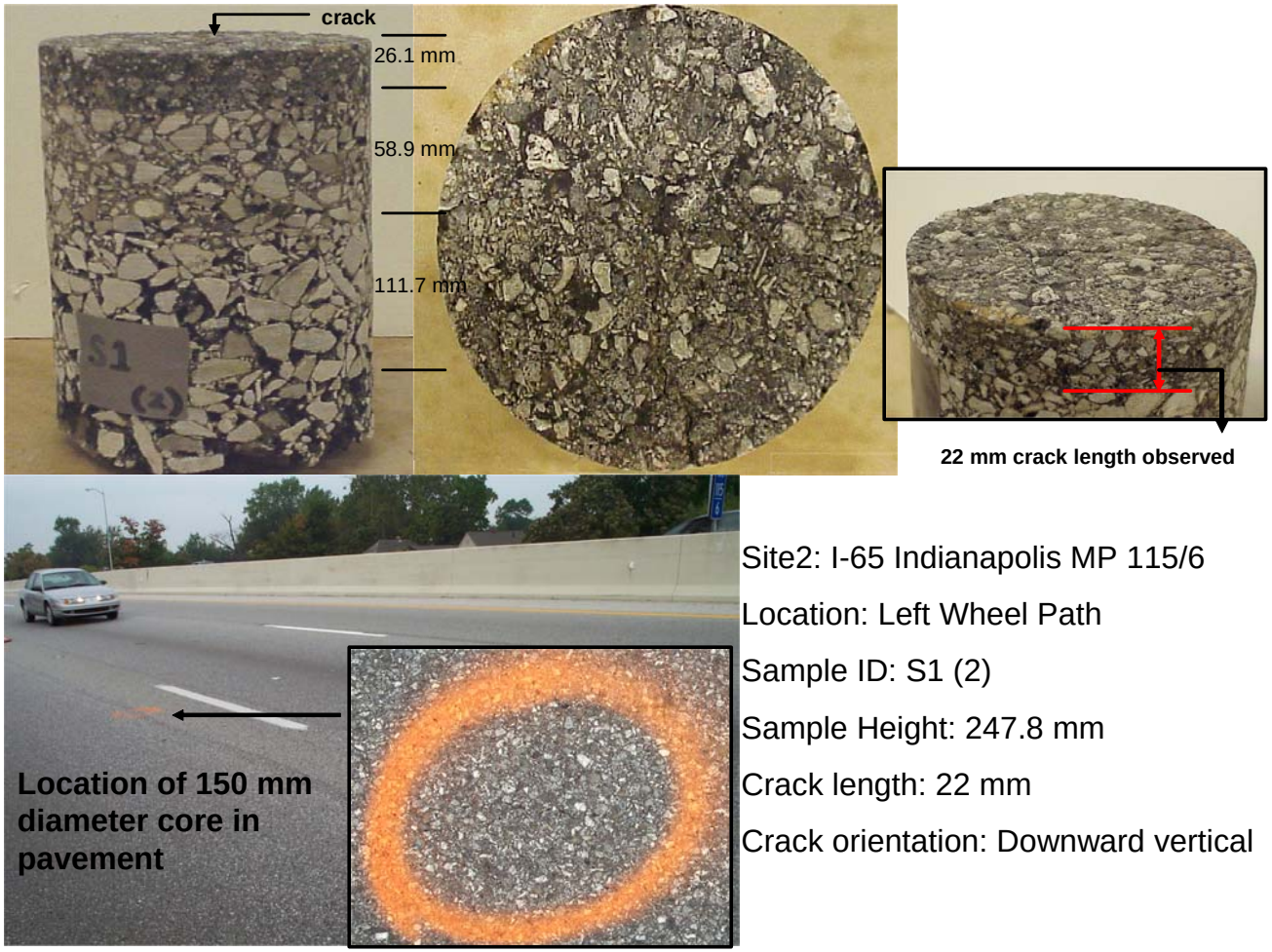

Figure 24: Inspection of Cracks, Site 2, I-65 Loop.

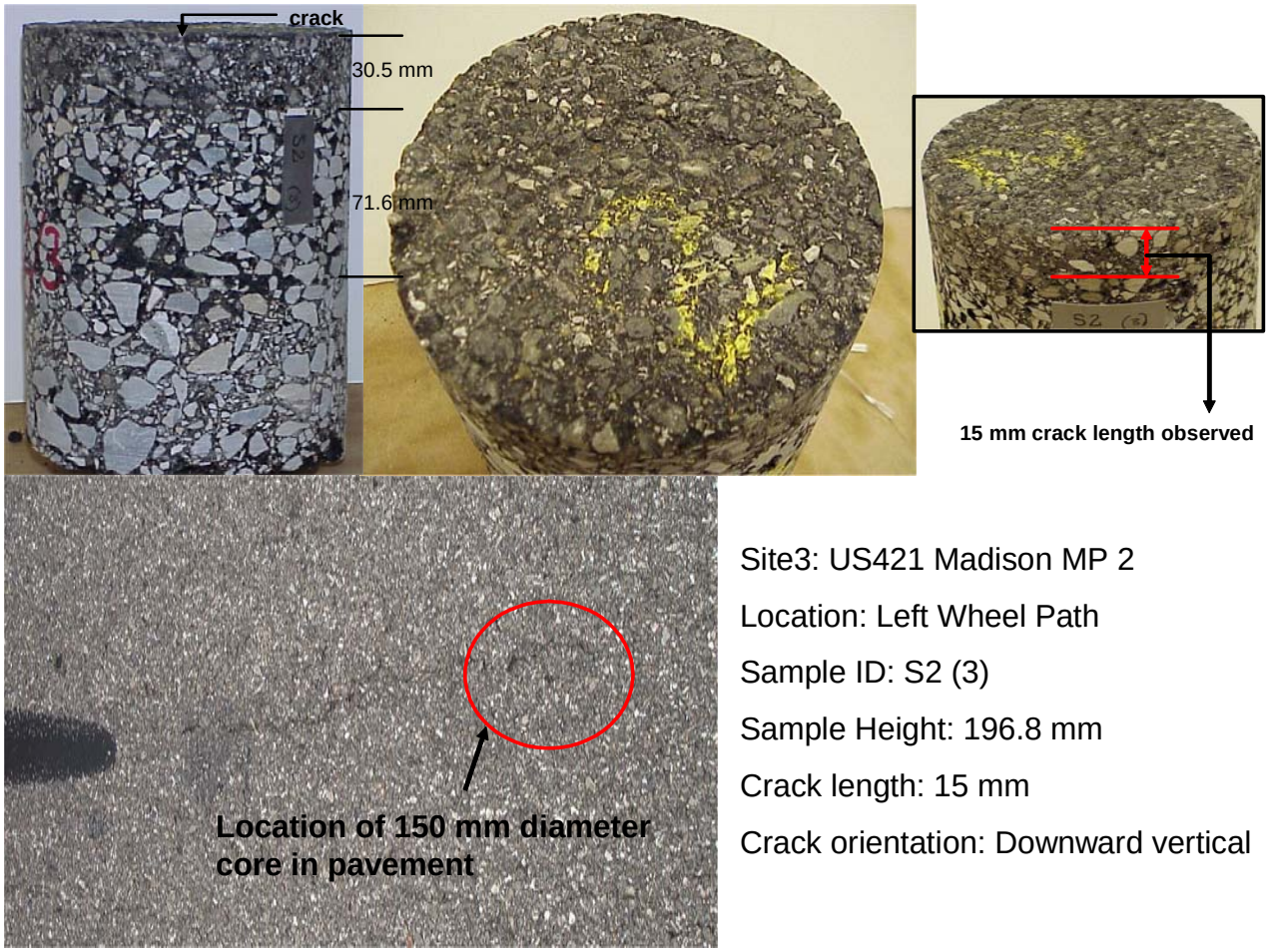

Figure 25: Inspection of Cracks, Site 3, US-421 Madison.

4.4.2 Imaging Analysis

Based on the visual observations, the length of the crack was approximately 20 mm from the surface. A three dimensional (3-D) imaging analysis using X-ray Tomography (CAT scanning) was performed on cracked cores to investigate the path and mechanism of crack propagation in the pavement, and to compare the results of the crack length from the imaging analysis with the visual observations. The imaging analysis was conducted at the Turner Fairbank Highway Research Center (TFHRC) with the Simulation, Imaging and Mechanics of Asphalt Pavement (SIMAP) program, see Figure 26.

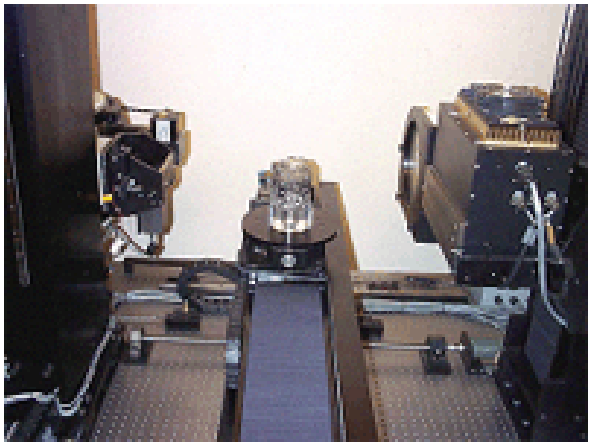

Figure 26: X-Ray Scanning at TFHRC

The X–ray tomography imaging is a non-destructive technique to investigate the internal structure of materials. It measures the path of X-rays through the material. It differs from the traditional X-ray technique with respect to energy. The technique for producing a tomography image includes data acquisition, reconstruction of structure and picture processing. For data acquisition, the structure is rotated while being exposed to high-energy X-ray beams. The radiation that is not absorbed by the material is detected and digitally saved as raw data. For reconstruction of image, the data is analyzed mathematically to produce a cross sectional picture of the scanned image. The picture is then processed with

different scales of colors for representing different phases, internal cracks, geometrical characteristics and deformations. The X-ray tomography has been applied various ways to study the asphalt concrete such as 3-D imaging of specimen, predicting mechanical response of mixture by applying mechanics to 3-D images, analyzing segregation of aggregate structure, and distribution of air void contents.

For each study site, one 150 mm diameter core obtained from the cracked area of the pavement was analyzed by X-ray Tomography Analysis (CAT scanning). From Site 1, core ID S16 (1), Site 2 core ID S1 (2), and Site 3 core ID S2 (3) were analyzed. Note that the scanned cores for Site 2 and 3 are the same cores shown in Figures 23 and 24.

A cross-sectional picture of the cores was reconstructed from the scanned image. The 3-D picture was then sliced into 184 slices for Site1 and Site3, and 186 slices for Site 2, to investigate crack propagation inside the core. Figure 27 shows the same scanned slice in three different color combinations, green, red and black & white. The ID of the core shown in Figure 27 is S16 (1) and it is from Site1 I-65 north of Lafayette. No visible cracks can be detected inside the core.

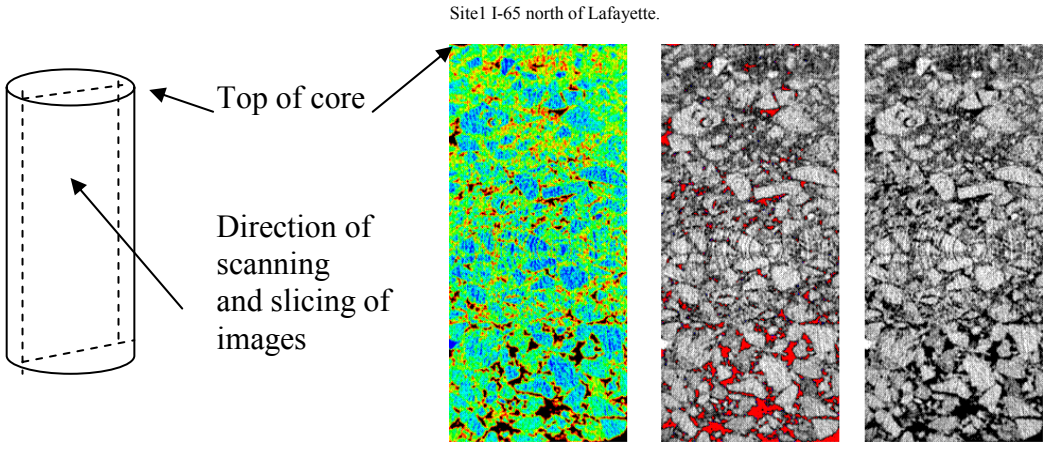

Figure 27. Scanning of Cores.

Figure 28 shows another example of the inspected core. The ID of the core is S2 (3) from Site 3. Inspection tried to identify direction of crack propagation, average height of cracks, and cracking pattern from the X-ray tomography sliced images. Inspection of images indicates that the visible crack seen in the top of the core does not penetrate deeper to the core than the surface layer, agreeing with the visual observations.

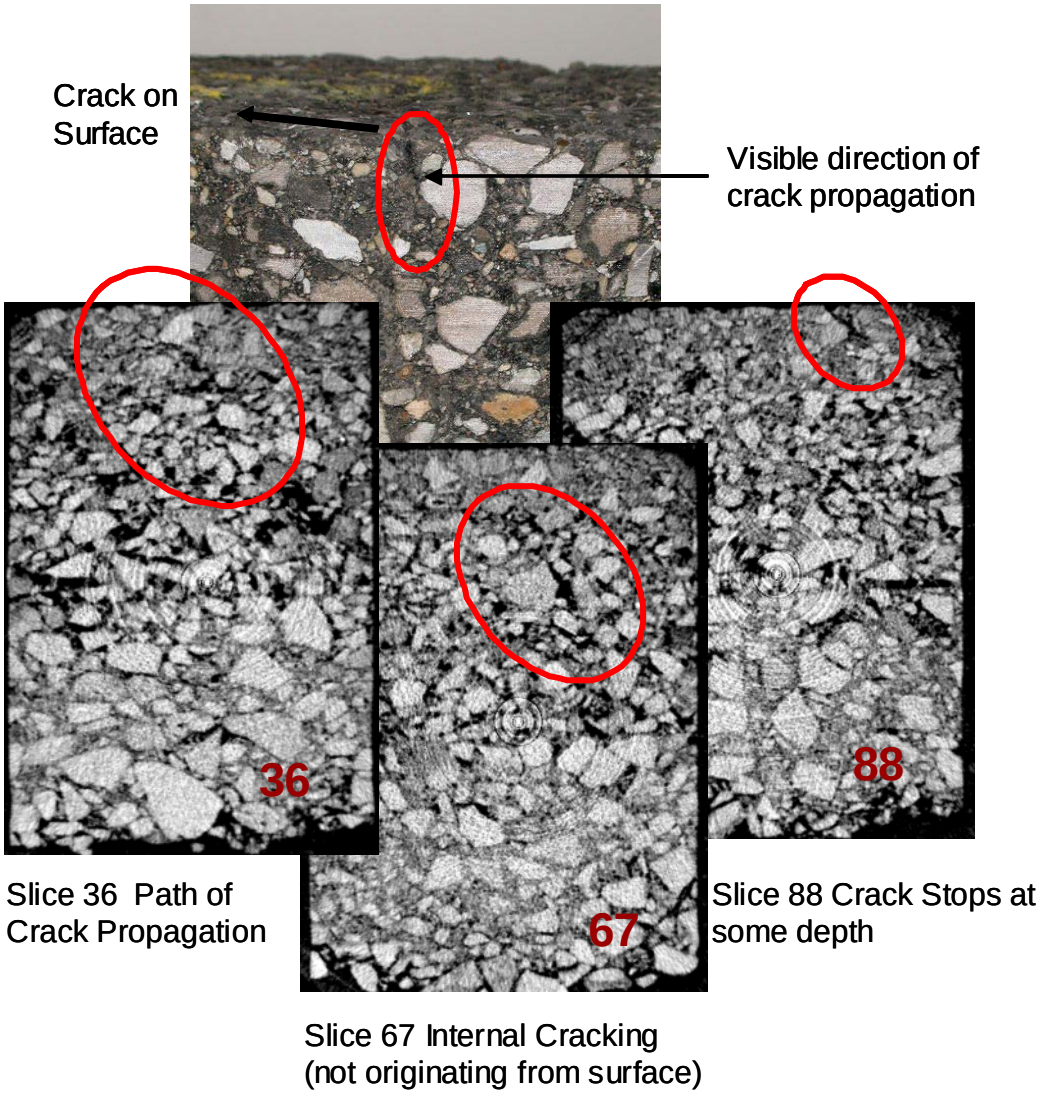

Figure 28: Site 3 US421 Madison ID S2 (3)

4.5 Test Results for Conventional Asphalt Binder Properties

The penetration test is an empirical test used to measure the consistency of asphalt binder. The penetration test was performed at 25°C and 45°C test temperature in accordance with the AASHTO T49 test procedure. The test results are presented in Table 14.

Table 14: Penetration Test Results

REPLICATE	TEMPERATURE 25°C			TEMPERATURE 45°C		
	PENETRATION (0.1 mm)			PENETRATION (0.1 mm)		
	SITE 1	SITE 2	SITE 3	SITE 1	SITE 2	SITE 3
1	11	18	10	67	90	70
2	10	19	11	64	90	70
3	11	20	11	65	89	68
Average	10.7	19.0	10.7	65.0	90.0	69.0
Std Dev	0.58	1.00	0.58	1.53	0.58	1.15
CV%	5	5	5	2	1	2

The requirements for the penetration graded asphalt cements (ASTM D946) are presented in Table 15. The measured binder penetrations are less than the lowest penetration grade of neat binders, indicating significant binder hardening. The original binder grade for Site 3 was PG 70-22 which refers approximately to Pen 40-50 binder. The original binder type information for the other sites was not available. Site 2 had the softest binder penetration being 19 while the other two sites had 10.7 (25°C).

Table 15: ASTM requirements for penetration graded asphalt cements

Penetration at 25°C	PENETRATION GRADE									
	40-50		60-70		85-100		120-150		200-300	
	Min	Max	Min	Max	Min	Max	Min	Max	Min	Max
	40	50	60	70	85	100	120	150	200	300

The ring and ball softening point testing was conducted according to AASHTO T53; see Table 16. Site 2 had the lowest softening point of 62.8°C which is in agreement with the penetration test results. However, the difference was not large compared to the other sites.

Table 16. Ring and Ball Softening Point

REPLICATE	$T_{Ring\&Ball}$ (°C)		
	SITE 1	SITE 2	SITE 3
1	65.0	62.5	65.5
2	65.0	63.0	65.5
Average	65.0	62.8	65.5

4.6 Test Results for Asphalt Mixture Composition

The bulk specific gravity (G_{mb}) values were measured for the surface layer (~25 mm thick HMA layer) for each sample obtained from all three study sites in accordance with AASHTO T166 test procedure. The core samples were collected from the pavement over the left, center, and the right wheel paths and the G_{mb} values have been calculated and tabulated correspondingly. Detailed test data is shown in Appendix D.

The theoretical maximum specific gravity (G_{mm}) values were measured in accordance with AASHTO T209 test procedure. For obtaining the G_{mm}, two to three cores were combined to get a 1.5 kg sample. The test required two samples per site, so a total of six cores were required per site. The G_{mm} test results are presented in Appendix D. As a summary, the G_{mm} for Site 1 was 2.486, for Site 2 it was 2.502, and for Site 3 it was 2.458. The design G_{mm} value for Site3 was 2.433 based on the JMF provided by INDOT, which was somewhat lower than the measured G_{mm} value of 2.458, but this is still within the acceptable difference of two laboratories. The JMFs data was not available for the other sites.

The percentages of air voids in the total mix were determined from the relation between G_{mm} and G_{mb} values. A summary of the calculated air void content values are

presented in Table 17. The detailed air void calculations are presented in Appendix D. The density in the left wheel path or the right wheel path is higher than the center of the pavement for Site1, I-65 North, due to the traffic loading and mix densification in the wheel paths. This phenomenon is not as clear for the other two sites. The age of Site 1 was 11 years compared to the 12 and 4.5 years for Sites 2 and 3, respectively. Site 3 had only half of the rutting compared to Site 1 so traffic has not yet had enough time to densify the pavement. Site 2 had also only half of the rutting compared to Site 1, which indicates more densification/shear resistant mix compared to Site 1. The average air void content for Site 1 and Site 2 are within typical in-situ density requirements of 92.5% of G_{mm}, but Site 3, Location 2 has significantly higher air void content.

The FWD results agree with these findings indicating that some densification in the wheel path has occurred in Site 1 because of the increased stiffness of the mix. The other two sites did not show mix densification based on FWD stiffness measurements.

Table 17: Summary of percent air void content.

POSITION IN THE PAVEMENT	**SITE 1 I-65 NORTH**		**SITE 2 I-65 INDIANAPOLIS**		**SITE 3 US-421 MADISON**	
	Location 1	**Location 2**	**Location 1**	**Location 2**	**Location 1**	**Location 2**
LWP	6.1	6.7	8.5	8.2	9.3	11.6
CENTER	8.6	7.6	6.4	8.4	8.9	11.3
RWP	6.8	6.8	6.1	8.5	8.8	9.5
SHOULDER	-	-	8.0	9.1	7.5	8.8
Average	7.2	7.0	9.0	8.5	8.6	10.3
Std Dev	1.31	0.51	1.31	0.14	0.26	1.13
CV%	18.1	7.2	14.5	1.6	3.0	10.9
LWP= Left Wheel Path						
RWP= Right Wheel Path						

The gradation data for the mixtures were determined according to the AASHTO T11 and T27 procedures. The chart of aggregate gradation with the restricted zone and control points corresponding to Nominal Maximum Aggregate Size (NMAS) 9.5 mm is presented

in Appendix D. The average gradation curve for all three study sites passes through the restricted zone and fell well within the minimum and maximum control points for the NMAS 9.5 mm. For all three sites, the surface mix gradation was on the coarse side of the gradation curve.

The extraction of binder content was performed in accordance with the AASHTO TP2 test procedures. The average binder contents were 5.4, 5.9, and 6.3% for Sites 1, 2, and 3, respectively. For Site 3, the average extracted binder content of 6.3% and the JMF design binder content of 6.2% compared well. For other sites, the JMF data was not available, however, Site 1 had almost one percent lower binder content than Site 3.

4.6.1 In-situ Volumetric Properties

Table 18 summarizes the in-situ volumetric properties for the three surface mixtures. Compared to the WesTrack crack resistant mixtures discussed in Chapter 2, Site 3 had enough binder in the mix compared to the other sites that had less than 9% which is needed for a good cracking resistance. Also, Site 1 and 3 mixtures had VFA less than 53% and VMA > 14% which indicates poor cracking resistance in the mixture.

The in-situ volumetric properties deviate from the mix design values, as expected. Based on JMF for Site 3, the design V_a = 4%, VMA = 15.2%, VFA = 73.7%, and V_{beff} = 11.2%.

Table 18: In-situ volumetric properties.

MIX VOLUMETRIC PROPERTY	SITE 1	SITE 2	SITE 3
VMA, %	16.9	16.7	19.8
VFA, %	51.8	55.8	49.0
V_{beff} %	8.8	8.6	9.7
V_a %	8.2	7.4	10.1

5 ANALYSIS OF RHEOLOGICAL AND MECHANICAL TEST DATA

5.1 Master Curve Construction

The material characterization of sampled pavements included the following two tasks: 1) Binder master curve construction from the measured binder test data; and 2) Mix master curve construction from the measured mix test data. The master curve allows a full material characterization of a visco-elastic property as a function of loading time and temperature. Both the binder and mixture master curves were constructed by combining the measured test data in a certain way to create a full temperature range master curve.

The binder tests included the Dynamic Shear Rheometer Test (DSR) at high and intermediate test temperatures and the Direct Tensile Test (DTT) at cold temperatures. The mix testing included the intermediate and high temperature SST-Shear Frequency Sweep shear modulus testing and low temperature Creep Compliance testing which together should give the data for the full temperature range for mix master curve.

The rheological data were analyzed in the RHEA^{TM} software (Rowe, 2000) to determine the relaxation spectra of the tested binders and mixtures. Using calculated relaxation spectra (Baumgaertel and Winter, 1989) and a simple Poisson's ratio conversion between shear and extensional modulus, the measured data sets were transposed into a desired master curve at desired reference temperature.

The scheme for constructing the master curve is by empirical shifts of data obtained at different temperatures along a logarithmic time or frequency axis by a shift factor (a_T). Since time-temperature superposition holds, the various relaxation times, in the case of a given relaxation process, have the same temperature dependence. Thus, the relaxation behavior at one temperature can be superimposed on another temperature by shifting an amount (a_T) along the logarithmic time axis. Once the shift factors have been determined, the reduced frequencies (ξ) can be calculated for the temperature isotherms that have to be shifted to the reference temperature to develop the master curve. The reduced frequency is given by:

$$\xi = \omega \cdot a_T \tag{6}$$

where ω is angular velocity obtained from $\omega = 2\pi f$ where f is the loading frequency. The reduced frequency can be represented in the logarithmic form as:

$$\log(\xi) = \log(\omega) + \log(a_T) \tag{7}$$

The RHEA™ software generates the estimated values of constants C_1 and C_2 for the Williams, Landel and Ferry (WLF) relation (Williams, Lendel & Ferry, 1955) which is given by:

$$\log(a_T) = \frac{-C_1 \cdot (T - T_R)}{C_2 + (T - T_R)} \tag{8}$$

5.2 Asphalt Binder Testing and Analysis

5.2.1 Dynamic Shear Rheometer Test

The dynamic shear rheometer (DSR) is used to characterize the viscous and elastic behavior of asphalt binders at high and intermediate service temperatures. The shear frequency sweep tests were performed at seven temperatures of 76°C, 64°C, 52°C, 40°C, 35°C, 25°C and 15°C according to the AASHTO TP5 with loading rate of 0.1 to 10 Hz. Test results for the measured binder complex shear modulus |G*| and phase angle δ are given in Appendix E

5.2.2 Direct Tensile Test

The Direct Tensile Test (DTT) was performed in accordance to the AASHTO TP3 test procedure to determine the low temperature tensile stresses and strains of asphalt binder. The tests were performed at temperatures of -18°C, -12°C for Site 1, -18°C, -12°C, and -6°C for Site 2, -12°C and -6°C for Site 3, which are within the standard range of 0°C to -36° C, where the asphalt exhibits brittle behavior. The specimens were loaded in

tension at a constant strain rate of 1 mm/min until break. Test results are shown in Appendix F.

Strength, Strain and Energy to Failure

The raw test data was analyzed using the eVDTT software developed by Abatech. This software uses the "RAW" data file produced by the control software of the DTT test device to conduct the analysis in accordance with the current TP3 analysis procedure (AASHTO, 2000). The data is also corrected for start-up errors using the procedure defined by Rowe, D'Angelo, Ho and Sharrock (2002). For each data set a plot of the stress versus strain was inspected to ensure that the data was of consistent quality, see Appendix F. Following inspection of the test results the mean data was then reported for each material evaluated as per the example given in Table 19.

Table 19. Typical test report generated by eVDTT software

DIRECT TENSION TEST FRACTURE OR FLOW PROPERTIES

Sample ID Site 3
Test Date 18-02-03
Temperature -12.0°C
Extension Rate 1.01 mm/min

Specimen	Max Time sec	Time @Break sec	Max Stress MPa	Stress @Break MPa	Max Strain %	Strain @Break %	Energy @Break mJ	Load @Break N	Strain % @Max Stress	Energy mJ @Max Stress	Energy mJ @Max Time	Type of Failure
1*	9.944	9.762	1.895	1.895	0.5163	0.4900	5.238	68.23	-	-	-	Br
2	13.93	13.84	2.432	2.432	0.7214	0.6940	9.594	87.55	-	-	-	Br
3	15.19	15.02	2.581	2.581	0.7877	0.7537	11.15	92.92	-	-	-	Br
4*	8.324	8.206	1.644	1.644	0.4315	0.4103	3.762	59.17	-	-	-	Br
5	12.47	12.40	2.249	2.249	0.6462	0.6204	7.955	80.95	-	-	-	Br
6	10.58	10.55	2.049	2.049	0.5497	0.5300	6.273	73.77	-	-	-	Br
7	12.37	12.31	2.266	2.266	0.6405	0.6158	7.998	81.59	-	-	-	Br
Mean	12.91	12.82	2.315	2.315	0.6691	0.6428	8.594	83.36	-	-	-	
Std Devn	1.745	1.693	0.2012	0.2012	0.09000	0.08498	1.849	7.243	-	-	-	

Notes.
* = Test discarded on basis of failure strain.
Strain channel is Tensile extension mm
Stress channel is Tensile stress MPa
Br = Brittle failure
Br/Du = Brittle/Ductile failure
Du = Ductile failure

Table 20 shows a summary of the DTT test results. The strains at failure are quite low

indicating brittle behavior. The lowest two values obtained from the test were excluded from the means. Site 2 had the lowest strain 0.4299% at -12°C indicating the most brittle behavior, although the conventional binder testing indicated that this binder was the softest of the measured binders.

Table 20. Measured failure stress and strain from DTT test.

SITE	Temperature (°C)	Max Stress at Break (MPa)	Strain at Break (%)	Energy at Break (mJ)
Site 1 I-65 North	-12	2.792	1.062	17.67
	-18	2.390	0.4122	5.297
Site 2: I-65 Loop	-6	1.382	1.618	14.55
	-12	1.395	0.4299	3.402
	-18	1.596	0.3110	2.796
Site 3: US-421	-6	2.337	1.906	27.81
	-12	2.315	0.6691	8.594

Determination of Binder Rheology from DTT Results

The DTT test is a constant strain rate test and consequently the data can be used to define rheology of the binder relaxation modulus, E(t) for loading times used in the DTT test. The relaxation modulus E(t) was determined numerically from the DTT result by using the time-deformation information considering E(t) as the slope of the stress-strain curve. Since time is linearly related to strain, stress versus time relation can be converted to stress versus strain. The Christensen-Anderson-Marasteanu (CAM) functional fitting model was used for fitting E(t) as follows:

$$E(t) = \frac{\sigma(t)}{\varepsilon(t)} = \frac{\sigma(t)}{t.\&} \quad \textbf{(9)}$$

A relation developed by Rowe et al., (2002) was used for fitting raw stress to time data directly, seeking the 5 parameters A, B, C, D, and E.

$$(\sigma(t) - D) = 3000 \times (t - E) \times \dot{\varepsilon} \left[\left(1 + \left(\frac{t - E}{A} \right)^{B} \right)^{\left(\frac{-C}{B} \right)} \right] \quad \textbf{(10)}$$

where:

$\sigma(t)$ = stress at time t,

$\dot{\varepsilon}$ = strain rate

D = delta-stress

E = delta-time

A,B,C = constants

This determination is illustrated in Figure 29 where the tangent slope of the stress strain curve is equal to the relaxation modulus.

During the direct tension test some non-linear behavior can occur at large values of strain and/or close to the fracture strain. Consequently, in the analysis process the data used for the rheology measurements is limited to that which will be within the linear visco-elastic (LVE) limit for the binders. The LVE limit is taken from the work conducted during the Strategic Highway Research Program (Anderson et al., 1994) and implemented in the dynamic shear rheometer (DSR) test procedure TP5 (AASHTO, 1993) as follows:

$$\gamma = 12.0/(G^*)^{0.29} \quad \textbf{(11)}$$

where:

γ = shear strain in percent

G* = complex modulus in kPa

$$\gamma = e^{\left(\frac{12.044362}{G^{*0.129203}} - 1.15129497 \right)} \quad \textbf{(12)}$$

where:

G* = complex modulus in Pa

To make use of these equation E(t) is approximated to 3G* and the equations are then applied as LVE limits.

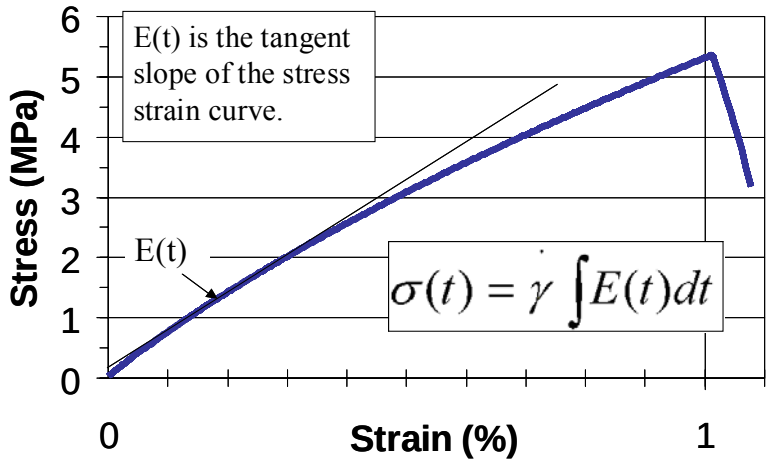

Figure 29. Determination of the relaxation modulus from the DTT.

Figure 30 illustrates the application of the LVE limits to a DTT data set. This example also shows the two stiffness isotherms. These isotherms have been calculated using the slope information and by fitting the CAM model (Rowe et al., 2002) to the data set as indicated in the figure. In addition, the lines representing the LVE limits of equations 1 and 2 are also shown. The isotherms adopted for subsequent analysis were those determined by fitting of the CAM model using start up adjustment procedures developed by Rowe et al. (2002). Isotherms from multiple tests have been combined for time-temperature shifting and the construction of master curves.

Time-temperature shifting and Construction of Master Curves from DTT Data

The software RHEA™ has been used for the development of the master curves in this project. The time temperature shifting method adopted follows the traditional approach of shifting the modulus values along the horizontal axis to form a smooth curve modulus. The shift procedures for producing a master curve were developed by various researchers. Gordon and Shaw (1994) defined various computerized methods that can be applied for the characterization of visco-elastic materials. The production of master curves involves steps as follows:

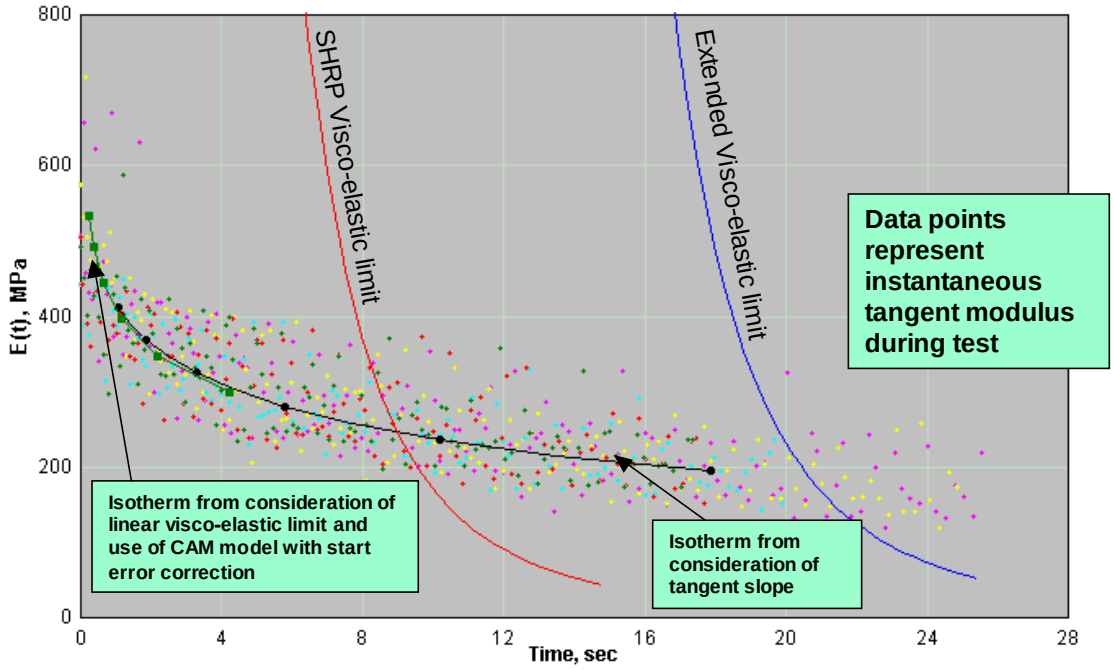

Figure 30. Application of linear visco-elastic limit for E(t).

1. An initial estimate of the shift using WLF equation (7) (Williams et al., 1955) with standard constants of C_1=17.44 and C_2= 51.6 was applied.
2. The fit was refined by using a pairwise shifting technique and straight lines representing each data set.
3. The fit was further refined using pairwise shifting with a polynomial representing the data being shifted. The order of the polynomial taken is the minimum value between (n+1), where n is the number of data points - or - Δf (the number of decades of frequency - or time).
4. WLF and Arrhenius parameters were then calculated from the resulting final shifts.

An example of the isotherms, shifted E(t) master curve (at reference temperature of –18^{o}C) and the linearized Arrhenius fit are presented in Figure 31 to Figure 33. The data defines the cold temperature rheology in the range 100 to 800 MPa, and it was merged with

DSR rheological measurements to define a more complete master curve of binder stiffness.

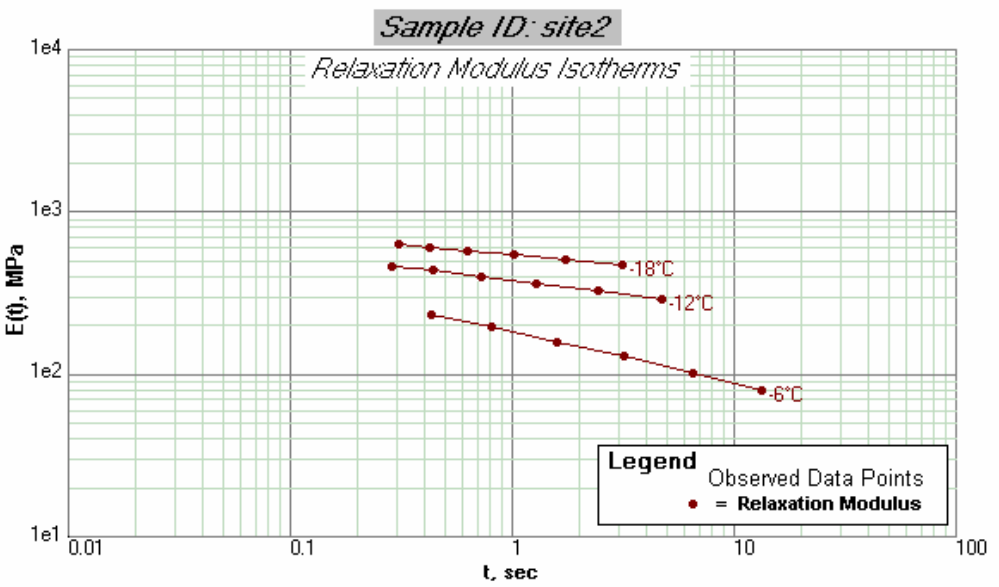

Figure 31. Isotherms of E(t) developed from the DTT.

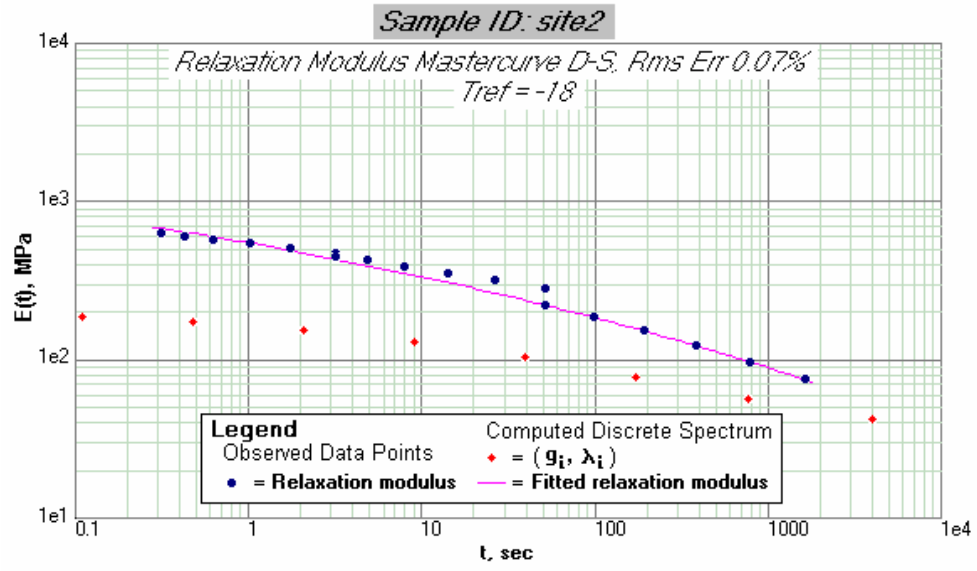

Figure 32. Master curve of E(t) developed from the DTT, Tref = -18°C

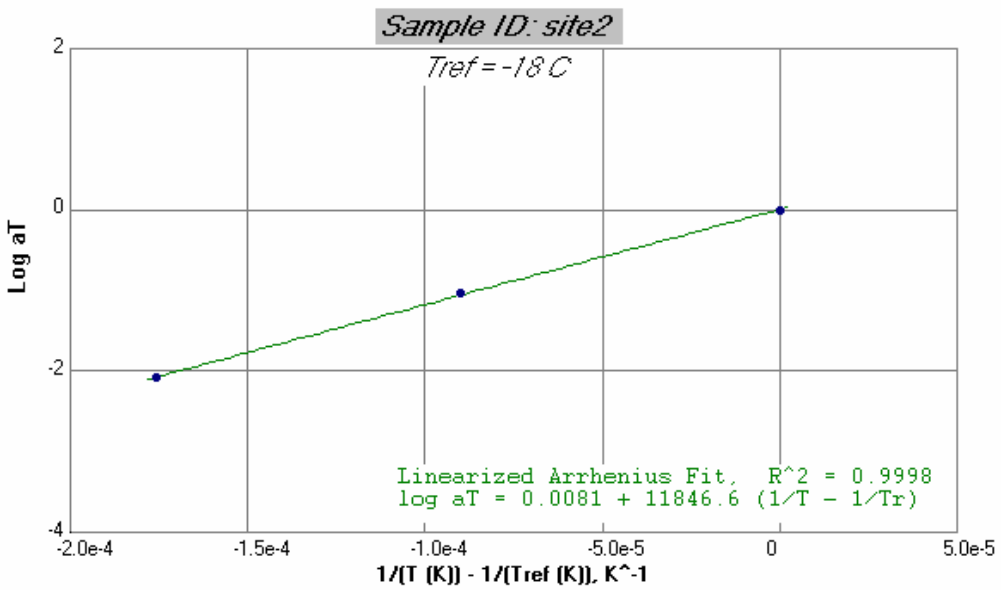

Figure 33. Linearized Arrhenius shift factors developed from the DTT.

5.2.3 Determination of Critical Cracking Temperature(CCT)

In addition, the DTT data is used to compute the critical cracking temperature as defined in the MP1A binder specification (AASHTO, 2001a) and using an adaptation of the numerical procedures defined in PP-42 (AASHTO, 2001b; Rowe et al., 2002). The computed thermal stress and measured strength data are illustrated in Figure 34. It can be observed that in two cases the direct tension test data did not intersect with the estimated stress data. In these instances the thermal strength data has been extrapolated in order that an estimation of the critical cracking temperature can be made.

The critical cracking temperature data is summarized in Table 21. Results indicate that the oldest sites (Site 1&2) have the poorest performance with the highest cracking temperature and the newest site (Site 3) has the best performance with the lowest cracking temperature. These results may reflect the effect of binder aging and the time that the sites have been in service. In addition, it should be noted that these tests have all been made on recovered binder which will affect the results to some extent – although this is not known.

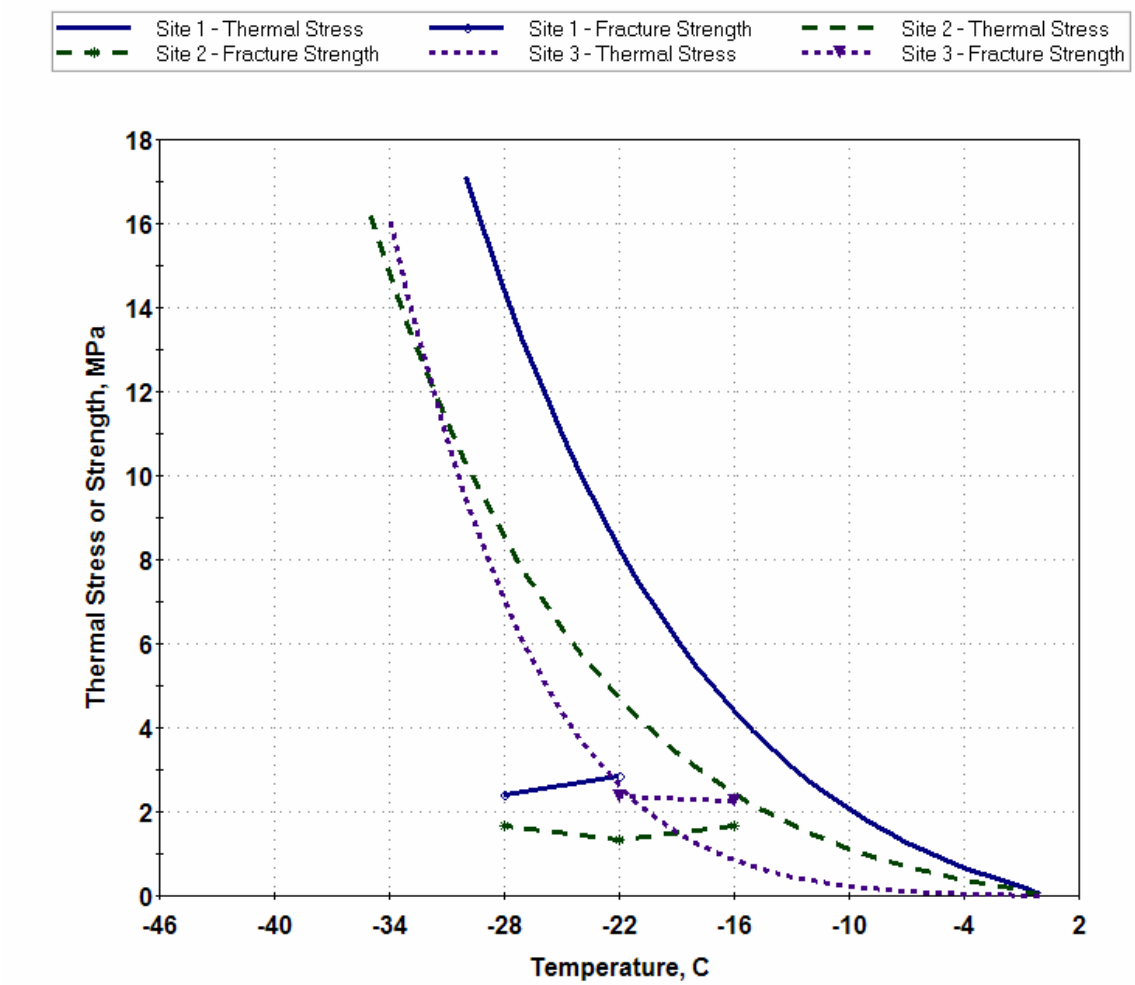

Figure 34. Thermal Stress and Strength Data - Sites 1 to 3

Table 21. Summary of Estimated Critical Cracking Temperatures for Site 1 to 3

LOCATION	**$T_{Critical}$ (°C)**
SITE 1 I-65 North of Lafayette	-13.7
SITE 2 I-65 Loop	-14.7
SITE 3 US-421 Madison	-21.4

5.2.4 Combined Binder Master Curves

Using the software tool RHEA™, the two data sets |G*| from DSR test and relaxation modulus E(t) from the DTT test were combined to produce master curves for the binder shear complex modulus |G*|. The steps in performing this analysis were as follows:

5. The storage G' and loss modulus G" data from the DSR testing was fitted with the software. The storage modulus was obtained from equation $G' = |G^*| \cos\delta$ and the loss modulus was obtained from the equation $G'' = |G^*| \sin\delta$. The constructed |G*| master-curve was adopted.
6. The computed E(t) from the DTT data was fitted with the software. The constructed relaxation modulus E(t) master curve was adopted.
7. For the combined master curve both data sets need to have the same data format. Therefore, the E(t) modulus was converted to the shear modulus, i.e., storage and loss modulus by using pseudo data points. Extensional data was converted to the shear data using the simple Poisson's ratio conversion of $G = E/[2(1+\nu)]$ with Poisson's ratio of 0.5; see Figure 35(a).
8. The combined master curve was obtained by shifting all data to the reference temperature of 25°C; see Figure 35(b).

Figure 35 shows the constructed master curve for Site 1; Figure 36 shows Site 2; and Figure 37 shows the master curve for Site 3. In each figure the first figure (a) presents the raw data or measured data without the shifting for storage modulus G' and loss modulus G". In each figure the second figure (b) shows the shifted data for the shear complex modulus |G*| as a function of reduced frequency (angular velocity in radians per second). The figures also show the measured and shifted phase angle as a function of reduced frequency. As the frequency decreases the phase angle approaches 90° indicating pure viscous material behavior.

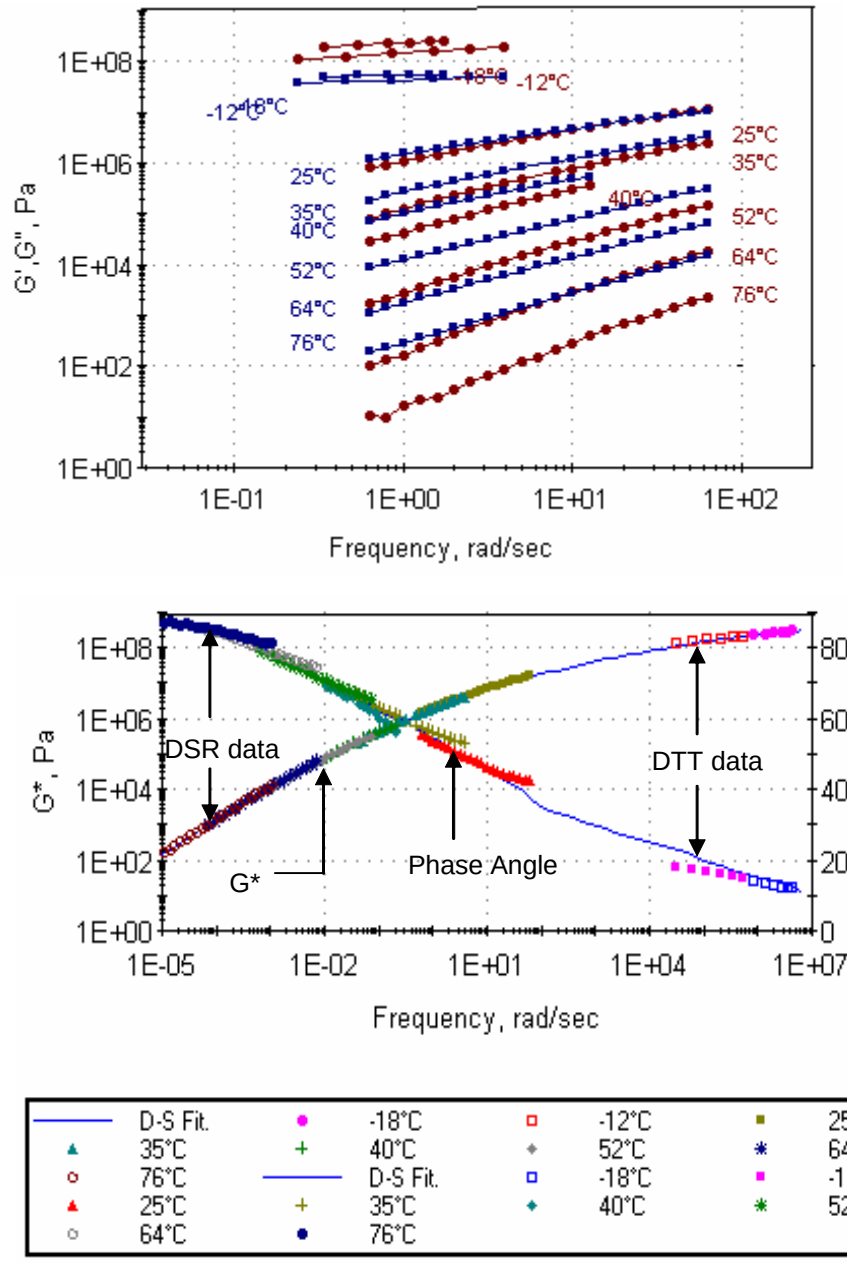

Figure 35: Master curve for shear complex modulus |G*|, Site1.

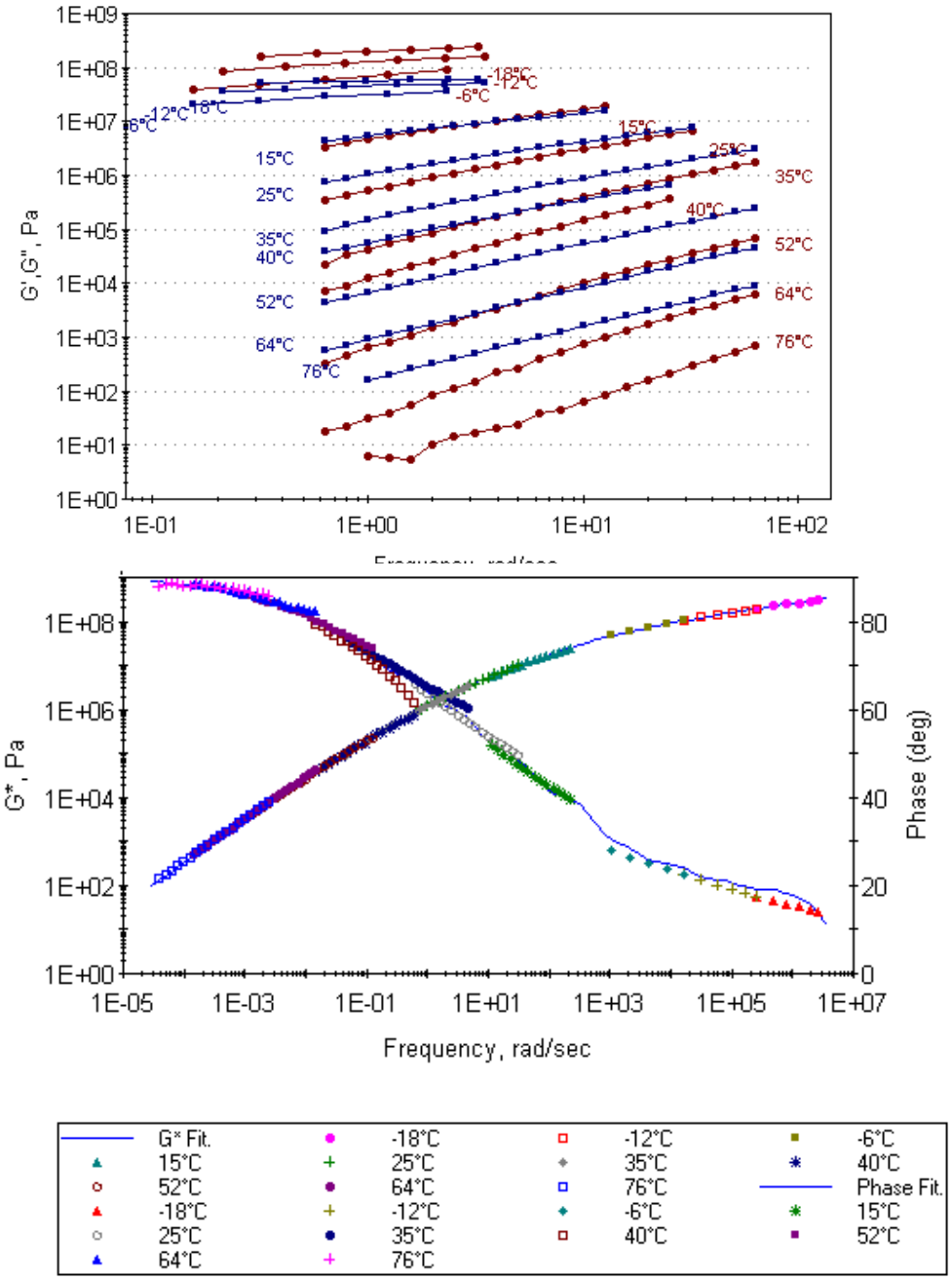

Figure 36: Master curve for shear complex modulus |G*|, Site2.

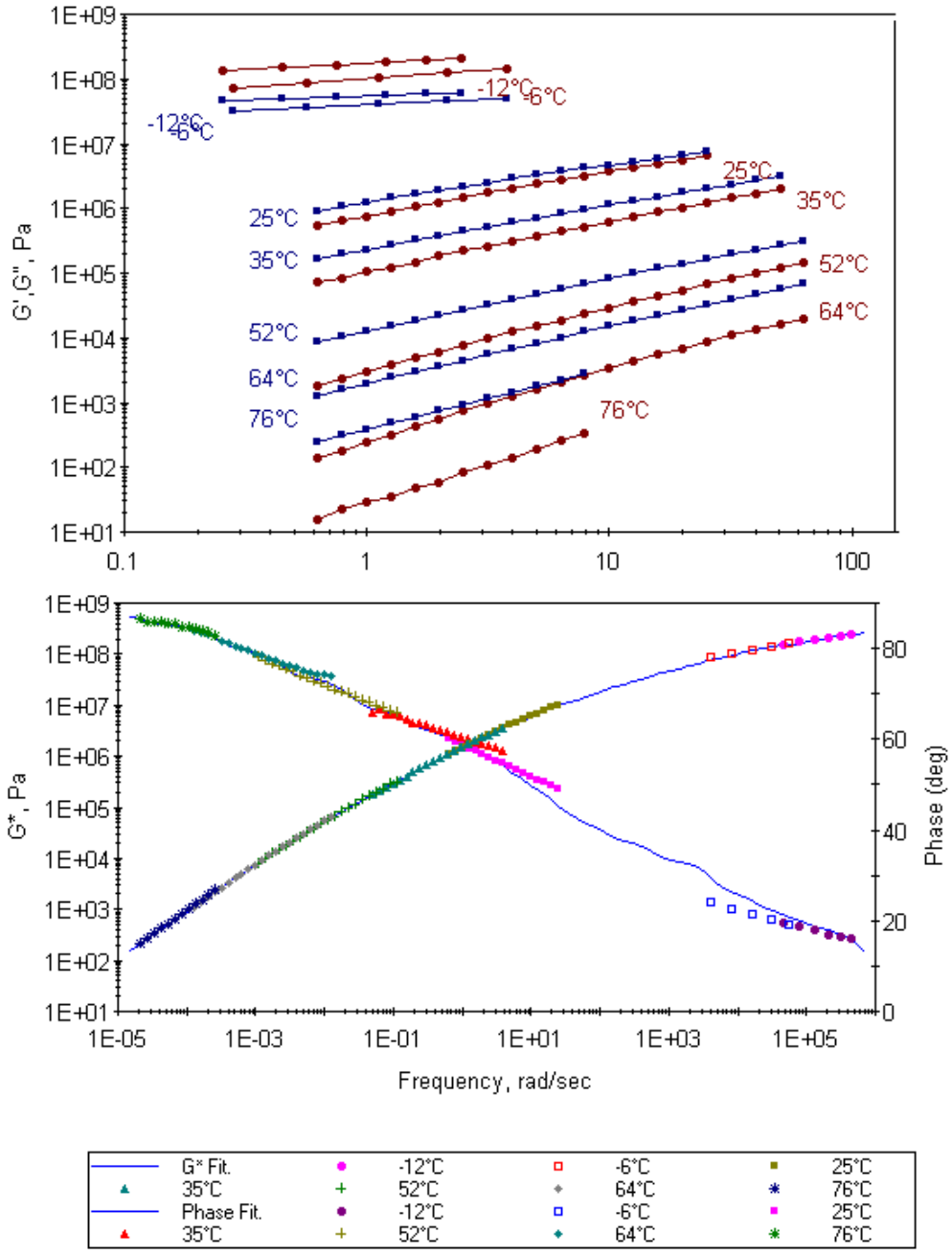

Figure 37: Master curve for shear complex modulus |G*|, Site3.

Figure 38 compares the constructed master curves. The master curves were obtained by fitting Christensen-Anderson (CA) model (Christensen & Anderson, 1992) through the data obtained from the RHEA^{TM} software. This procedure is explained in the following chapter. At high and intermediate temperatures Site 2 had the softest binder while Site 1 and Site 3 had similar binder properties. This is in agreement with the measured conventional binder properties. At low temperatures Site 3 had the stiffest binder while Site 2 still had the softest binder, although differences were not large.

From the DSR data it was estimated that the high temperature performance grade for Site 1 binder was PG 82, for Site 2 PG 76, and for Site 3 PG 82. Thus, Site 1 had aged three PG grades while Site 2 and 3 had aged two PG grades.

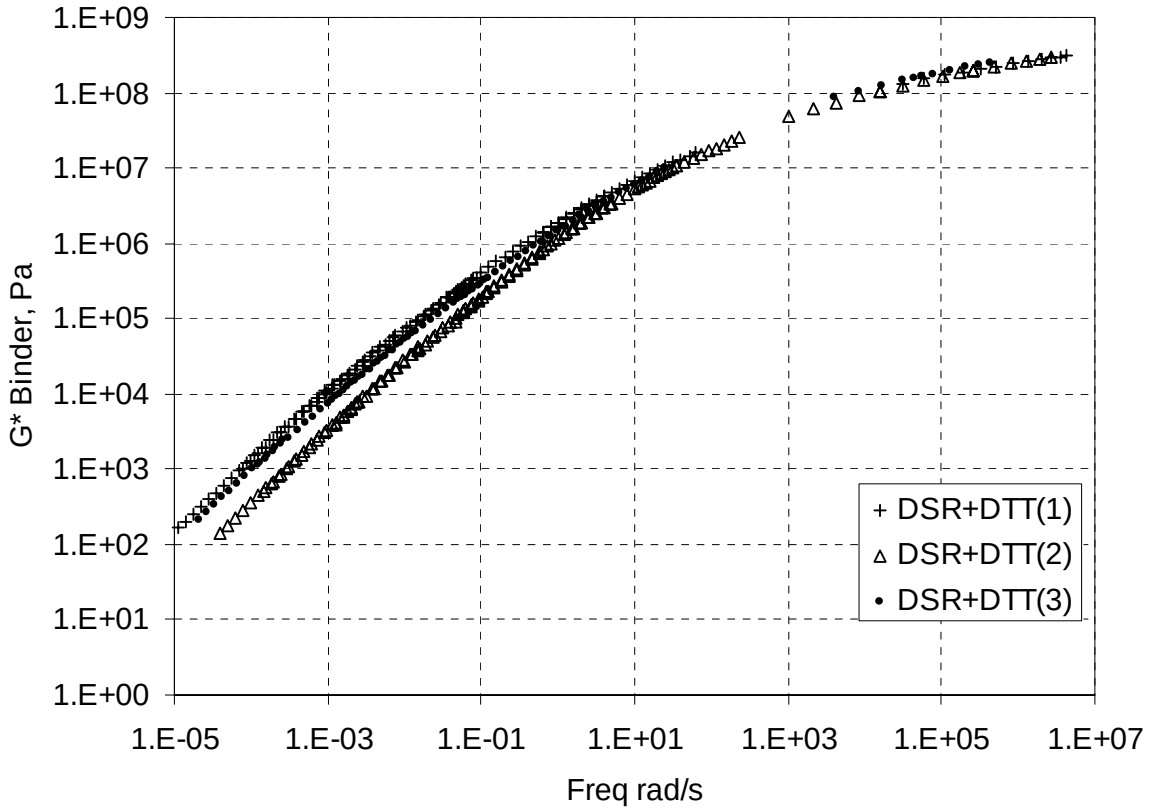

Figure 38: Comparison of binder shear stiffness |G*| master curves.

5.2.5 Relaxation Modulus

In terms of the relaxation modulus, Site 1 has a large rms (root mean square) error using the CAM relationship with a fixed glassy modulus. If the CAM relationship is used then the error reduces to 0.31% with a lower glassy modulus of 1515.7MPa. Using the CAM parameters, see Table 22, Site 3 has the largest critical time, exponent and asymptote slope. At purely viscous behavior this slope becomes 1 so it can be stated that in the range tested Site 3 demonstrates more viscous behavior compared to site 1 and 2.

Table 22: Analysis parameters using CAM model

PARAMETER	**SITE 1**	**SITE 2**	**SITE 3**
Arrhenius gradient a_1	32753.09	26668.26	29066.61
Glassy modulus (MPa)	3000	3000	3000
Critical time (sec)	956.18	0.46	720.9
Exponent	0.08	0.114652	0.136115
Asymptote log-log slope	0.340494	0.320393	0.725398
rms error %	10.01	1.22	0.9

The parameters used enable construction of the master curves as illustrated in Figure 39 from which it can be observed that the curvature results in a lower stiffness at longer loading times. The flatter slopes of Sites 1 and 2 are more indicative of oxidized materials as would be expected when considering the relative ages of the sites. The binder in Site 3 has significantly better relaxation properties (e.g. slope of master curve at loading time at approximately 60 seconds on this plot – equivalent to an m-value for a binder being considered for a –22 grade) at the conditions associated with thermal cracking. In addition, at the loading time of 60 seconds Site 3 has the lowest relaxation modulus with Site 1 having the highest which is consistent with the age of Site 3 and Site 1. Site 2 had been in service one year more than Site 1 but the binder in the mix had slightly better relaxation properties compared to Site 1. These findings are in agreement with the critical cracking temperature calculations, as expected.

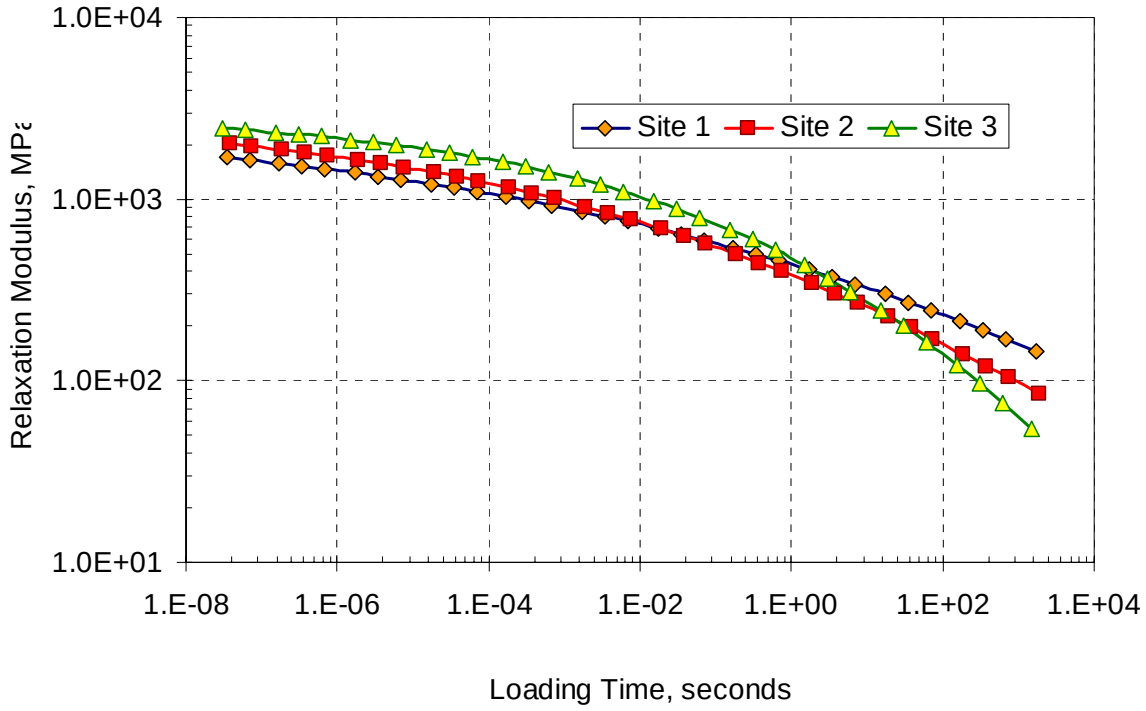

Figure 39: Relaxation modulus E(t) master curve, T_{ref} = -12°C.

5.3 Asphalt Mixture Testing and Analysis

5.3.1 SST Shear Frequency Sweep Test

The frequency sweep test at constant height with the Superpave Shear Tester (SST) was performed in accordance to AASHTO TP7 to determine the shear stiffness of the mix. Two cores were taken per site, so a total number of six cores were tested at temperatures of 4, 10, 20, 40 and 55°C. However, cores for Site 1 and 2 were too thin to be tested as is, so the two cores were glued together and tested simultaneously. Only in Site 3 were the two cores tested separately. Loading time ranged from 0.01 to 10 Hz. Test results are shown in Appendix G.

The data was analyzed using the RHEA™ software and the results are presented in graphical plots in Figure 40, Figure 41, and Figure 42. For the analysis, the reference

temperature was selected to be 25°C and glass transition temperature 0°C. The coefficient of expansion below and above the glass transition temperature was selected to be 0.00002 /°C which is within the typical range of thermal coefficient for linear expansion of hot mix asphalt (Williamson, 1972).

In the analysis of Site 1 data, one data point was removed from the coldest temperature isotherm at 4°C for shifting of the isotherms. There was some noise observed in the data points for the warmest temperature isotherm of 55°C as well. The modifications made to the raw data can be observed in Figure 40. In Site 2 data analysis, the isotherm at temperature 4°C was obviously in error and was removed from the analysis. In the analysis of Site 3 the two data sets were averaged.

Figure 43 compares the three developed master curves. Overall, at high temperatures, Site 2 had the stiffest mix, and Sites 1 and 3 had very similar mix stiffness. At cold temperatures, Site 3 had the softest mix and Site 1 and 2 had similar stiffness. This disagrees with the measured binder stiffness information because the softest binder in the high and intermediate temperatures was Site 2 binder. So the mix volumetric and aggregate properties altered the ranking of mixtures regarding the stiffness information.

5.3.2 Creep Compliance D(t) and Indirect Tensile Strength Tests

The IDT tests were performed at temperatures of -20, -10 and 0°C on triplicate specimens to determine the Creep Compliance D(t) and indirect tensile strength in accordance with the AASHTO TP9 procedure. The specimens were equilibrated at room temperature between tests which should eliminate any physical hardening. However, while inspecting the IDT data it became obvious that the data was in error and acquisition problems during testing were causing the poor data quality; the resolution for LVDTs used in the testing was apparently too large and differences in the creep data were not detected. The IDT creep data was not analyzed further due to the poor data quality.

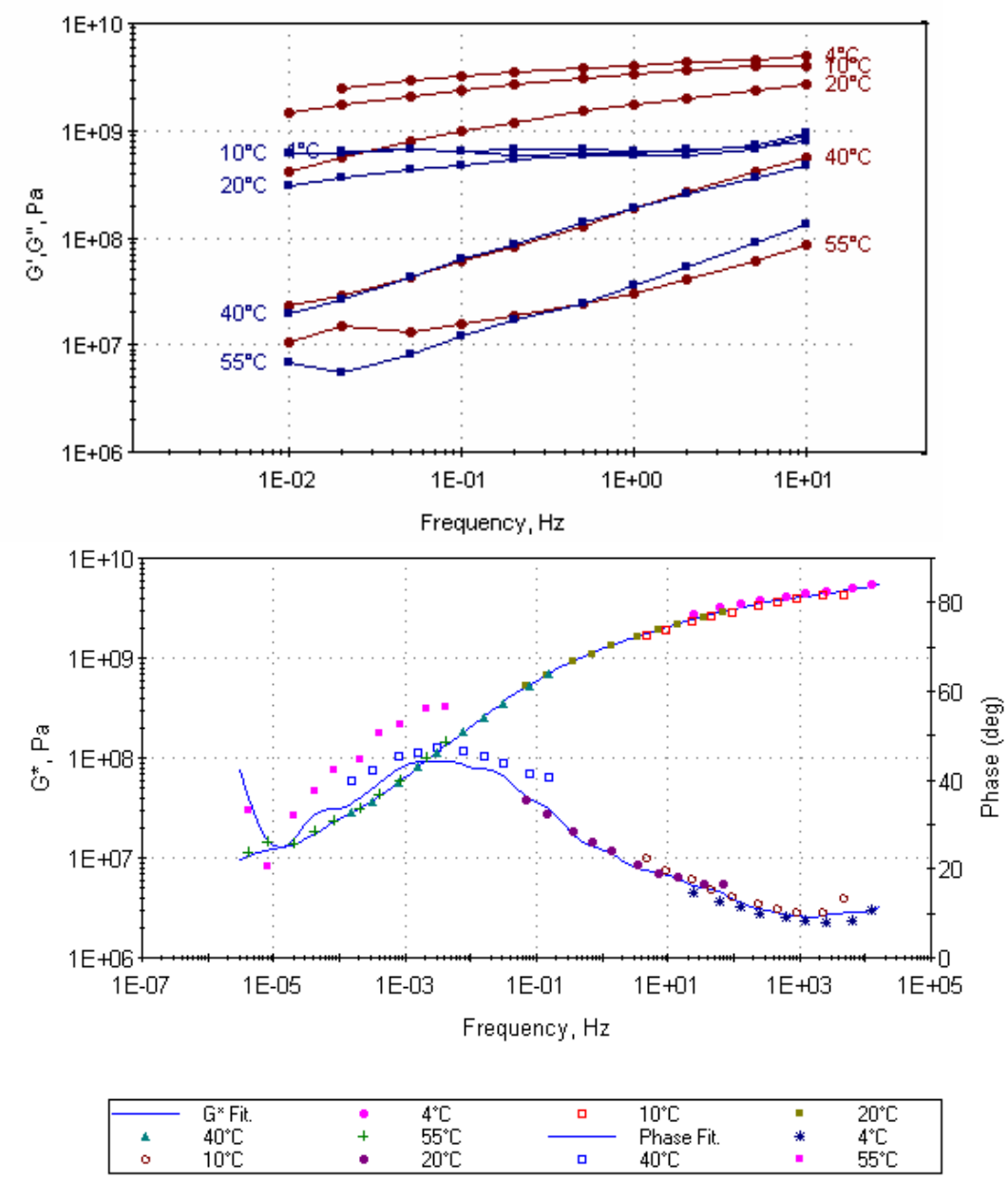

Figure 40: Master curves for Site 1 I-65 North of Lafayette

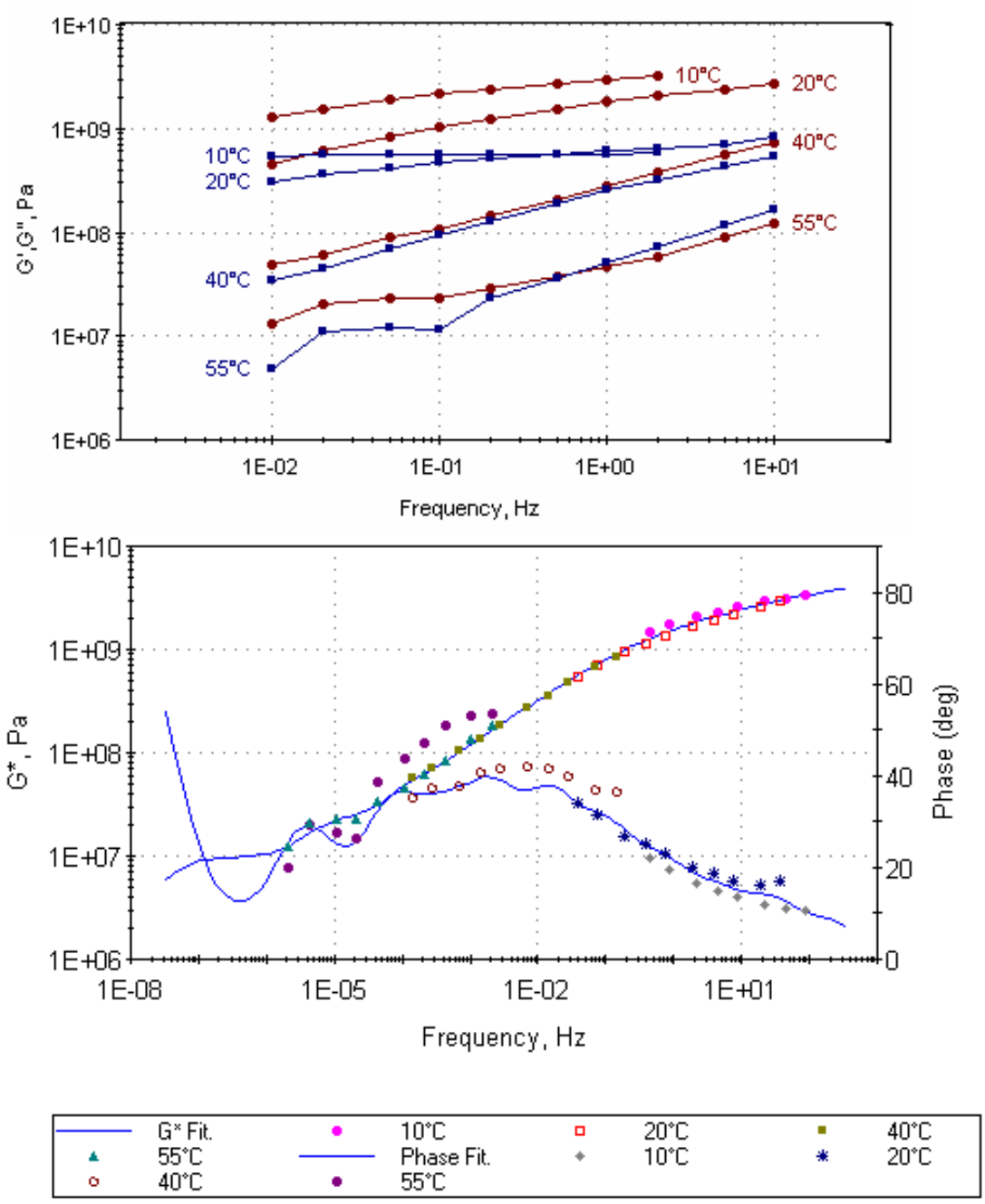

Figure 41: Master curves for Site 2 I-65 Near Indianapolis

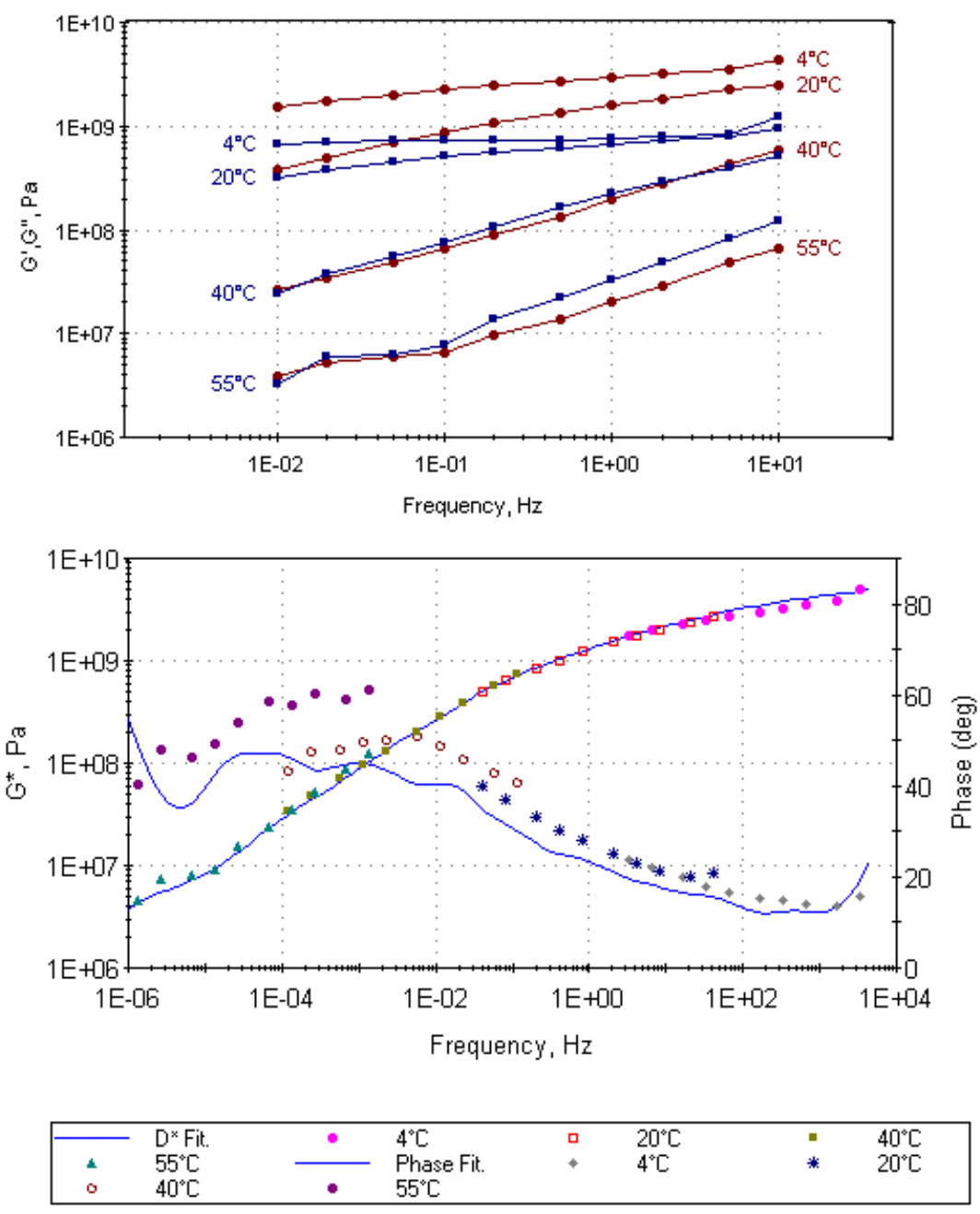

Figure 42: Master curves for Site 3 US 421 Madison

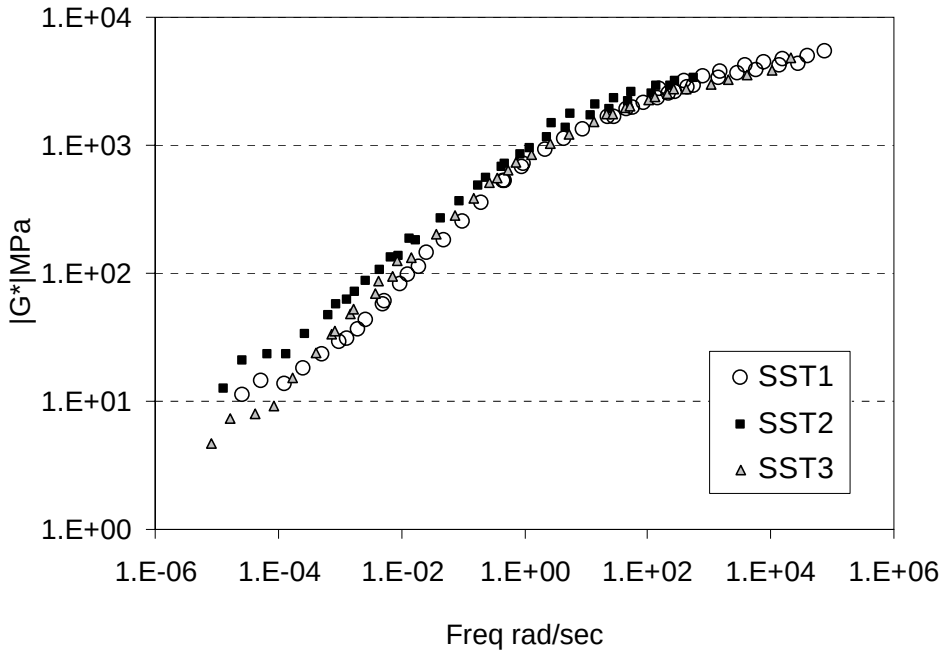

Figure 43: Summary of SST mix shear stiffness master curves.

A summary of the indirect strength data is shown in Table 23. At -20 and -10°C Site 3 had the lowest strength although the binder stiffness of Site 3 was the same as for Site 1. The low strength can be explained with the higher air void content in the mixture, see Table 23. At zero degree temperature Site 3 mix stiffness was comparable to Site 1. The better agreement was due to the lower air void content of the tested specimens for Site 3, as Table 23 indicates.

Table 23: Summary of Indirect Tensile Strength Test Results.

SITE	IDT STRENGTH (kPa)					
	-20°C		-10 °C		0°C	
	Strength	Va (%)	Strength	Va (%)	Strength	Va (%)
SITE 1 I-65 North	2505	6.6	2464	8.1	2148	7.1
SITE 2 I-65 Loop	2121	8.5	2136	8.1	1637	8.7
SITE 3 US-421	1768	10.8	1853	10.2	2022	9.4

6 VISCO-ELASTIC 3-D FINITE ELEMENT MODELING

The research approach for the analysis of top-down cracked pavements included the Finite Element analysis of stress/strain distribution at the top of the pavement surface. The analysis made use of material property sets determined from analysis of FWD and laboratory test data, a climatic effects model, and a 3-D visco-elastic finite element model, as illustrated in Figure 44.

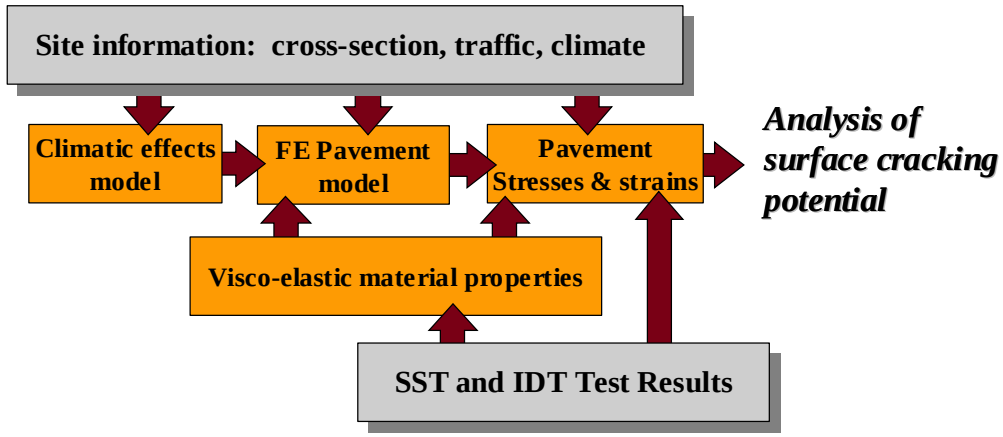

Figure 44. Analysis scheme.

The objective for the material model development for mix and binder properties was to obtain the relationships to describe the complex dynamic modulus and phase angle, for a range of pavement temperatures between -20˚C to 54˚C for the FE analysis. The approaches considered were a combination of the Superpave Shear Test (SST) and Indirect Tensile Test (IDT) datasets for the mix, and the combination of Dynamic Shear Rheometer (DSR) and Direct Tensile Test (DTT) datasets for the binder. The assumptions, procedures and parameters in the development of these models have been explained in detail in the following sections.

6.1 Development of Material Models for FE Analysis

6.1.1 Base Binder Model

For the development of the material model for the binder, separate base course and surface binder data sets were used. For the base course binder, pavement layer thickness information was collected for the three study sites and was verified that the HMA base layer was a typical AC 20 binder (comparable to PG 64-22). Since the binder properties were not evaluated for the base course layer, the calculations have been performed using a typical AC-20 binder data set (Rowe and Pellinen, 2002). The Dynamic Shear Rheometer (DSR) test data for a range of temperatures from 15˚C to 80˚C after rolling thin film oven (RTFOT) aging was used with Bending Beam Rheometer (BBR) data conducted at temperatures of -18, -24 and -30˚C. The two data sets were merged to obtain binder properties over the wide range of temperatures -30˚C to 80˚C which was comparable to the range of temperature of our interest from -20 to 55˚C.

The Christensen-Anderson (CA) model was fitted to the binder master curve to determine the parameters in the equation:

$$\left|G^*(\omega)\right| = Gg[1 + (\omega_c / \omega)^{(\log 2)/R}]^{-R/\log 2} \quad \textbf{(13)}$$

$$\delta(\omega) = \frac{90}{1 + (\omega / \omega_c)^{(\log 2)/R}} \quad \textbf{(14)}$$

where:

$\|G^*(\omega)\|$	= Complex shear modulus
G_g	= Glassy modulus, typically 1 GPa
ωc	= Crossover frequency, rad/s
R	= Rheological index
$\delta(\omega)$	= Phase angle, in degrees

A good fit was observed when the binder data, |G*|, and phase angle were obtained as illustrated in Figure 45. The parameters of the CA model, glassy modulus G_g, crossover frequency ω_c and rheological index R for the binder were determined using the corresponding WLF parameters at the reference of temperature 15˚C, see Table 24.

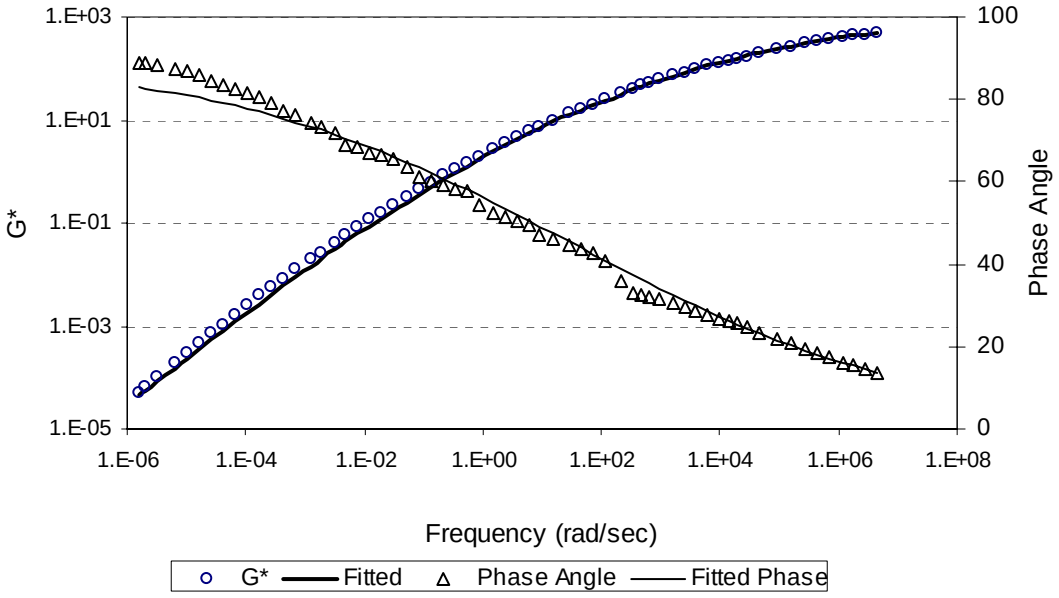

Figure 45: CA fit for binder |G*| and phase angle for all site for base binder.

Table 24: Parameters for CA model for base binder

MASTER CURVE PARAMETERS FOR BASE BINDER		
Glassy Modulus	G_g (MPa)	1542
Rheological Index	R	2.06438
Crossover Frequency	ω_c (rad/sec)	32.44
Reference Temperature	T_R ˚C	15
WLF RELATION		
Constants C1 and C2	C1	22.77
	C2	184.7
Reference Temperature	T_R ˚C	15
Glassy Temperature	T_g ˚C	-20

6.1.2 Surface Binder Model

For the surface binder analysis, the Dynamic Shear Rheometer (DSR) |G*| data and the Direct Tension Test (DTT) relaxation modulus E(t) data were merged to provide a combined dataset which encompasses the entire range of pavement temperatures. The combined data set analyzed in Chapter 5 was used for the model development for the binder properties. A separate master curve model for binder properties in addition to the master curve development using RHEA software was needed to get the master curve in the form that subsequent FE analysis would be efficient and fast.

Figure 46, Figure 47, and Figure 48 illustrate plots of master curve of shear complex modulus |G*| and phase angle δ for the surface mix binders using CA fitting function, as described above. The parameters for the CA model, glassy modulus G_g, crossover frequency ω_c, and rheological index R were determined using a non linear least square fit and the corresponding WLF parameters at the same reference temperature of 25˚C are presented in Table 25.

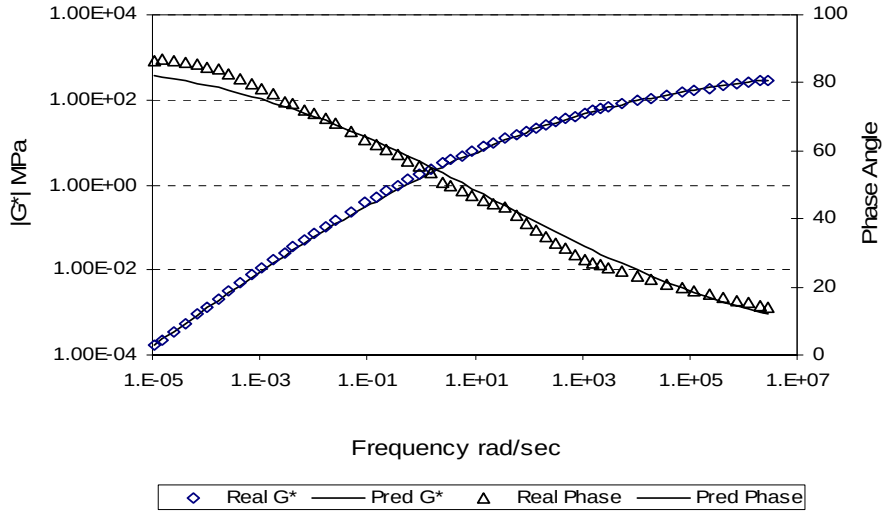

Figure 46: C-A fit for G* and phase angle for Site 1 surface binder.

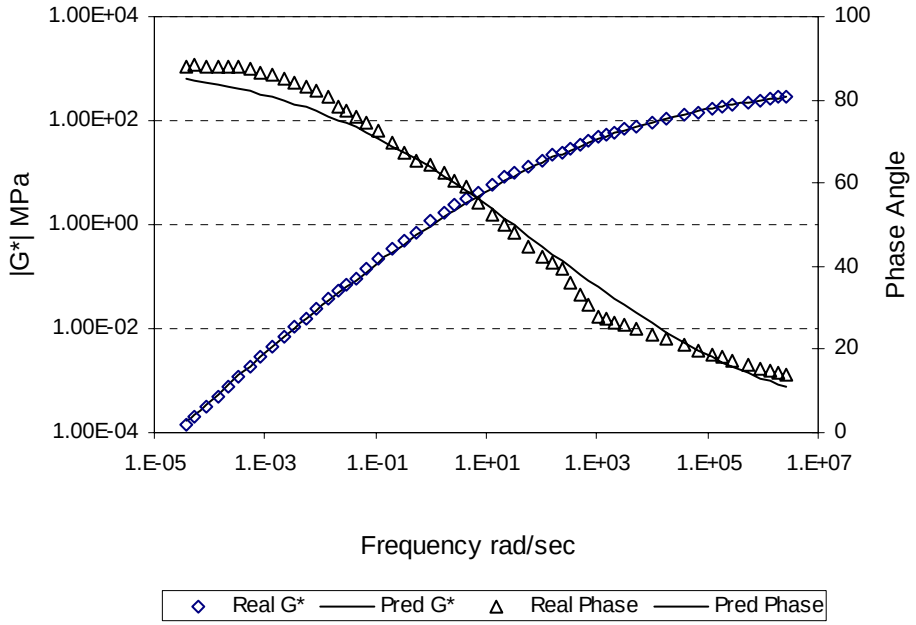

Figure 47: C-A fit for G* and phase angle for Site 2 surface binder.

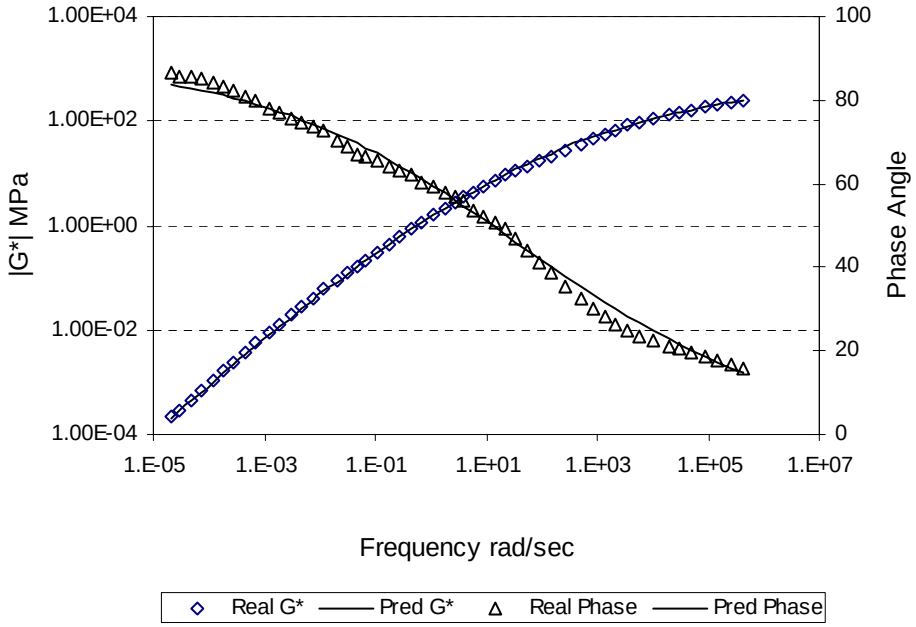

Figure 48: CA fit for binder |G*| and phase angle for Site 3 surface binder.

Table 25: Parameters for CA model for surface binder

MASTER CURVE PARAMETERS				
	Symbol	**Site 1**	**Site 2**	**Site 3**
Glassy Modulus	G_g (MPa)	713.2	564.3	662.6
Rheological Index	R	1.87469	1.56266	1.68473
Crossover Frequency	ω_c (rad/sec)	26.2758	97.9859	45.3541
Reference Temperature	T_R ˚C	25	25	25
WLF RELATION				
Constants C_1 and C_2	C_1	29.58	23.39	21.23
	C_2	259.94	214.18	187.3
Reference Temperature	TR ˚C	25	25	25
Glassy Temperature	T_g ˚C	-20	-20	-20

6.1.3 Selected Mix Stiffness Approach

In the analysis of the mix data, the Superpave Shear Test (SST) dataset and the Indirect Tensile Test (IDT) data set were going to be merged to provide a combined data set which encompasses the entire range of pavement temperatures from -20˚C to 55˚C. The combined data set analyzed in Chapter 5 was used for a model development for the mix properties.

Due to the errors in the IDT data the combined master curves for Sites 2 and 3 could not be developed. An alternative approach was selected to obtain the needed mixture stiffness for the FE analysis employing stiffness predictive equations. The Hirsch model, based on composite material behavior, is a fundamental material model approach for determining the mix stiffness (Christensen, Pellinen, and Bonaquist, 2002). The stiffness modulus of the asphalt mix can be directly estimated from binder modulus, voids in mineral aggregate (VMA) and voids filled with asphalt binder (VFA). The model for the dynamic complex extensional modulus |E*| is given by:

$$|E^*|_{mix} = P_c\left[4{,}200{,}000\left(1-\frac{VMA}{100}\right)+3\,|G^*|_{binder}\left(\frac{VFA\times VMA}{10{,}000}\right)\right] + (1-P_c)\left[\frac{1-VMA/100}{4{,}200{,}000}+\frac{VMA}{3VFA\,|G^*|_{binder}}\right]^{-1} \quad \textbf{(15)}$$

where:

P_c = aggregate contact volume, as a volume fraction

$$P_c = \frac{\left(20+\frac{VFA\times 3\,|G^*|_{binder}}{VMA}\right)^{0.58}}{650+\left(\frac{VFA\times 3\,|G^*|_{binder}}{VMA}\right)^{0.58}} \quad \textbf{(16)}$$

The aggregate contact volume, P_c, is the portion of aggregate particles in intimate contact with each other. As the aggregate contact volume increases, the modulus and strength also increases. High values of P_c indicate very effective structures producing good strengths and stiffness which is typical at low temperatures. Low values of P_c indicate structure with low strength and stiffness and tend to occur at high temperatures.

The parameters required for the Hirsch model can be calculated from the volumetric composition of the mixture using Equations (15) and (16), where V_a is air voids and V_{beff} is the effective binder volume.

$$VMA = V_{beff} + V_a \quad \textbf{(17)}$$

$$VFA = \left(\frac{V_{beff}}{V_{beff}+V_a}\right)*100 \quad \textbf{(18)}$$

The parameters required for the Hirsch model were calculated from the measured volumetric composition of the studied mixtures. The VMA and VFA values are shown in Table 18. The binder stiffness $|G^*|_{binder}$ was obtained from the developed CA fitted binder

master curves, discussed above.

Figure 49 compares the mix master curves obtained by fitting only the SST mix data and predicted stiffness master curves using the Hirsch predictive model. The SST master curve was converted to uniaxial loading mode by Equation $|G^*| = 0.0603\ |E^*|^{1.0887}$. The SST master curves gave lower values for the mixture stiffness at high temperature with as low as 10 MPa. This suggests that the SST data is not giving comparable mix stiffness values in relation to the uniaxially measured stiffness. Therefore, it was decided that the predicted mix stiffness was used in the subsequent FE analysis.

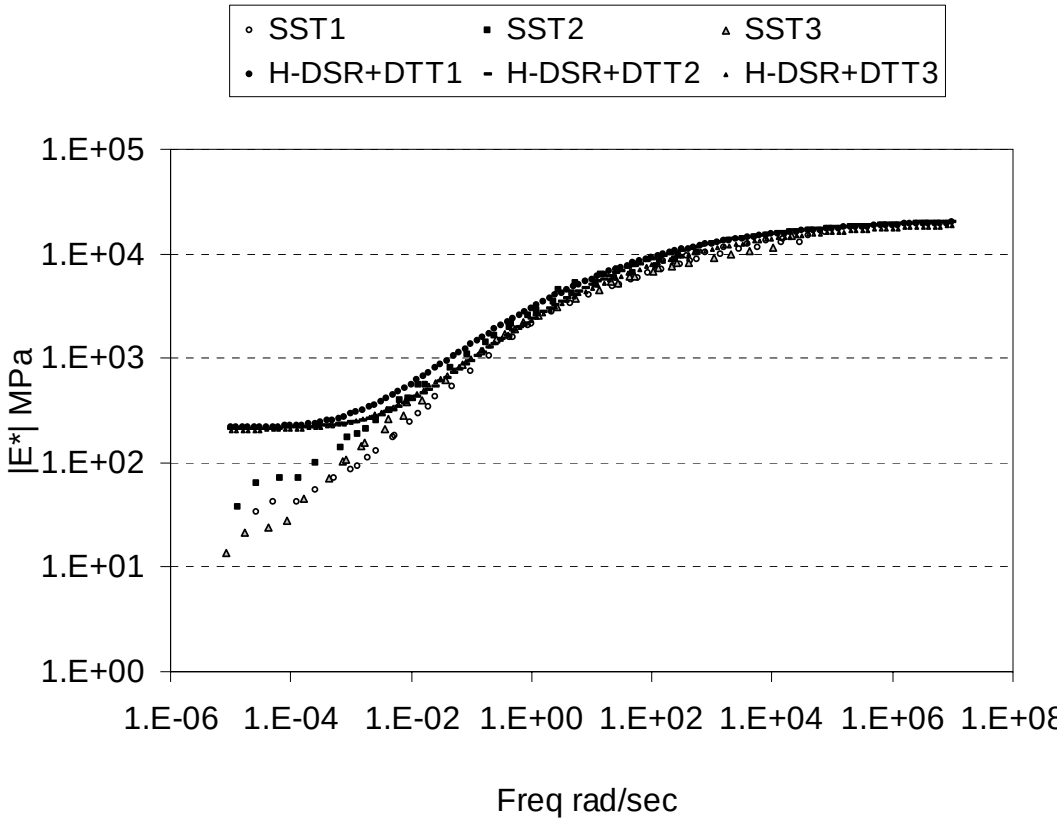

Figure 49: Comparison of mix master curves.

6.1.4 Visco-elastic Model Development for FE Analysis

For the analysis of the pavement structure, a linear visco-elastic rheological model

was employed. Work initially concentrated on the use of the Burger's model since it was considered that this would be adequate to consider the range of loading times of interest. This aspect was investigated by performing an analysis of a pulse load on a cylindrical specimen. The pulse load time was chosen to be similar to the traffic speeds to be used in the finite element analysis. This analysis of the pulse suggested that in order to describe the shape of the load and deformation response the five relaxation times are needed. Consequently, the standard two element representation of the Burgers' model was replaced with the more generalized five element model. The parameters for the model were obtained by fitting relaxation spectra using stiffness data from the Hirsch model.

6.2 Mesh Design and Gaussian Quadrature

During the 1990's Rowe, Brown, Sharrock and Bouldin (1995) developed a finite element analysis approach for pavement design. A modification to this software is proposed for the analysis of the pavement structures for surface cracking propensity. The analysis method can deal with the visco-elastic nature properties of asphalt materials, allows temperature depth gradients to be modeled, enables the definition of complex wheel loads and allows materials to be damaged at different rates within the pavement structure.

The software consists of a "core" FE program that interacts with other programs and subroutines that provide information on material properties, pavement temperatures and traffic conditions. The greater part of the existing finite element code, initially drawn upon for program development, is based on work described by Owen and Hinton (1980).

6.2.1 Pavement Depths at Gauss Points

In the 3-D finite element analysis of the pavement structure, the stresses and strains are obtained at the four Gauss points of the 20 node element chosen to represent the HMA layers. The pavement depths have been calculated corresponding to the Gauss points and tabulated in Table 26. Climatic data at distances D1 and D2, shown in Table 26, from the

surface of the pavement are analyzed for obtaining the temperatures corresponding to these points.

Table 26: Pavement Depths corresponding to Gauss Points for FE analysis

SITE 1 I-65 NORTH OF LAFAYETTE							
	Depth of HMA Layers (in)	**Depth of HMA Layers (mm)**	**Layer/2**	**Gauss Pt#2**	**Distance above and below Centerline**	**Distance1 From Top D1**	**Distance 2 From Top D2**
Layer 1	1.5	38.1	19.05	0.577	10.99852	8.1	27.1
Layer 2	13	330.2	165.1	0.577	95.32053	107.9	273.0
SITE 2 I-65 NEAR INDIANAPOLIS							
	Depth of HMA Layers (in)	**Depth of HMA Layers (mm)**	**Layer/2**	**Gauss Pt#2**	**Distance above and below Centerline**	**Distance1 From Top D1**	**Distance 2 From Top D2**
Layer 1	1	25.4	12.7	0.577	7.332348	5.4	18.1
Layer 2	20.5	520.7	260.35	0.577	150.3131	135.4	395.8
SITE 3 US 421 MADISON							
	Depth of HMA Layers (in)	**Depth of HMA Layers (mm)**	**Layer/2**	**Gauss Pt#2**	**Distance above and below Centerline**	**Distance1 From Top D1**	**Distance 2 From Top D2**
Layer 1	1.25	31.75	15.875	0.577	9.165436	6.7	22.6
Layer 2	6.75	171.45	85.725	0.577	49.49335	68.0	153.7

A pavement representation for Site 1, I-65 North of Lafayette, indicating the position of Gauss points is shown in Figure 50.

6.2.2 Pavement Temperatures

Climatic factors play a dominating role in asphalt pavement design procedures since they affect permanent deformation and fatigue cracking as well as other modes of pavement distress. In order to enable a rigorous analysis of climatic effects to be

introduced, a FE heat flow model was used to generate 24 temperature-depth profiles, one for each hour of the day. The calculations are repeated for twelve periods corresponding to each of the twelve months of the year. The model uses an energy balance calculation with boundary conditions that consist of a heat transfer coefficient used in conjunction with air temperature, together with a radiation flux, at the upper surface and a fixed temperature at 1 m depth, equal to the average monthly air temperature. The computation is started at dawn, assuming a constant temperature with depth for simplicity. The heat flow equations are integrated by an explicit time stepping procedure, while, simultaneously, the heat transfer conditions at the surface are varied with time according to the predetermined patterns of air temperature together with direct and diffuse radiation. After 24 hours, dawn again is reached. The temperature-depth variation found at this time is treated as a new estimate of the starting conditions and the time stepping process is repeated for another 24 hours. In this way, successive approximations to the initial boundary conditions are obtained. When the initial and final states of the 24-hour period match closely, the desired solution for the period has been determined. The radiation at the surface is obtained as follows:

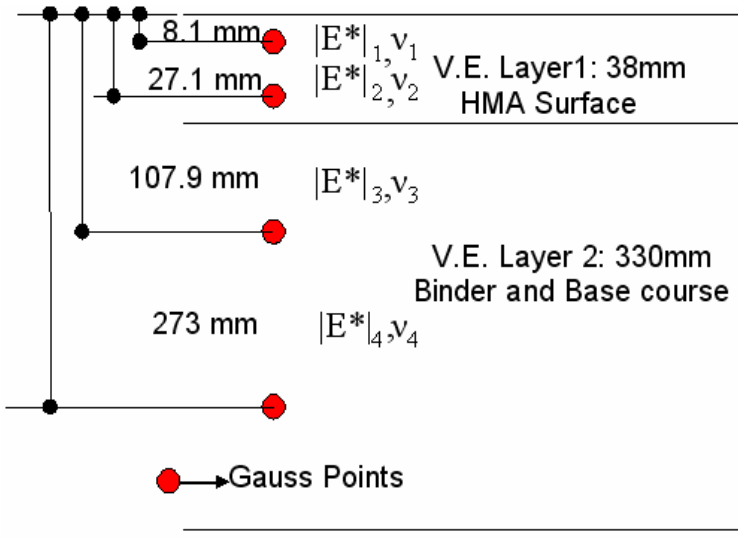

Figure 50: Pavement Representation for Site 1 I-65 North

Day: A mean value of solar constant of 1362 W/m^2 is assumed, i.e. the radiation intensity normal to the sun's direction above the earth's atmosphere. This is taken to vary seasonally by +/- 3.5% due to the varying radius of the earth's orbit. Generally accepted published information on the proportion of the radiation reaching the ground is assumed, dependent on the elevation of the sun, the height above sea level and cloud cover. An absorbtivity of 0.9 is taken for the asphaltic materials.

Night: A constant re-radiation of 120 W/m^2 to space is assumed. This is developed and terminated linearly during the first hour and last hour of darkness, to give a pattern continuous with the daytime radiation input.

An approximate daily variation of air temperature for each month is constructed from average daily maximum and minimum temperatures, with an allowance of plus and minus a number of standard deviations to cover the required proportion of the extremes, varying linearly with maximum and minimum temperature over the year. Together with the computed surface temperature, this defines the remaining surface heat transfer, using a heat transfer coefficient of 23 W/m^2/^{o}C.

The heat flow calculation is done iteratively, employing the previously mentioned FE method. Typical thermal properties are assumed for the asphaltic mixture as follows:

- Conductivity (K_c) 1.5 w/m.^{o}K
- Mass Density (ρ) 2400 kg/m^3
- Specific Heat (Cp) 960 J/kg.^{o}K

The above properties are used to obtain diffusivity, as follows:

$$\kappa = \frac{K_c}{(\rho \, x \, Cp)} \qquad (19)$$

Thus, the default value used in the FE heat flow calculations for diffusivity is 6.51e-7 m^2/s.

The result from this analysis is 288 temperature depth gradients (24 for each month of the year) with a single gradient representing a typical hour of one of the 12-months.

Statistical bias can be applied to the calculated temperature depth gradients – for example the computations can be performed for mean conditions or for conditions representing a high or low multiple of the standard deviation from the mean. This statistical aspect is of considerable importance since damage to asphalt mixtures occurs generally at the extreme of climatic conditions – both for plastic flow and cracking.

This entire computation procedure has recently been calibrated (Pellinen et al., 2004) against data collected from the WesTrack program and, while computationally is marginally different from the procedure implemented with the new NCHRP 1-37A design method, it allows rapid computation of effects due to the manner in which it is integrated with other analysis tools.

Pavement temperatures are available from a 10-year climatic database file collected during the Strategic Highway Research Program (Rowe, 1996). These data files were analyzed to produce pavement temperature depth profiles for the state of Indiana. With the LeapsPro^{TM} Software, the envelope of annual temperature depth variation was obtained for each study site. Figure 51 shows the temperature depth variation. The hourly temperature variation data for each month were also recorded. The maximum and minimum temperatures are summarized and presented in Table 27.

Table 27: Maximum and Minimum pavement temperature-depth values

SITE 1			**SITE 2**			**SITE 3**		
Depth (mm)	**T_{min}**	**T_{max}**	**Depth (mm)**	**T_{min}**	**T_{max}**	**Depth (mm)**	**T_{min}**	**T_{max}**
0	-23.32	56.92	0	-20.34	57.15	0	-16.56	57.54
25	-22.19	53.91	25	-19.27	54.08	25	-15.49	54.45
50	-21.25	51.43	50	-18.38	51.66	50	-14.6	52.06
75	-20.62	49.36	75	-17.77	49.54	75	-13.99	49.92
100	-20.01	47.4	100	-17.21	47.62	100	-13.42	48.03
125	-19.38	45.64	125	-16.61	45.81	125	-12.82	46.2
150	-18.75	44.03	150	-16.01	44.17	150	-12.22	44.59
200	-17.9	41.52	200	-15.28	41.83	200	-11.5	42.25
250	-17.31	39.51	250	-14.66	39.63	250	-10.88	40.09
300	-16.86	37.81	300	-14.24	37.93	300	-10.47	38.4

Figure 51 shows the plot of annual maximum and minimum temperature depth variation for Site 1 I-65 North of Lafayette. The minimum temperature was -23.32ºC and the maximum temperature was 56.92ºC.

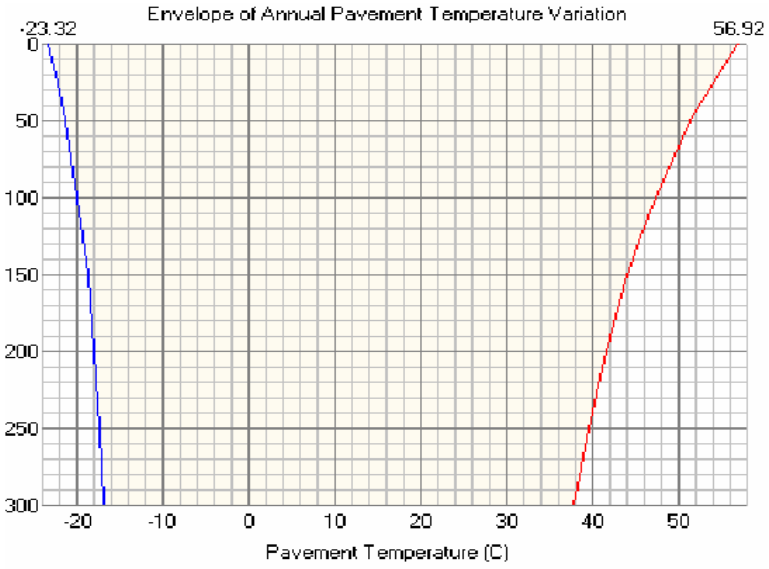

Figure 51: Site 1 Annual temperature-depth variation

After obtaining the pavement temperature-depth gradient in Table 27, the temperatures at Gauss points are calculated by fitting a climatic model to the temperature depth curve. This method is automated in some of the software application previously developed and involves fitting the data computed by the climatic effects model with six parameters (P_1 P_2 P_3 P_4 P_5 and P_6). The gradients are expressed in an exponential form given by:

$$T(z) = P_1 + P_2 e^{-2z} + P_3 e^{-5z} + P_4 e^{-8z} + P_5 e^{-11z} + P_6 e^{-14z} \qquad \textbf{(20)}$$

where:

t = Temperature, °C

z = Depth, m

$P_1 – P_6$ = Fitting parameters

While this approach has been found acceptable in automated procedures a similar procedure was used to interpolate data from the model by fitting a third order polynomial to the plot of recorded maximum and minimum temperature data. The fit obtained by this procedure proved sufficiently accurate to enable a good interpolation of the temperatures at various depths for this project.

The temperature corresponding to the Gauss points were obtained using the climatic model for each site. The temperature-depth values at the Gauss points are presented in Table 28.

Table 28: Temperature at gauss points for FE analysis

SITE 1			**SITE 2**			**SITE 3**		
Depth mm	**Temp max**	**Temp min**	**Depth mm**	**Temp max**	**Temp min**	**Depth mm**	**Temp max**	**Temp min**
HMA Layer 1			HMA Layer 1			HMA Layer 1		
8.1	55.89	-22.9	5.4	56.42	-20.05	6.7	56.65	-16.22
27.1	53.82	-22.17	18.1	54.97	-19.57	22.6	54.87	-15.62
HMA Layer 2			HMA Layer 2			HMA Layer 2		
107.9	47.09	-19.68	135.4	45.52	-16.26	68	50.55	-14.14
273	40.57	-16.94	395.8	37.84	-12.91	153.7	44.95	-12.11

6.2.3 Loading Time/ Frequency

The loading time and frequencies were calculated for a typical range of vehicular speed of 35 to 60 mph. The relationship between the thickness of HMA layer (mm), vehicle speed (km/hr) and loading time (s) is given by:

$$\log t = 5 \times 10^{-4} h - 0.2 - 0.94 \log V \qquad (21)$$

The lowest loading frequency was 22 rad/sec and the highest frequency was 73.8 rad/sec. With reference to the maximum and minimum loading frequency at each site, a decade of frequency (10-100 rad/sec) was selected for the calculation of stiffness of the mix for the finite element model using the Burger's model discussed in Section 6.1.4.

6.3 Wheel Load Modeling

The wheel load was decomposed into a contact area made up of 120 sub-patches, each of which can have a normal and shear component applied. Consequently, transverse and longitudinal forces associated with the tire loading were combined into a single force vector that acts on the surface of the loaded sub-patch.

The contact patch is time-stepped across the problem. This makes the analysis relatively complex and time consuming. This is the reason that the relaxation modes and visco-elastic layers are limited to two and the grid size was not further refined, thereby enabling the problem to be solved on a PC with a reasonable degree of accuracy.

There are some important observations with regards to tire loading:

- Stress reversals exist across each rib
- Stress reversals longitudinally- compression in front and tension at rear
- Higher stresses on outside rib of radial tires
- Result is a complex stress distribution
- Tire loading is simplified into multiple contact patches with normal and shear loading

The wheel load has been decomposed into a contact area made up of 120 sub-patches, each of which can have a normal and shear component applied. Consequently, transverse and longitudinal forces associated with the tire loading have been combined into a single force vector that acts on the surface of the loaded sub-patch. The model makes use of a finite-element model (Zienkiewicz, Nayak & Owen, 1972; Owen et al., 1980; Owen, Prakash and Zienkiewicz, 1974) with quadratic hexahedral elements visco-elastic elements representing the asphalt material as shown in Figure 52.

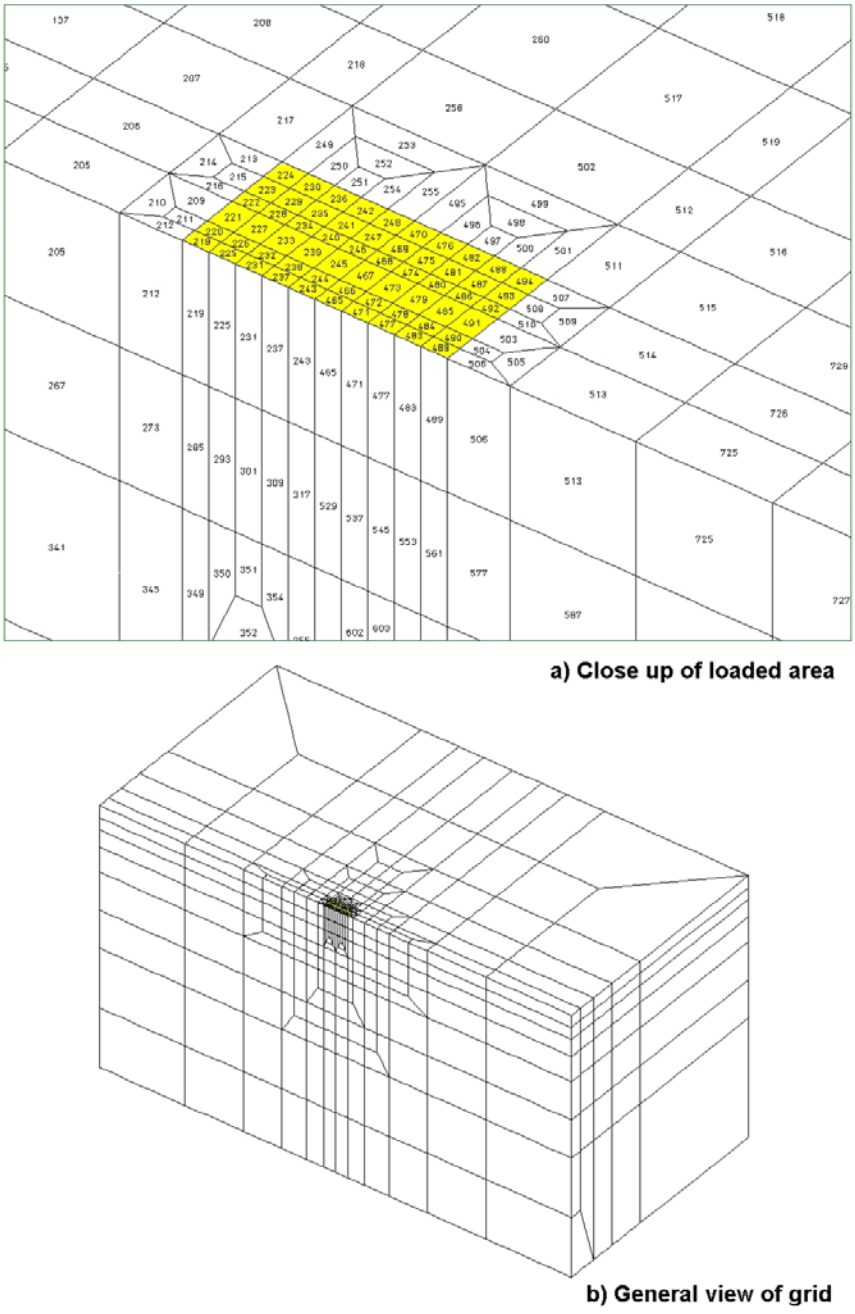

Figure 52: Mesh used to represent complex wheel loading on 3-D analysis.

The contact patch is time-stepped across the problem. This makes the analysis relatively complex and time consuming. This is the reason that the relaxation modes and

visco-elastic layers have been limited to two and the grid size has not been further refined – thus enabling the problem to be solved on a PC with a reasonable degree of accuracy.

This type of analysis allows the effects of both variations in wheel load contact stresses across the wheel and temperature depth gradients in the pavement to be modeled thus meeting the objectives discussed above. The major limitation of this analysis is that no provision is currently made for the consideration of the crack propagation once initiation has occurred. However, it could be argued that the major design consideration is the prevention of crack initiation.

6.4 Pavement Modeling

The pavement structure is considered as comprising two visco-elastic layers with variable temperature depth and hence, stiffness properties. One of these layers is used to model the HMA surface layer while the binder course and base layers are combined in the remaining visco-elastic layers. The foundation property sets are considered as elastic layers with information obtained through the analysis of the FWD data. The material property sets combined with the visco-elastic and elastic models define the structure being analyzed.

The first part of the analysis conducted was a check calculation to ensure that viscous-elastic response of the material model was reasonable. This was performed by the consideration of a pulse load test that had a similar range of loading speed to the pavement with the materials being considered. A Poisson's ratio of 0.3 was used in the analysis because it gave more realistic results compared to the Poisson's ratio of 0.4.

The displacements obtained for Site 1 are illustrated in Figure 53. The maximum deflection that occurs in this with the loading is 129 microns. The current FE code shows some permanent strain at the end of the pulse. This aspect requires some further investigation since the recovery should be greater (i.e. virtually complete) given Hirsch "solid" VE material model used in the analysis. In addition, the effects of boundary

symmetries are rather noticeable. The initial and final deflections are effectively due to a doubling of the load at the boundary of the pavement problem.

The change from a uniformly distributed load used in previous analysis to a detail stress pattern (variable contact stress and shear stress) going in towards and coming out of the central region of the finite element mesh causes some noticeable discontinuity in deflections. Further refinement is needed to correct this problem.

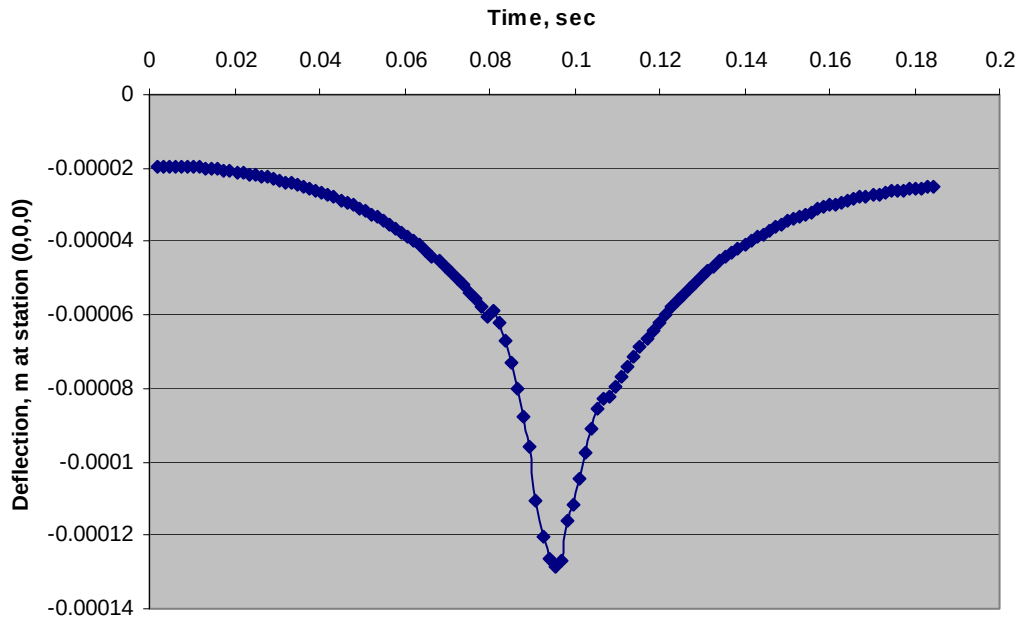

Figure 53: Displacements for site 1 using existing FE Code

6.5 Elastic Layered Analysis System

An existing computer program – LeapsPro™ (Layered Elastic Analysis of Pavement Structures) was used for the elastic layered analysis. LeapsPro™ makes use of a core layered elastic program which interacts with a number of routines to develop a pavement problem for analysis. However, for this application a special version of the LEAP software was produced that could handle a complex wheel load. This consisted of separation of the

wheel into 192 contact patches as illustrated in Figure 54. The magnitude of vertical load on each circular loading element is illustrated in Figure 55. The total magnitude of the loaded area was consistent with the loading required to produce a 40 kN wheel load (approximately 18 kip axle load).

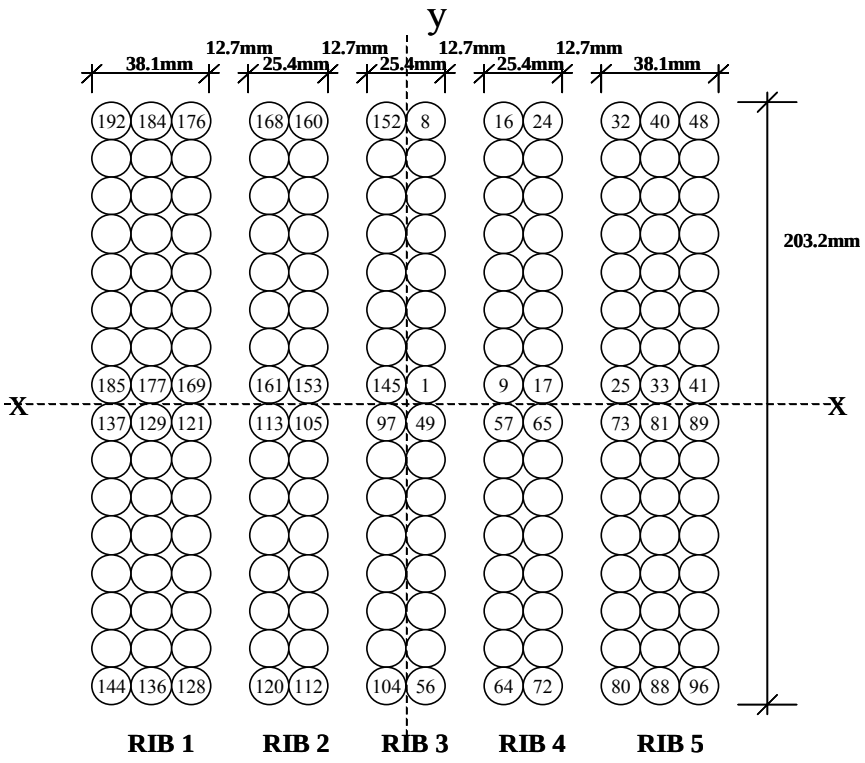

Figure 54: Representation of wheel load in elastic layer analysis

Pavement Layers

The pavement layers in LEAPS consist of asphalt layers of an elastic soil foundation. The asphalt pavement layers were subdivided into a wearing course and base layer. These layers were again sub-divided into two layers – with each sub layer being assigned its own temperature and modulus in the same manner as used for the finite element analysis.

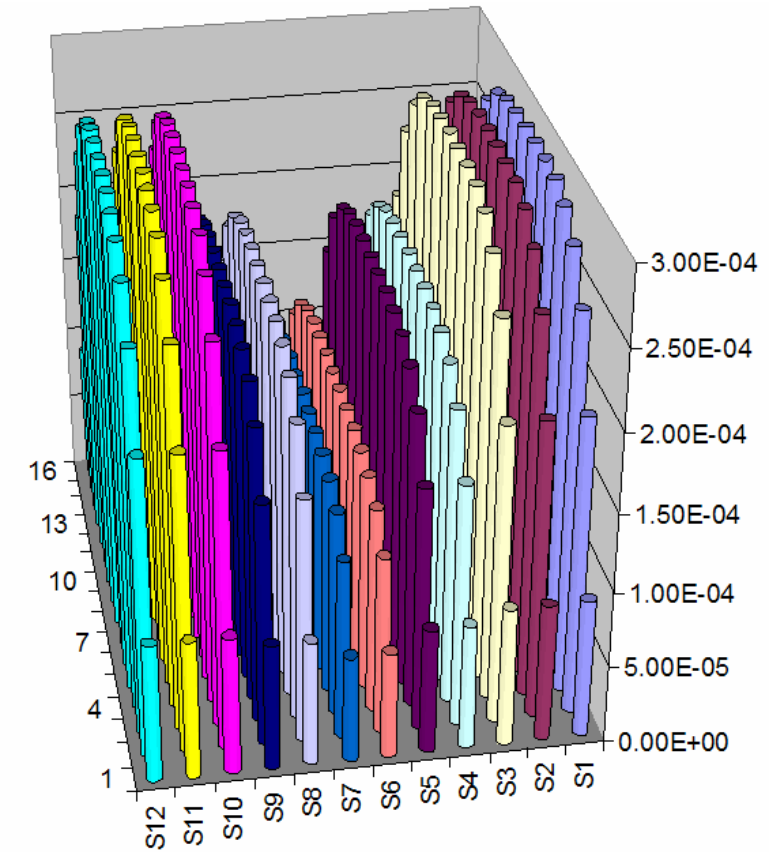

Figure 55: Relative magnitude of loads on each contact patch, MN

Loading Time

A loading time consistent with 80 km/h (approximately 50 mph) was used for the analysis. The loading time was not varied with depth but this could be added in subsequent analysis if considered necessary.

Asphalt Material Properties

Measured material properties were used to define a complete master curve. The Hirsch model was then used to develop the mixture stiffness for each temperature considered.

Computations

Computations where then produced for each site producing for 50 points that represent a transverse slice of the pavement – with 25 points computed for the surface properties and 25 for the base over a distance of 250 mm from the center of the loaded area. The radius of the loaded area is approximately 115 mm. From this analysis, many data representations can be made. Tensile strain, compressive strain all vary across the section and these have been combined into a single parameter – the octahedral shear strain as a relative measure of the damage likely to occur at any one point. The octahedral shear strain is computed from the results of the elastic analysis as follows:

$$\gamma_{oct} = \frac{2}{3}\left[\left(\varepsilon_x - \varepsilon_y\right)^2 + \left(\varepsilon_y - \varepsilon_z\right)^2 + \left(\varepsilon_z - \varepsilon_x\right)^2 + 6\left(\gamma_{xy}^2 + \gamma_{xz}^2 + \gamma_{yz}^2\right)\right]^{0.5} \quad \textbf{(22)}$$

The computed data in this format is presented in Figure 56 to Figure 61.

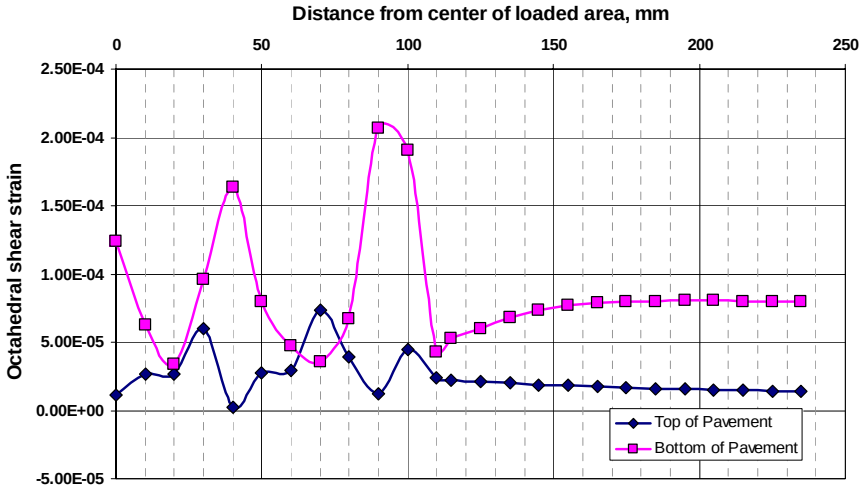

Figure 56: Variation of octahedral shear strain across transverse profile of pavement (wheel radius = 115mm), Site 1, cold extreme.

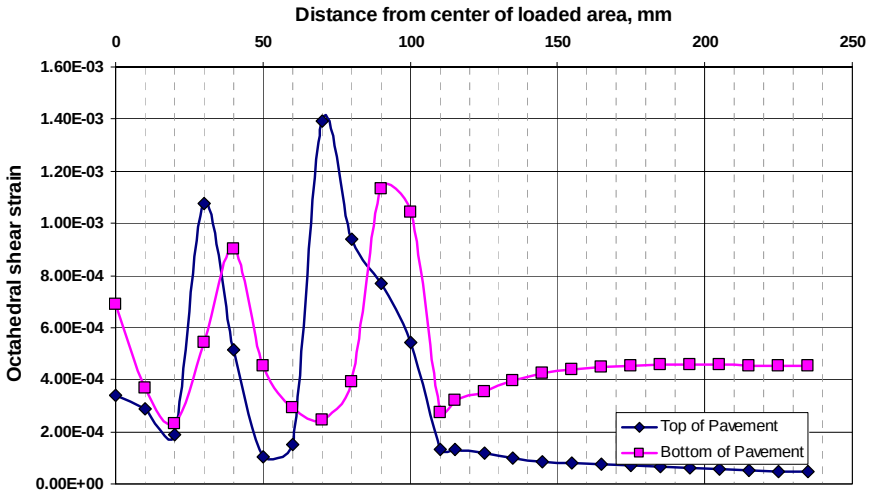

Figure 57: Variation of octahedral shear strain across transverse profile of pavement (wheel radius = 115mm), Site 1, hot extreme.

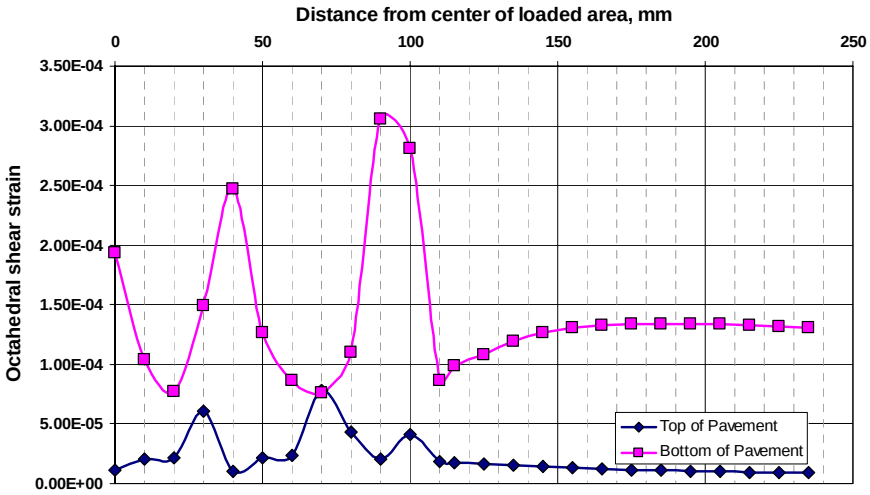

Figure 58: Variation of octahedral shear strain across transverse profile of pavement (wheel radius = 115mm), Site 2, cold extreme.

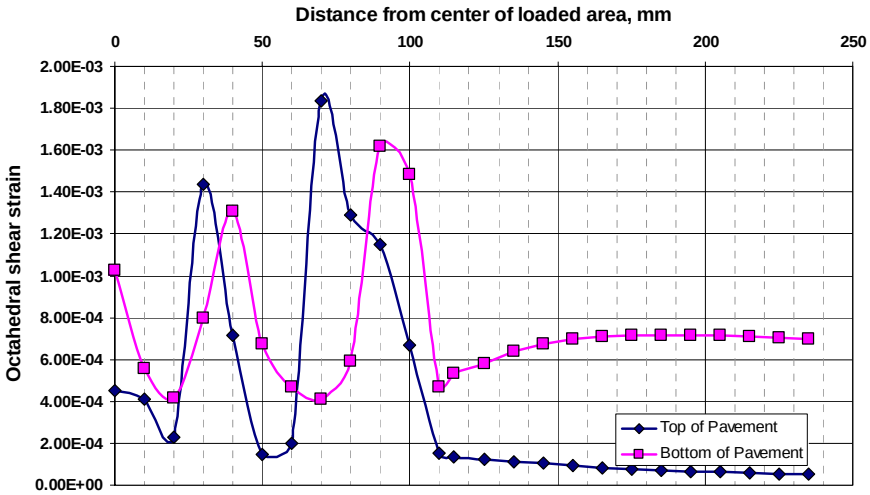

Figure 59: Variation of octahedral shear strain across transverse profile of pavement (wheel radius = 115mm), Site 2, hot extreme.

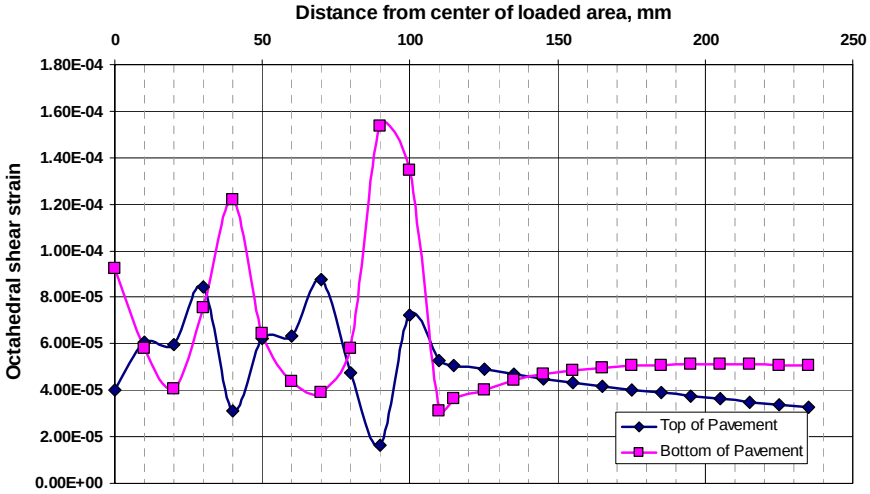

Figure 60: Variation of octahedral shear strain across transverse profile of pavement (wheel radius = 115mm), Site 3, cold extreme.

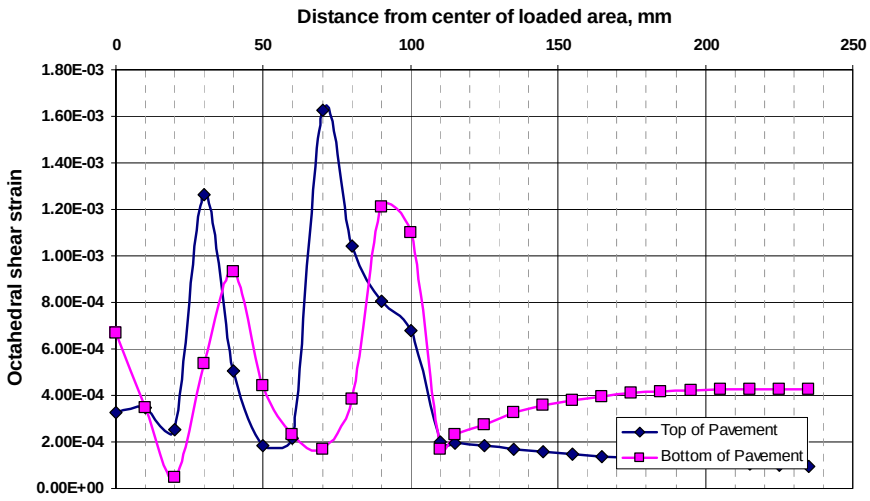

Figure 61: Variation of octahedral shear strain across transverse profile of pavement (wheel radius = 115mm), Site 3, hot extreme.

6.6 Pavement Analysis Summary

A considerable challenge exists in modeling a pavement structure with vertical and shear components of loading that are then subsequently represented as variable values over a loaded area. Modifications have been made to two types of analysis systems to enable the complex load effects to be studied, viz. finite element and layered elastic analysis programs.

6.6.1 Finite Element

Issues concerning the accurate modeling of a visco-elastic material in the finite element system need resolving but considerable progress has been made. This software needs additional work to complete the definition of input and output data. However, we can note the following:

- A larger number of relaxation times are needed to enable the load pulse to be accurately modeled. This number is most likely between 5 and 10.

- The effects of boundary conditions were noticeable on the analysis.
- The Poisson's ratio value made a significant impact on the results. This suggests that a method for varying the Poisson's ration with stiffness will be needed.

As this model is refined, better solutions will be made to obtain properties at the base and surface of the layers.

6.6.2 Elastic Layer Analysis

Analysis suggests that the winter cold condition has the largest magnitude of octahedral shear strain at the underside of the pavement whereas in the hot condition this is reversed with the largest magnitude on the surface. The variation in strain magnitude across the profile is quite surprising and it is suggested that additional calculations be performed to verify these findings. The relative magnitude of strains (expressed in micro strain units) is presented in Table 29.

Table 29: Magnitude of octohedral shear strains (με) for each site/condition.

SITE AND CONDITION	SITE 1: I-65 North		SITE 2: I-65 Loop		SITE 3: US-421 Madison	
	Cold	Hot	Cold	Hot	Cold	Hot
Top of pavement	73	1394	78	1837	87	1627
Bottom of pavement	207	1131	306	1618	154	1210

From inspection of this data it would be concluded that Site 2 is most susceptible to surface cracking followed by Site 3 and then Site 1. This is most likely because of the stiffer bases in the Site 1 and 3 locations. The absolute magnitude of the strains that are occurring in the hottest time of the year are very large compared to those used for typical pavement calculations using average annual air temperatures or some weighting of that parameter. This is due to the extreme conditions used in these calculations. These strains are considered more realistic of that occurring in the asphalt mix as a whole. The strain in

the binder will be considerably larger in magnitude. Consequently, an important aspect of the performance of the asphalt binder will be to sustain large strains with little or no damage – and if damage does occur then the ability to heal.

The highest strains are occurring on the inside edge of the outer rib. This is obviously very dependent upon the exact nature of stress used in the calculation. At best, we could note that this complex stress distribution is more realistic than a uniformly distributed load. Much further work is required which is beyond the limited scope of this study to truly define the stress/strains that occur on the pavement surface due to loading. However, we can state with confidence that the propensity for a pavement to crack due to high magnitude of strains occurring near the loaded wheel area and/or immediately adjacent to the wheel is established.

It would appear, if we accept that the octahedral shear strain is a good descriptive parameter for damage, that the initiation of cracking is most likely to occur in the hotter summer months. The extent of propagation of cracks once they have occurred is beyond the scope of this work – although it is postulated that these may well propagate better under cold climate conditions when the material is more brittle.

7 SUMMARY, CONCLUSIONS AND RECOMMENDATIONS

The objective of the study was to evaluate top-down cracked pavements and assess their structural capacity as well as study in-place materials to propose the best identification of distress type, material selection, and rehabilitation methods to be used in Indiana.

Research involved evaluating three surface cracked pavements during 2002 and 2003. A 500 m section of I-65 North of Lafayette was chosen as the first site (designated as Site 1), an I-65 section in downtown Indianapolis was the second site (Site 2), and US-421 in Madison was the third site (Site 3). Site 1 had 11 year old pavement, Site 2 had 12 year old pavement and Site 3 had 4.5 year old pavement. All these sites exhibited longitudinal wheel path cracking which was later identified as top-down cracking.

The research was carried out by conducting visual surveys, Falling Weight Deflectometer (FWD) testing, and coring from the cracked and non cracked pavement areas. Cores were first inspected and then subjected to a full laboratory-testing program to measure rheology and fracture properties of the binders used in the surface mixtures. Then, the measured material properties were utilized in a LE analysis program to investigate stresses and strains in the top and bottom of the pavement surface.

The following sections give a brief summary of visual survey and laboratory testing. Sections also present major conclusions based on the research findings. The two last sections discuss research recommendations and lay out an implementation plan.

7.1 Summary of Laboratory and Field Test Results and Conclusions

Pavement Performance

Visual inspection and results from the INDOT PMS measurement database indicate that all sites had longitudinal wheel path cracking. The measured rut depth was less than 4.5 mm for all of the sites. The PCR (Pavement Condition Rating) was 93.3, 99.8, and 99, for Sites 1, 2, and 3, respectively. Pavement performance is summarized in Table 30, which

shows the measured rut depths, smoothness, and distress rating values, as a reference. Based on these ratings, Site 1 had the most distresses, although it was one year younger than Site 2.

Table 30. Summary of Material Properties and Pavement Performance.

PROPERTY	SITE 1 I-65 North	SITE 2 I-65 Loop	SITE 3 US-421 Madison	AVERAGE
Pavement age (years)	11	12	4.5	7.8
Original Binder Grade	AC-20*	PG 64-22	PG 70-22	-
Rut depth (mm)	4.2	1.9	4.1	3.4
IRI (in/mile)	74	115	54	81
PCR	93.3	99.8	99.0	97.4
Fatigue cracking (m^2)	36.8	27.5	2.2	22.1
Longitudinal cracking (m)	126	102.5	83	103.8
Penetration (1/100 mm)	10.7	19.0	10.7	13.5
$T_{R\&B}$ (°C)	65.0	62.8	65.0	64.3
P_b (%)	5.4	5.9	6.3	5.9
Air Voids (%), WP/CL	6.6 / 8.1	7.8 / 7.4	9.8 / 10.1	8.1 / 8.5

*) Before Superpave binder grading INDOT was using AC-20 binder which most likely is close to PG64-22

Measured Crack Depth and Verification of Top-down Cracking

The cores obtained from cracked areas were examined visually and also using x-ray tomography. The x-ray tomography testing was completed at Turner Fairbank Highway Research Center by the Federal Highway Administration. The visual inspection and x-ray tomography suggested that the cracks were confined in the thin surface mix and did not penetrate deeper into the pavement in any of the sites. The depth of the surface cracks were from 15 to 22 mm and the crack orientation was downward skewed for Site 1 and downward vertical for Sites 2 and 3. This confirms that the observed surface cracking is a top-down cracking.

Construction Issues

Based on the visual survey, none of the sites seem to exhibit load-end segregation. Load-end segregation manifests itself as a coarser and more open mat texture repeating about 25 to 30 meter intervals. However, this finding was not verified by laboratory testing.

Longitudinal surface cracking in Site 3 was systematically located in the left wheel path area with some symmetrical cracking in the right wheel path. This may indicate some longitudinal mix segregation caused by screed extensions in the paver. The width of the paving lane is approximately 3.5 meters, which means that screed extensions were used to cover the entire paving width with one paver pass. The screed extensions can cause segregation of the mix depending on the specifics of the screed used and segregation tendency of the mix.

For Site 2 the outside wheel path cracking may also be initiated by segregation caused by screed extensions and edges of tunnel similarly as described for Site 3 above. In this case the weak area of the pavement is 0.5 meters outside of the wheel path which is consistent with the wider paving lane width of 4 meters.

For Site 1 the centerline cracking may be caused by segregation by the auger gear box in the center of the paver screed. The gear box may cause segregation as the mix is transported from the tunnel to the augers. The wheel path cracking may also be initiated from the areas of segregated mix, although in this case it seems to be less likely.

Structural Capacity

The FWD testing indicated that all sites had excellent structural capacity and computed effective structural numbers SN_{eff} were 8.5, 10.2, and 6.1 for Sites 1, 2, and 3, respectively. The effective modulus of all pavement layers above the subgrade, $E_{p,}$ was 2,187 MPa for Site 1, 1,682 MPa for Site 2, and 2,274 MPa psi for Site 3. The estimated W_{18} traffic base on the AASHTO 1993 Pavement Design Guide was over 10^8 ESALs for all sites.

The thickness of the full depth asphalt pavement was 368 mm, 530 mm and 203 mm

for the sites 1, 2, and 3, respectively. Therefore, at least for Sites 1 and 2 the pavement thickness and structural capacity indicate "perpetual" pavement and, therefore, they will not exhibit bottom-up cracking. Site 3 in Madison is also structurally very strong due to the layer of rubblized concrete underneath the asphalt layers. To sum it up, it is not expected that bottom-up cracking will develop in these pavements.

Binder Properties

Binder testing was completed only for the binder extracted from the 1.5-2 mm thick surface mix. Research findings for the conventional binder testing, penetration and ring and ball softening point, indicated relatively hard binders in all sites. Site 2 had the softest of the three binders tested. Measured penetration values ranged from 10 to 19, which fall out the lowest penetration grading of Pen 40/50. The original binder grade for Site 3 was PG 70-22, Site 3 had PG 64-22 binder, and Site 1 had AC-20 binder (comparable to PG64-22 binder). Based on Dynamic Shear Rheometer (DSR) testing it was estimated that the high temperature performance grade for Site 1 binder was PG 82, for Site 2 PG 76, and for Site 3 PG 82. Thus, Site 1 had aged three PG grades while Site 2 and 3 had aged two PG grades. Therefore, Site 2 binder was aged least and Site 3 binder was relatively aged the most.

Rheological testing agreed with the findings of conventional testing indicating that the Site 2 had softest binder when measuring with DSR. However, the relaxation modulus obtained from the combined DSR and Direct Tension Test (DTT) master-curve indicated that Site 3 had the most fast relaxing binder, which is consistent with the age of the sites. The DTT thus suggested that Site 3 had the most plastic and Site 2 the most brittle binder in the -22°C temperature. This implies that the surface cracking is not related to the low temperature cracking phenomenon in the asphalt mixtures.

Binder properties are summarized in Table 30. Compared to binder properties found from the literature, the binder stiffness data does not seem to differ significantly from the "normally" aged binder stiffness values.

Mixture Properties

The mixture properties were also measured from the thin surface mix layer. Site 3 had the highest air void content average being 10.1%, while Site 1 and 2 had 8.1% and 7.4%, respectively. It can be speculated that the high air void content in Site 3 has accelerated the binder aging compared to the other sites, although it had the highest binder content of 6.3% while Site 1 and 2 had 5.4% and 5.9% binder, respectively.

All mixtures were fine 9.5 mm surface mixtures and the amount of fines passing 0.075 mm sieve were 2.5 to 2.9% for Sites 1 and 3, while Site 2 had 5.8%. The studied mixtures had effective binder volume between 8 to 10%, and voids filled with asphalt ranging from 50 to 55%. Literature suggests that a better mix cracking performance may be obtained by increasing mix density by compaction. In addition, mixtures with more fines may be more crack resistant than mixtures with low amount of fines.

The measured SST shear modulus of the mixtures did not agree with the measured binder properties. Site 2 had the stiffest mix although it had the softest binder. This test result could not be verified because the IDT Creep compliance test data was erroneous and could not be used in the analysis. However, the slightly lower rutting of Site 2 mixture under traffic may indicate stiffer mixture compared to Site 1. However, the SST measurement is only based on one replicate test result and two cores had to be glued together to get a thick enough specimen for testing. The IDT strength test data indicated that Site 1 had the highest tensile strength at all test temperatures (-20, -10 and 0°C) while at 0°C temperature Site 2 had the lowest tensile strength. Mix Properties are summarized in Table 30.

7.2 Summary of Advanced Analysis and Conclusions

7.2.1 Pavement Modeling

Pavement modeling was completed using a 3-D Finite Element code to compute stresses and strains in the pavement due to the wheel loads. Due to the problems in the accurate modeling of a visco-elastic material, the analysis was not successful but considerable progress has been made. However, the software needs additional work to complete the definition of input and output data.

An additional layered elastic analysis of the sites indicated that the octahedral shear strain in the top and bottom of the pavement could explain the top-down cracking potential of the pavements. However, due to the problems of obtaining reliable measured mixture stiffness values, predicted values were used. This may introduce some error in the analysis. Analysis indicated that Site 2 (with lowest predicted mixture modulus) had the highest octahedral shear strain values compared to the other sites. This may indicate higher top-down cracking potential if the cracking phenomenon is shear strain driven at high temperatures. However, this is not clear based on the analysis.

7.2.2 Surface Crack Propagation

The crack propagation in all sites was confined to the surface layers. If the propagation rate would stay the same, the predicted crack propagation as percent of crack depth would be as shown in Table 31.

Table 31: Crack depth % of layer thickness.

SITE	PAV. THICKNESS (mm)	CRACK DEPTH (mm)	CRACK DEPTH % of THICKNESS	PAVEMENT AGE (years)	CRACK DEPTH% PER YEAR
1	368	20	5.4	11	0.5
2	530	22	4.2	12	0.3
3	203	15	7.4	4.5	1.6

Figure 62 compares measured INDOT crack depth values to the crack depths reported by Svasdisant et al. (2001). They measured surface crack depths and pavement layer thicknesses from seven different pavement sections. Pavements were about 10 years old and some of them had rubblized base. Figure 62 suggests that when the thickness of the pavement is above 200 mm the top-down cracks are not likely to propagate through the entire pavement structure.

It was inferred from Svasdisant et al. report that from the measured 41 cores 74% of the surface mixtures had cracked through, while only 36% of intermediate and 20% of base mixtures had cracked through the entire lift thickness.

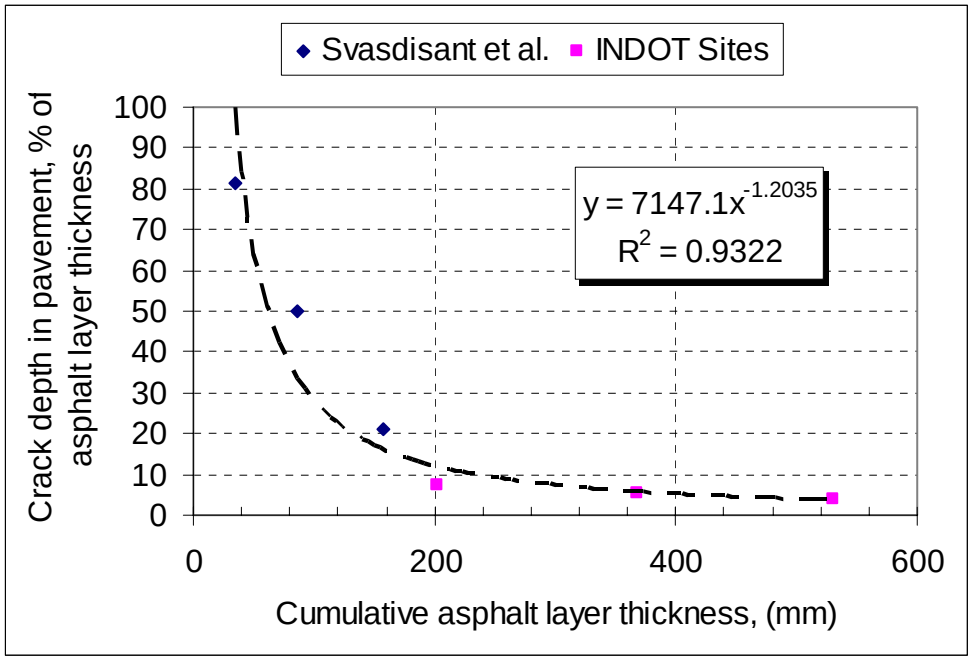

Figure 62: Measured crack depth as function of asphalt layer thickness.

7.2.3 Ranking of Sites

Table 32 shows the ranking of sites based on the measured binder and mix in-situ properties and the LE analysis. Ranking is done by arranging sites in order of most desired

condition for each parameter/criteria considered. Assigned value of one indicates best performance. It is also assumed that the softer binder is better than a stiffer binder for top-down cracking.

Table 32: Ranking of Sties

SITE	Mix Air Voids	Mix Fines	Critical Cracking Temp.	DST&DTT $\|G^*\|_{binder}$	E(t)	SST $\|G^*\|_{mix}$	IDT Strength	FWD	LE Anal.
1	2	3	3	3	3	1	1	2	1
2	1	1	2	1	2	3	2	1	3
3	3	3	1	3	1	1	3	3	1
				1 softest		1 softest	1 highest		

Based on this ranking, none of the sites seem to have properties far better than the others. The binder in Site 2 is softest but does not have good low temperature cracking properties. Hard binder in Site 3 has aged significantly compared to the other sites. The air void content in the mixtures seems to point in the direction that the binder aging is accelerated when the air void content exceeds 7.5%. The higher amount of fines in the mix may prevent binder and mix aging as Site 2 properties suggest.

7.3 Recommendations

7.3.1 Prevention of Top-down Cracking

The energy approach based on Linear Elastic Fracture Mechanics (LEFM) states that "crack extension (i.e., fracture) occurs when the energy available for crack growth is sufficient to overcome the resistance of material. The material resistance may include the surface energy, plastic work, or other type of energy dissipation associated with a propagating crack" (Anderson, 1995). The energy release rate *G* is defined as the rate of change in potential energy with crack area for a linear elastic material. At the moment of

fracture $G = G_c$ where G_c is the critical energy release rate which is a measure of fracture toughness. Hence, we can assume that pavement surface cracks are formed when the available energy provided by the tire loading cannot be absorbed by stain energy in the form of elastic bending or energy cannot dissipate in the form of plastic deformation of the structure. At fracture, energy is dissipated through creating fracture surfaces, in addition to energy dissipation through viscous and plastic flow.

This study was able to identify some material properties that most likely contribute to the fracture toughness and crack advancement in pavements; however, unfortunately this research was not able to distinguish structural reasons for top-down cracking. Literature review did not provide any conclusive evidence either. It can be speculated that there are several structural contributors to the pavement cracking such as mixture segregation, poor bonding between layers, thin layer thicknesses, and stiffness differentials between pavement layers.

It is obvious that the crack will find its way through the path of least resistance, so any weak area is vulnerable to crack initiation and propagation. The amount of energy tire loading introduces to the pavements today cannot be controlled by the pavement engineers (at least in a short term). Thus, the only thing that can be controlled in day to day operations is the material selection. Combining this with the use of current and new pavement design tools would be the most effective strategy to prevent pavement distresses. That is to say, as long as the models used in the pavement design methods are realistic and provide proper guidance. The best results will be achieved when all the above is combined with the enhanced construction practices. However, because most likely opposite measures are needed to prevent top-down and bottom-up cracking compared to the pavement rutting, a delicate balance is required while executing material selection for the pavement and mix designs.

The study recommendations can be divided into two categories 1) Material Selection and Construction practices, and 2) Structural Aspects. Due to the fact that only the first category items produced findings, recommendations for dealing with structural aspects are discussed in the implementation section.

The list below sums up the recommendations to prevent top-down cracking in terms of material selection, material properties and construction practices:

- Reduce in-situ air voids content below or equal to 7% by requiring tighter density specification
- Limit the amount of fines in the mixture to 5 to 6%
- No changes for binder grades is recommended at this point
- Prevent non-uniformities in the material properties by enhancing construction practices and QC/QA work including prevention of segregation during paving

The relatively high air void content of the studied asphalt mixtures, around 7 to 9%, allowed a certain degree of aging in all sites to occur. These air void contents are not untypical of U.S. practice but better values can be achieved. It would be desirable to ensure that in well constructed pavements the as-built air void content would be in the range 5 - 6% - allowing for some densification over time. To guard against permanent deformation due to the secondary traffic densification, a stiffness requirement must be set for pavements having air void contents less than 4%. This recommendation requires modifications to the construction specifications.

The requirement of more fines in the mixtures is based on the theory that mixture tensile strength (related to fracture toughness) will increase as more fines are used. However, mixture stiffness will also increase, which will make it more difficult to compact. The shape of fines, i.e. round or crushed, affects the mixture's compactability considerably. Therefore, there is a need to study compatibility of mixtures as a function of fines and the type of fines used.

The selection of binder grade and surface mix properties for preventing top-down cracking is quite controversial. However, it can be speculated that binders with low relaxation capacity are vulnerable for cracking. The balance between rutting and cracking is delicate, as mentioned earlier, and without further research this study cannot recommend to reduce binder stiffness used.

Segregation creates weak spots in the pavements allowing crack initiation to occur. None of the sites had load-end segregation based on visual inspection. But crack patterns, especially at US-421 in Madison, indicate that lane segregation caused by construction practices might exist.

7.3.2 Rehabilitation of Top-down Cracked Pavements

Based on this research the identification of top-down cracking from the bottom-up cracking can be based on the knowledge of the thickness of the pavement structure and the pattern of the cracking. The top-down cracking manifests itself as a longitudinal cracking in the wheel path area or in the center of the lane. If layer thickness is above 200 mm it is unlikely that cracks will penetrate deeper than through the surface layer in the pavement. Coring and examining cracks from a few locations in the pavement can be used to verify the top-down cracking.

FWD testing and a structural analysis must be performed to confirm that the cracking has not weakened the pavement structure. If the structural capacity is good, the pavement can be rehabilitated by milling and replacing the surface mix.

The selection of the rehabilitation material is dependent on the structural capacity of the pavement. In the material selection, the recommendations given to prevent top-down cracking above should be followed.

8 IMPLEMENTATION

The implementation of this research can be divided into the short, medium and long term goals. The short and medium term implementation issues are related to the INDOT's current construction practices and possible changes in them. The medium and long term implementation goals are related to the pavement design issues and therefore to the future research in the local and possibly in the national level (Federal Highway Administration

(FHWA) and National Cooperative Research Program (NHCRP)). The short and medium term local implementation issues include:

- Training of contractor and state personnel to enhance construction and QC/QA work (high priority)
- Development of top-down identification, prevention, and rehabilitation guide based on research findings (high priority)
- Modify current construction specifications to reduce segregation (high priority)
- Modify current pavement design practices (low priority)
- Research of tendency of asphalt mix to segregate (low priority)

A short description of items listed above is presented as follows. Training of personnel must be organized in cooperation with INDOT and Asphalt Pavement Association of Indiana. This way the issues hindering good quality can be identified and hopefully remedied. Issues that are needed to be included in the training are mixture compaction, lay down operations, and prevention of segregation.

A guide to identify top-down cracking and select rehabilitation strategy needs to address the following listed items. Not all of these items can be addressed with great detail and this guide must develop over time to incorporate any future research or empirical findings of pavement performance in Indiana.

- Identification of top-down cracking (visual survey and coring)
- Verification of pavement structural capacity using FWD
- Verification of bonding between layers with coring and with possible laboratory test
- Identification of segregation (visual survey, coring and laboratory measurements)
- Material Selection (stiffer or softer binder/mix compared to the replaced material and existing structure)
- Structural issues (surface layer thickness same as before or thicker?)

- Construction practices (the need for tack coat, type of tack coat, type of rollers such as steel wheel or vibratory)

To implement the needs to modify current construction specifications related to the in-situ density and amount of fines in the mixture, a research plan to establish the relationship between mix design and achievable in-situ mixture density must be developed. Some ideas how the research can be conducted are listed below:

- Use Superpave Gyratory Compactor (SGC) to establish a laboratory compaction curve for standard surface and base mixtures in Indiana. Select the standard mixture such that it represents typical aggregates and binder grade used.
- The compaction curve must be developed for different compaction temperatures by each temperature compacting mixture to the refusal density (zero percent air void content if possible).
- The laboratory gyratory compaction must be correlated to the field compaction by using field test strips. Densification using different roller types must be examined at various temperatures. This will establish equivalency of mix densification between field and laboratory compaction.
- As a part of the mix design process, require SGC compaction test for each designed mix to verify the mix compactability. If possible, use gyratory that can measure shear force during the compaction.
- Measure stiffness of the standard mixtures by SST Shear Frequency Sweep Test and axial dynamic modulus test and Indirect Tensile strength of the standard mixtures and correlate this to the JTRP SPR 2644 study findings.
- Correlate standard mixture material properties to pavement performance
- Modify standard mixtures by changing binder stiffness and/or the amount and type (round or crushed) of fines in the mix.
- To verify boundary conditions (i.e., simulation of real life pavement performance) possible Pur-Wheel tests can be performed.

Pavement structure, i.e., layer thicknesses, number of layers, and type of layers (rigid or flexible) all affect pavement performance, in addition to the type of materials used. Literature suggests that differential stiffness differences affect the stress distribution and thus crack formation in the pavements. In this study two sites had rubblized base underneath the flexible pavement. How this contributes to the top-down cracks was not studied. The combined stress distribution in the pavement structure is affected by the environment and type and magnitude of loading, as we know. What we do not know is what is the worst (or best) possible pavement structure to prevent particular pavement distress and how distresses interact with each other.

To implement changes to the current pavement design practices and verify items related to the structural aspects and construction practices in the developed rehabilitation guide a research plan to study shear stresses and friction between tire and pavement must be developed. Some ideas how the research can be conducted are listed below:

- Construct trial pavement in the INDOT APT pit to study the role of bonding between surface and base layer. The bonding is also related to the friction between the tire and the surface mixture. The high shear stresses that can be developed in the APT by applying high wheel loading without wander provide a means to conducting accelerated pavement surface failure experiments. Testing can be conducted in varying pavement temperatures to separate the cracking and rutting phenomenon. The things related to the bonding of surface layer, the use of tack coat, type of tack coat and compaction are some of the variables.
- In a similar manner, the APT pit can be used to study the role of surface layer thickness for the formation of surface cracks and rutting. Also, the effect of stiff layer (rubberlized concrete) underneath the asphalt layers can be studied.
- This type of research would allow investigation of the issue of using stiff or soft binder in the overlay to replace top-down cracked surface mix (stiffness differentials, layer thickness and rutting versus cracking).

As mentioned above cracks find their way through the least resistance and the coarse portion of segregated mixture typically have high air voids content, low binder content and low amount of fines compared to the job mix formula (Pellinen, 1985). All these properties contribute to the mixture's vulnerability to fracture.

Segregation may be caused by poor mixing or poor lay down of the mix and the degree of segregation is dependent on the mixture's tendency to segregate. The segregation tendency increases when mix has low amount of fines passing 0.075 mm, low binder content, and large aggregate top size (Pellinen, 1985).

The segregation tendency of the mixtures should be considered in the mix design. It would be desirable to develop a quick laboratory method to measure segregation tendency. In the 70's Swedish researchers Hillgren and Sjöblom (1979) developed a method to measure segregation tendency of asphalt mixtures in the field and in the laboratory. Unfortunately testing requires binder extraction and gradation testing of 11 kg of asphalt mix which makes it less practical for frequent use. The method is based on dropping asphalt mix through a funnel and measuring binder content and gradation of fine and coarse portion of segregated mixture.

The segregation caused by paving operations and paver can be prevented to some extent by first understanding when the mix is segregated and then adjusting paver to reduce the segregation. Mixture transfer vehicles have been successful in reducing the load-end segregation but "machine" segregation caused by the paver is still not well understood. Field studies have shown that a thermal camera is an effective way to reveal the segregated spots by measuring temperature differentials in the hot mix asphalt.

8 REFERENCES

AASHTO, "*Standard Test Method for Determining the Fracture Properties of Asphalt Binder in Direct Tension*," Designation TP3-00, Provisional Standards, 2000.

AASHTO, "*Specification for Performance Graded Asphalt Binder*," Provisional Standards MP1A, 2001a.

AASHTO, "*Practice for Determination of Low-Temperature Performance Grade*," Provisional Standards PP42, 2001b.

Abatech Inc. "*Rheology Analysis – RHEA Software*," Version 0.9.78, 2002

Baumgaertel, M and Winter, H.H., "*Determination of Discrete Relaxation and Retardation Time Spectra from Dynamic Mechanical Data*," Rheol Acta 28:511-519 1989.

Baumgaertel, M., & Winter, H.H., (1989). *Determination of Discrete Relaxation and Retardation Time Spectra from Dynamic Mechanical Data*. Rheological Acta, 511-519.

Brown, S.F. and Brunton, J.M., "*An Introduction into the Analytical Design of Bituminous Pavements*," 3rd Edition, University of Nottingham, Nottingham, England, 1985.

Gerritsen, A.H., van Gurp, C.A.P.M., van der Heide, J.P.J, Molenaar, A.A.A, and Pronk, A.C. *Prediction and Prevention of Surface Cracking in Asphaltic Pavements*, Proc. 6th International Conference on the Structural Design of Asphalt Pavements, Ann Arbor, 1987.

Christensen, D. W., & Anderson, D. *Interpretation of Dynamic Mechanical Test Data for Paving Grade Asphalt Cements.* Journal of Association of Asphalt Paving Technologists, Vol. 61, pp. 67-116, 1992.

Christensen, D. W., Pellinen, T., & Bonaquist, R. *Hirsch Model for Estimating Modulus of Asphalt Concrete.* Journal of Association of Asphalt Paving Technologists, Vol 72, 2003.

Gordon, V., and Shaw, M. *Computer Programs for Rheologists*, Hanser/Gardner Publications, 1994.

Finnish Pavement Tecnology Advisory Council (PANK). (1995). Finnish Asphalt Specifications 1995. Helsinki.

Hillgren, and Sjöblom, (1979). *Separationsbenägenhet Hos Asfaltmassor*. Svenska Bygnasentreprenörföreningen. Raport no. 23. Stockholm 1979, 30p.

Hugo, F and Kennedy, T.W., "*Surface Cracking of Asphalt Mixtures in Southern Africa*," Proceedings of the Association of Asphalt Paving Technologists, Volume 54. 1985.

Huang, Y. Pavement Analysis and Design. 2nd Ed. Prentice Hall, New Jersey, 2002.

Jacobs, M.M.J., "*Cracking in Asphalt Mixes*," PhD, The Delft University of Technology, The Netherlands, 1995.

Kunst, P.A.J.C., "*Surface Cracking in Asphalt Layers*," CROW Record 4, The Netherlands, 1990.

Matsuno, S., and T. Nishizawa. *Mechanism of Longitudinal Surface Cracking in Asphalt Pavement*, Proc. 7th International Conference on the Structural Design of Asphalt Pavements, Ann Arbor, 1992

Myers, L. A., "*Development and Propagation of Surface-Initiated Longitudinal* Wheel Path Cracks in Flexible Highway Pavements," PhD Thesis, University of Florida, 2000.

Myers, L. A., R. Roque, and B. E. Ruth. *Mechanisms of Surface-Initiated Longitudinal Wheel Path Cracks in High-Type Bituminous Pavements.* Journal of the Association of Asphalt Paving Technologists, Vol. 67 pp. 401-432, 1998

Niederquell, M. Baladi, G.G.Y, and Chatti, K. *Rubblization of Concrete Pavements: Field Investigation.* In Transportation Research Record, 1730, TRB, National Research Council, Washington, D.C., 2001, pp. 150-160

Owen, D.R.J. and Hinton, E., "*Finite Elements in Plasticity. Theory and Practice*," Pineridge Press, Swansea, 1980.

Owen, D.R.J., Prakash, A. and Zienkiewicz, O.C., "*Finite Element Analysis of Non-linear Composite Materials by use of Overlay Systems*," Computers and Structures, Vol. 4, 1974, pp. 1251 -1267.

Performance of Coarse Graded Mixes at WesTrack - Premature Rutting. Analysis Conducted by an Independent Team, Final Report, June 1998, FHWA, FHWA-RD-99-134. 1998.

Pellinen, T., Christensen, D.W., Rowe, G., Scharrok, M. *Fatigue Transfer Models- How do they Compare?* Paper presented in Transportation Research Board Annual Meeting, January 12-15, 2004.

Pellinen, T. (1985). *Asfalttimassan epähomogeenisuuden ja lajittumisen vaikutuksesta asfalttipäällysteeseen.* (On the Influence of Asphalt Mix Inhomogeneity and Segregation

on Asphalt Pavement). University of Oulu, Laboratory of Road and Traffic Technology, Publication No. 2, Oulu. 125 p (38 Figs., 42 Tbls., 32 Refs.)

Rowe, G.M., "*Application of the Dissipated Energy Concept to Fatigue Cracking in Asphalt Pavements*," PhD Thesis, University of Nottingham, January 1996.

Rowe, G.M., Sauber, R., Fee, F. and Soliman, N., "*Development of Lon-Life Overlays for Existing Pavement Infrastructure Projects with Surface Cracking in New Jersey*," Transportation Research Board/National Research Council, Transportation Research Circular, Number 503, December 2001, pp. 96-107.

Rowe G.M., and Sharrock, M.J., "*Development of Standard Techniques for the Calculation of Master Curves for Linear-Visco Elastic Materials*," The 1st International Symposium on Binder Rheology And Pavement Performance, The University of Calgary, Alberta, Canada, August 14 - 15, 2000.

Rowe, G.M., D'Angelo, J.A., Ho, S. and Sharrock, M.J., "*Development of the Direct Tension Test Analysis Procedures for Thermal Crack Prediction*" Proceedings of the forty-seventh annual conference of the Canadian Technical Asphalt Association, Calgary, Alberta, ISBN 0-921317-53-0, 2002, pp. 405-431.

Rowe, G., & Brown, S., Sharrock, M., Bouldin, M. *Visco-elastic analysis of Hot Mix Asphalt Pavement Structures.* Transportation Research Record. n1482, pp44-51, 1995.

Shell International Petroleum Company, "*Shell Pavement Design Manual*," London, 1978.

Schorsch, M., Chnag, C-M., Baladi, G.Y. *Effects of Segregation of the Initiation and Propagation of Top-Down Cracks.* Paper presented in Transportation Research Board Annual Meeting, January 12-16, 2003.

Stuart, K., Mogawer, W., Romero, P. *Validation of the Superpave Asphalt Binder Fatigue Cracking Parameter Using an Accelerated Loading Facility.* Publication No. FHWA-RD-01-093. Turner Fairbank Highway Research Centre, McLean, VA.

Svasdisant, T., Schorch, M., and Baladi, G.Y. *Mechanistic Analysis of Top-Down Cracks in Asphalt Pavements.* Paper presented in Transportation Research Board Annual Meeting, January 13-17, 2002.

Tsai, B.W., Harvey, J., Monismith,C. WesTrack *Fatigue Performance Prediction Using Miner's Law.* Proceeding of Transportation Research Board, 81th Annual Meeting, Washington, D.C., 2000.

Uhlmeyer, J.S., K. Willoughby, L. M. Pierce and J. P. Mahoney. *Top-Down Cracking in Washington State Asphalt Concrete Wearing Courses.* In Transportation Research Record 1730, TRB, National Research Council, Washington, D.C., 2000, pp. 110-116

Zienkiewicz, O.C., Nayak, G.C. and Owen, D.R.J., "*Composite and Overlay Models in Numerical Analysis of Elasto-plastic Continua*," International Symposium on Foundations of Plasticity, Warsaw, 1972.

Wambura, J. H. G., J. Maina and H. R. Smith. *Kenya Bituminous Materials Study*. In Transportation Research Record 1681, TRB, National Research Council, Washington, D.C., 1999, pp. 129-137

Williamson, R.H. *Environmental Effects in Road Pavements and their Engineering Significance*. PhD Thesis, University of Natal, Durban, Vol. 1, 1972

Williams, M.L., Landel, R.F. and Ferry, J.D., (1955) "*The Temperature Dependence of Relaxation Mechanisms in Amorphous Polymers and Other Glass-Forming Liquids*," Journal of the American Chemical Society, Volume 77, pp. 3701-3707.

APPENDIX A **DISTRESS DATA SHEETS**

Site 1: I-65 North of Lafayette

Location 1:

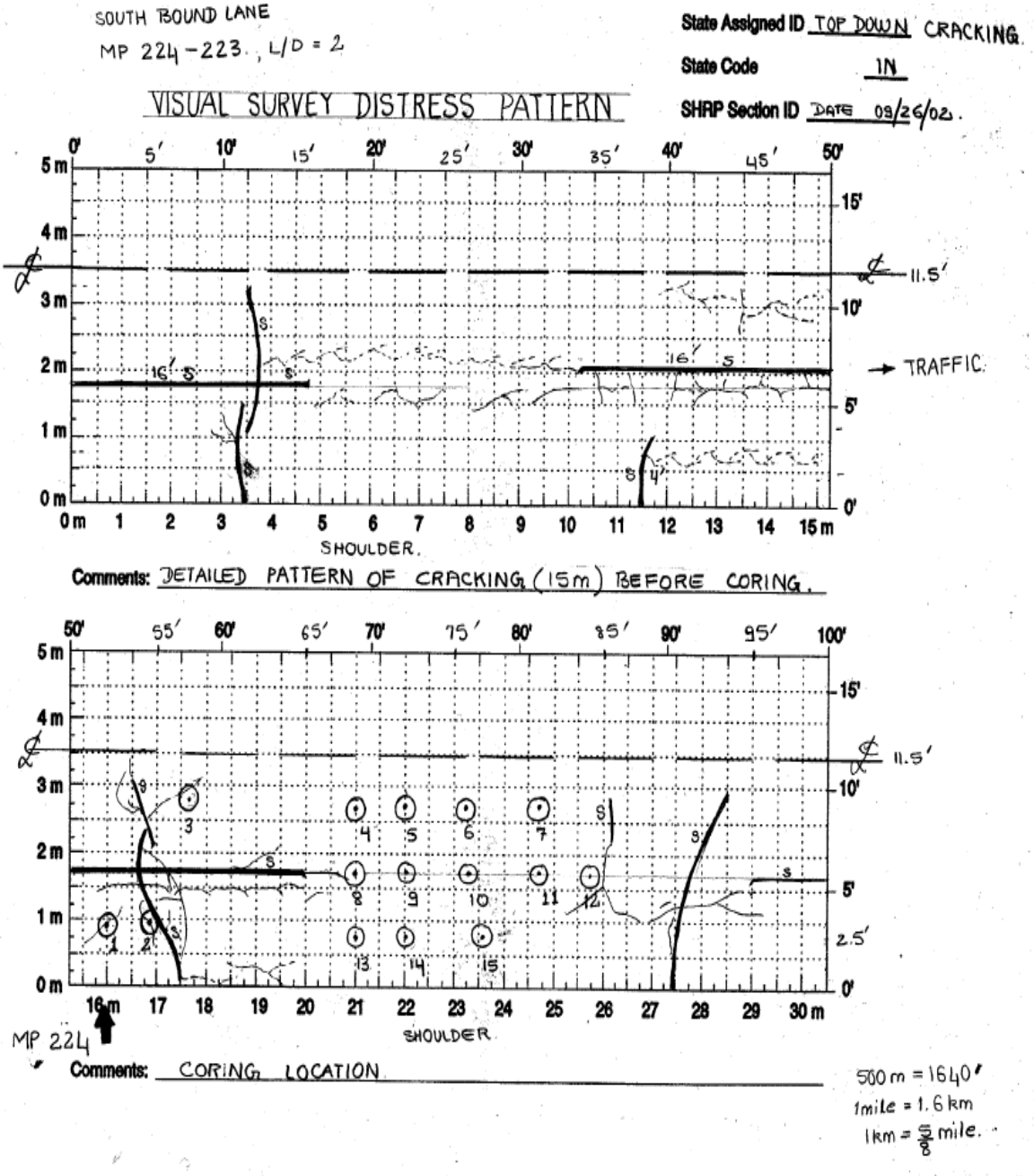

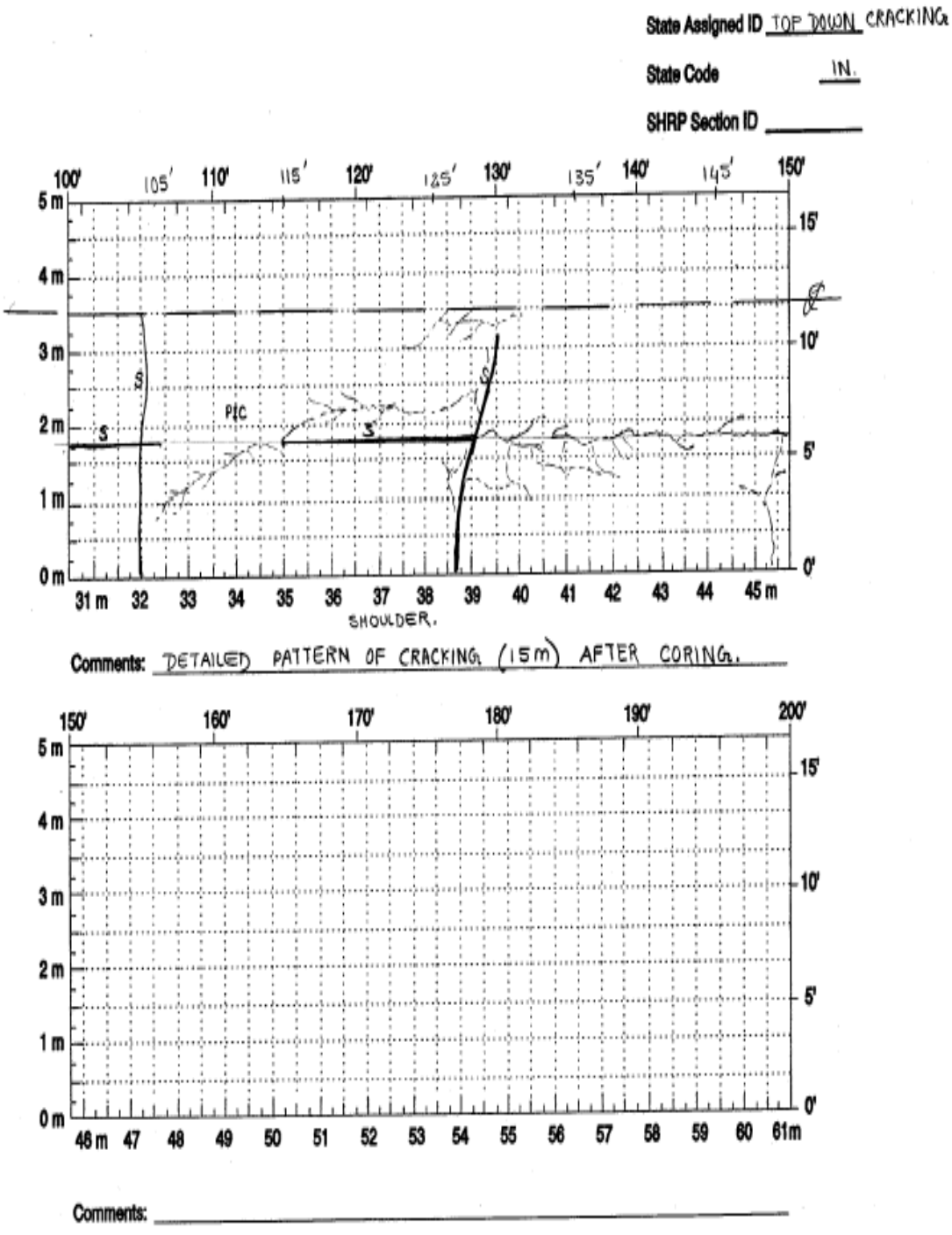

15 cores were obtained from location 1 of Site 1: I-65 North of Lafayette.

Location 2:

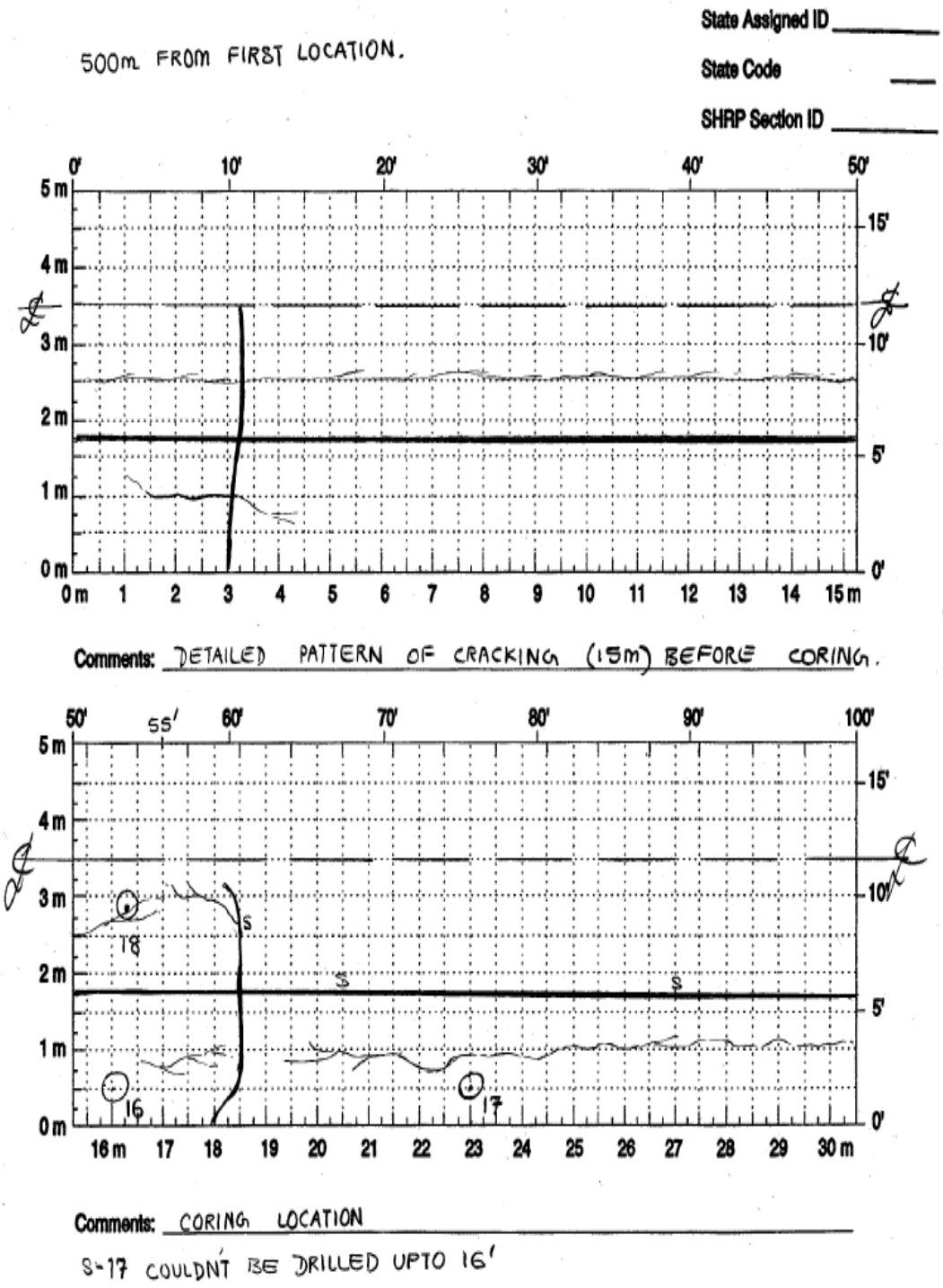
State Assigned ID
State Code
SHRP Section ID
500m FROM FIRST LOCATION.
0' 10' 20' 30' 40' 50'
5 m 4 m 3 m 2 m 1 m 0 m
15' 10' 5' 0'
0m 1 2 3 4 5 6 7 8 9 10 11 12 13 14 15 m
Comments: DETAILED PATTERN OF CRACKING (15m) BEFORE CORING.
50' 55' 60' 70' 80' 90' 100'
5 m 4 m 3 m 2 m 1 m 0 m
15' 10' 5' 0'
S
18
16
17
16 m 17 18 19 20 21 22 23 24 25 26 27 28 29 30 m
Comments: CORING LOCATION
S-17 COULDN'T BE DRILLED UPTO 16'

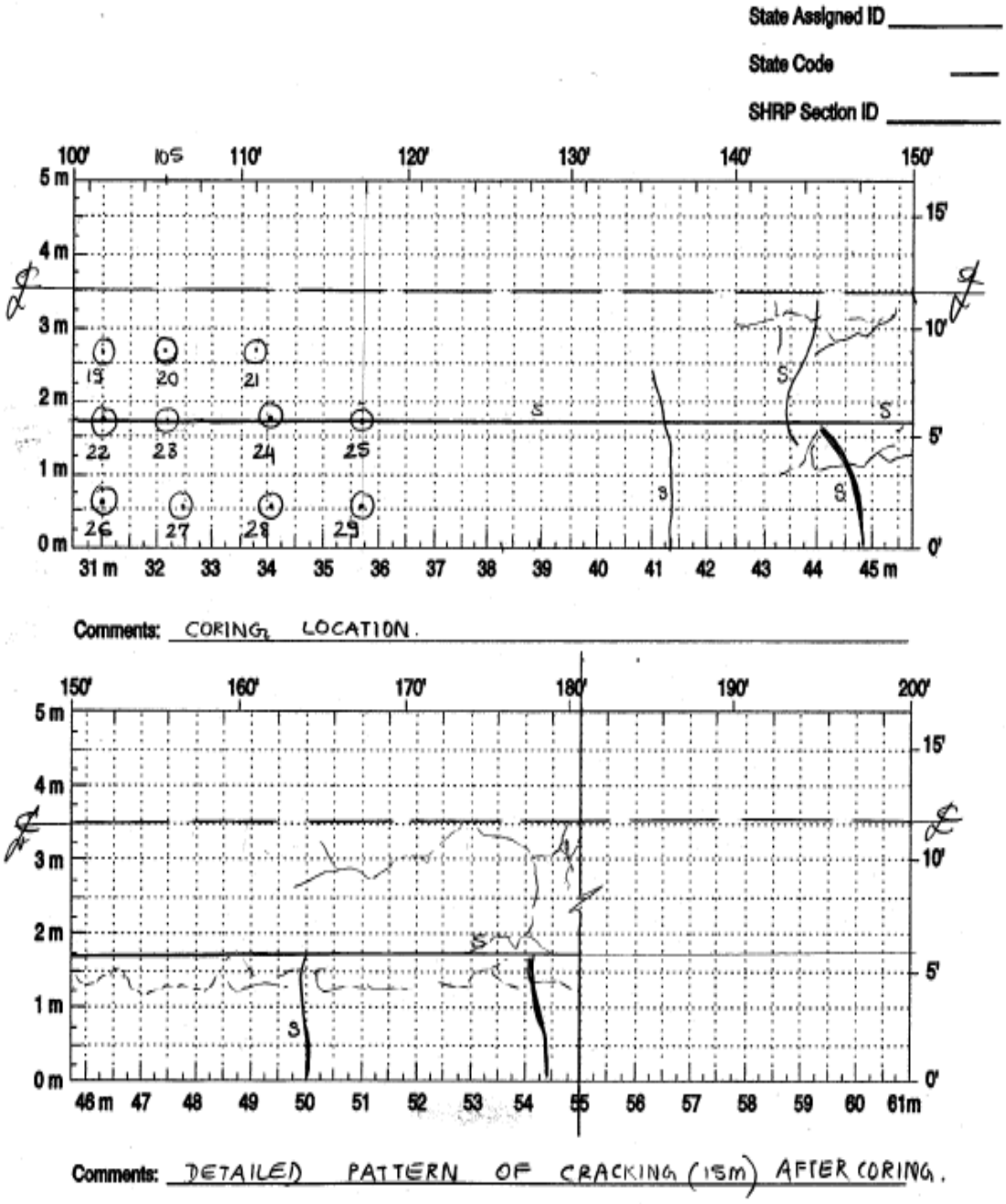

14 cores were obtained from location 2 of Site 1: I-65 North of Lafayette.

Site 2: I-65 Near Indianapolis

Location 1:

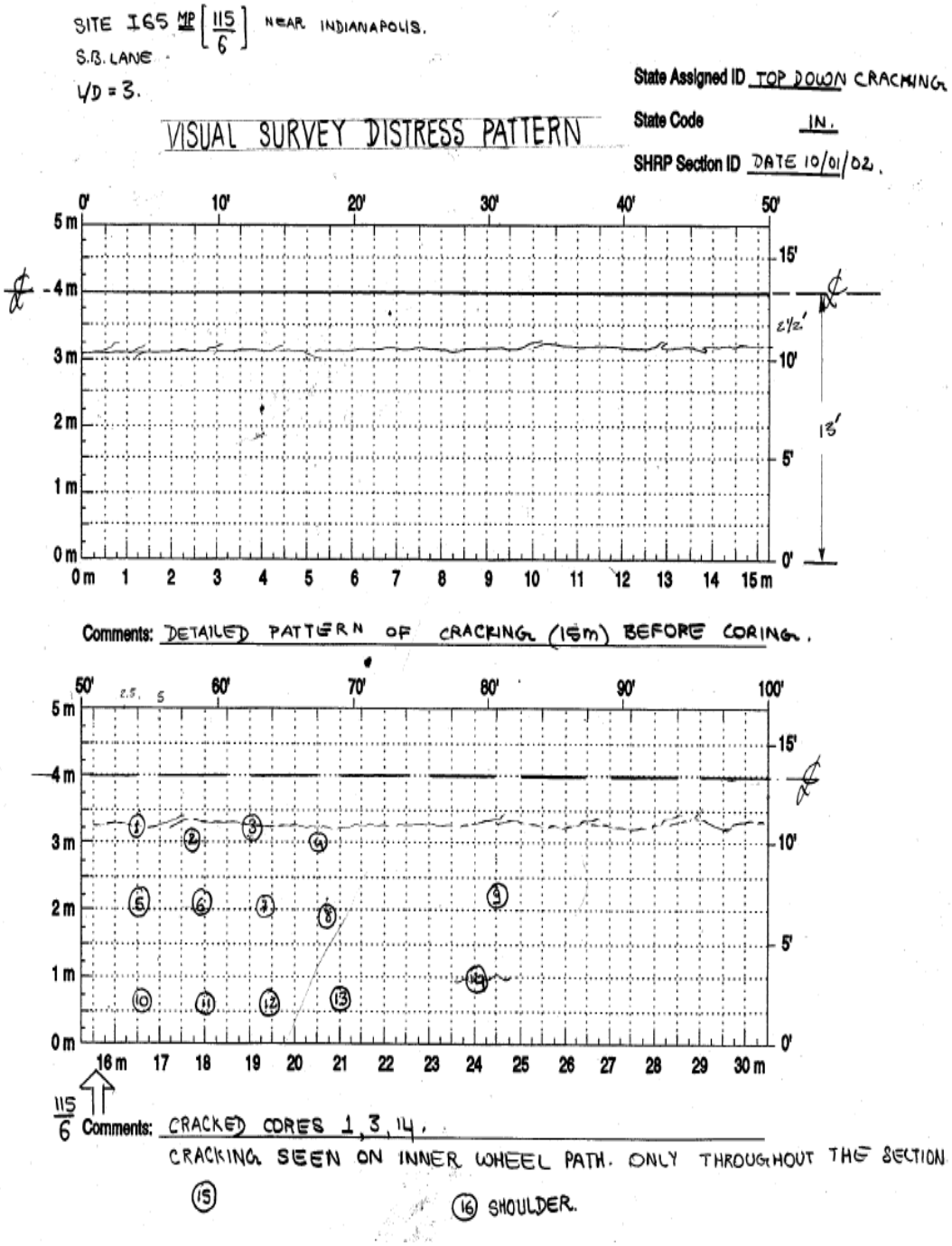

16 cores were obtained from location 1 of Site 2: I-65 Near Indianapolis.

Location 2:

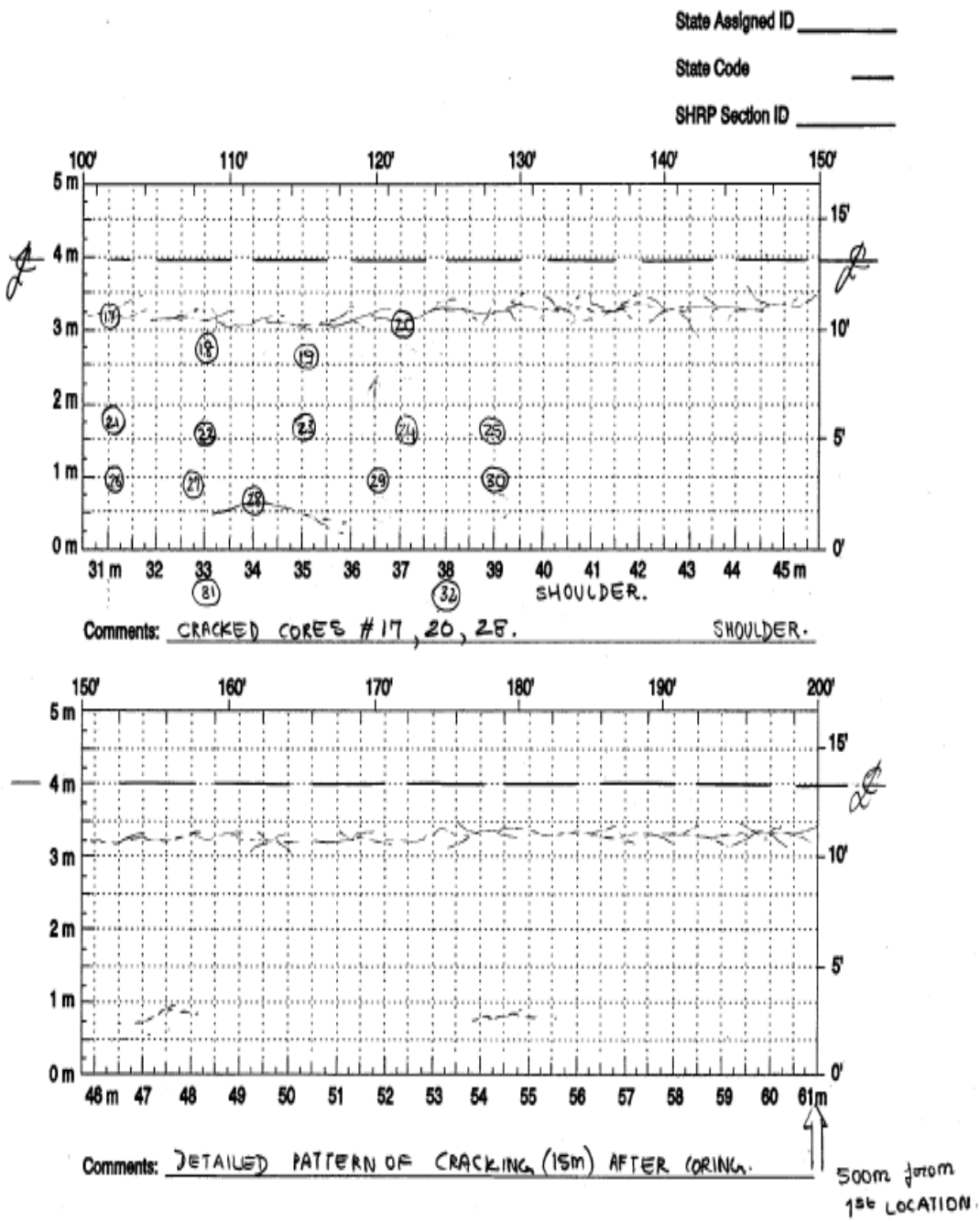

16 cores were obtained from location 2 of Site 2: I-65 Near Indianapolis.

Site 3: SR 421 Madison

Location 1:

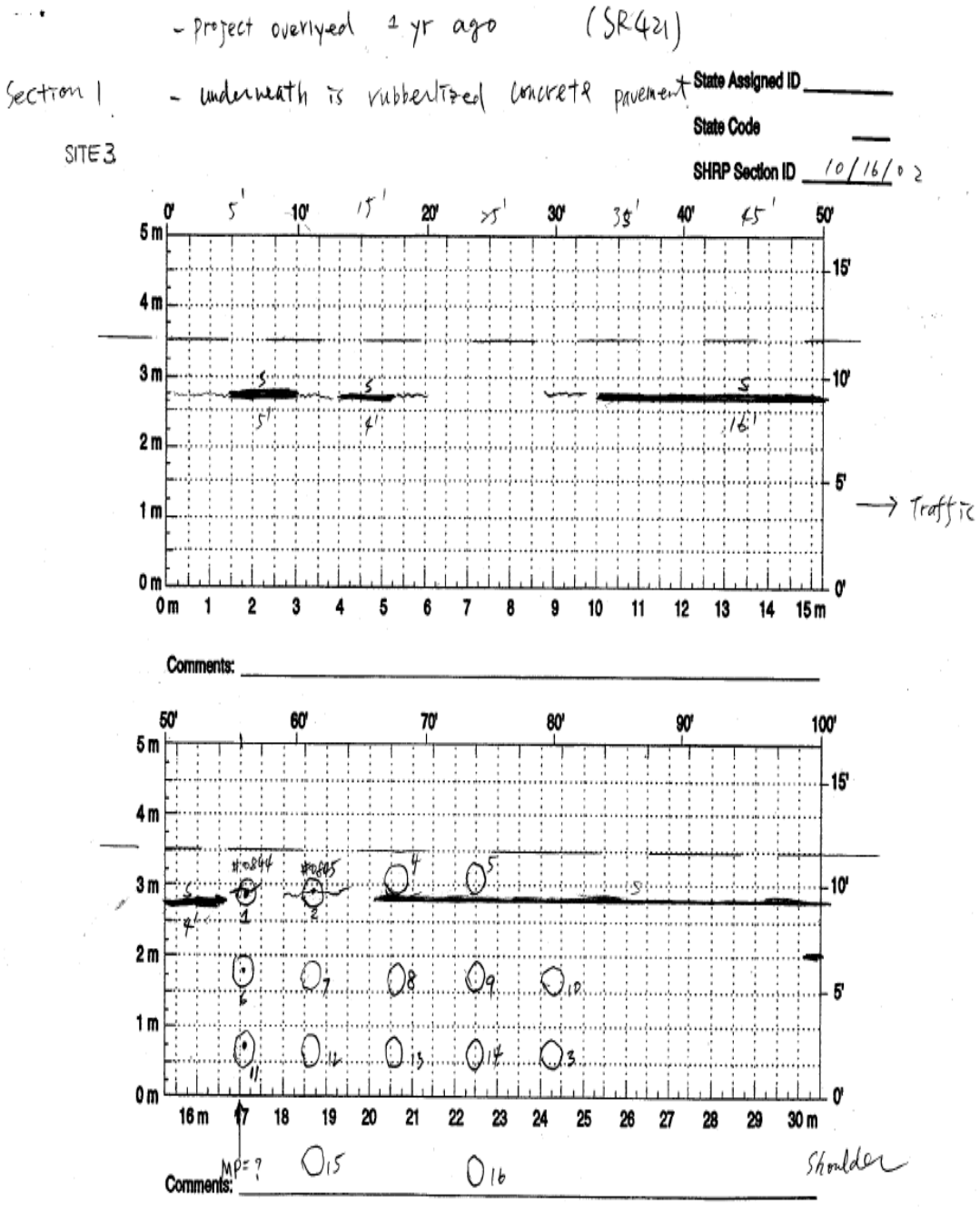

16 cores were obtained from location 1 of Site 3: US 421 Madison.

Location 2:

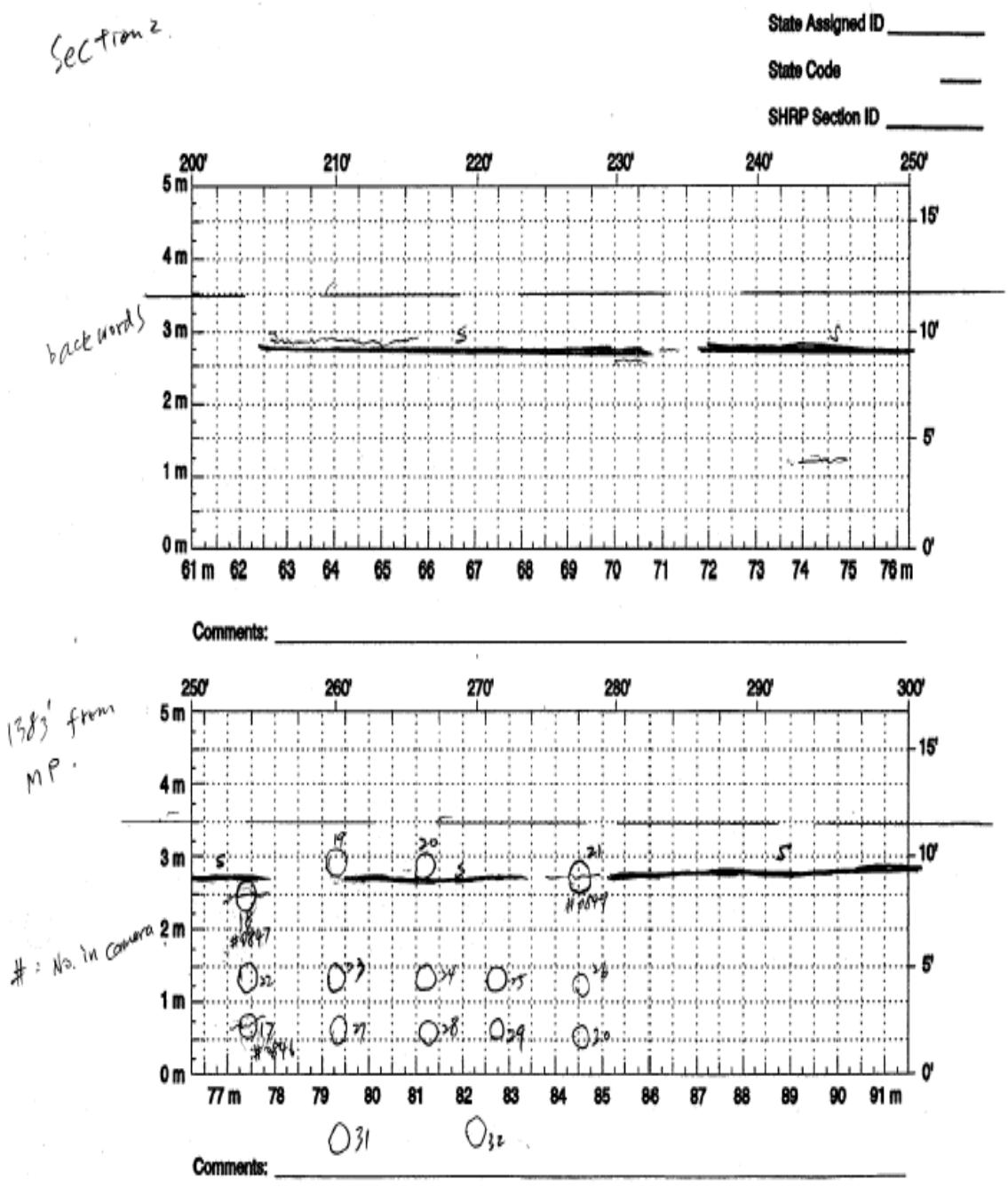

16 cores were obtained from location 2 of Site 3: US 421 Madison.

APPENDIX B **PAVEMENT MANAGEMENT SYSTEM -DISTESS RATINGS**

COMPOSITE OR FLEXIBLE DISTRESS RATING		
RATING	0=NONE 1=LOW	0=NONE 1=FEW
	2=MODERATE 3=HIGH	2=SEVERAL 3=MANY
DISTRESS	**SEVERITY**	**EXTENT**
1. RAVELING	1) Light Agg Loss 2) Moderate Agg Loss 3) Severe Agg Loss	1) Isolated Spots Or Strips 2) 12 25% To 75% Of Area 3) More Than 75% Of Area
2. PATCHING	1) Minor Distress, Rides Good 2) Fair Condition 3) Deteriorated Or Temp Patch	1) 1-3 Deteriorated Patches Per 100' 2) 4-6 Deteriorated Patches Per 100' 3) >6 Patches Per 100'
3. HOLES	1) Palm Sized Or Shallow (<1") 2) Dinner Plate/Moderate Depth 3) Larger Than #2	1) Isolated, Random Occurrence 2) Occur In 10% To 50% Of Area 3) Occur In Over 50% Of Area
4. RANDOM OR ALLIGATOR CRACKS	1) Fine, Mostly Long Crx, No Pattern 2) Tight Crx, Patterned, Light Spalls 3) Crx, Spalled, Loose Or Severe	1) Small Area(S);Total <50 Lineal Ft 2) <25% Area (Part Of One Track) 3) >25% Area
5. TRANSVERSE AND/OR BLOCK CRACKS	1) <1/4 In.; Few Incidental; Sealed 2) >1/4 In; Small Depressed; Tight 3) Spalls; Depressed; Many Incidental	1) Avg. >= 40 Ft Space;<12 Crx In 500' 2) 20-40 Ft Space; Blx = 30-60 SFt/20' Multiple Crxs; Light Spalls > 25 Crxs Per 500' 3) Avg.<20 Ft Space; Blx Avg. <30 SFt/20'
6. LONGITUDINAL JOINTS	1) <1/4 In. Or Sealed Well 2) Moderate Random Crxs; Tight 3) Severe Spalls, Random Crxs, Open	1) < 50% Of Length 2) 50% To 90% 3) Continuous
7. EDGE CRACKING	1) Crx Tight; No Raveling Or Breaks 2) Crx Moderate; Minor Break-Up 3) Missing Pieces; Severe Crx	1) < 20% Of Length (100') 2) 20% To 50% Of Length 3) > 50% Of Length
8. WIDENING CRACKS	1) Tight Or Well Sealed,<1/I"Width 2) >1/4"; Lo Severity Random Crx Small Depressed; Light Spalls 3) Depressed; Many Random; Spalled	1) Intermittent; <25% Of Length 2) 25% To 75% Of Length 3) Nearly Continuous; >75% Of Length
9. PUMPING	Yes - Pumping Is Evident, (Moving Blocks, Ghost Fines, Mud, Etc.)	
	No - Pumping Is Not Evident	
10. MAINTENANCE	No- If Preventative Maintenance Is Not Evident (Old Or None Performed)	
	Yes-If Preventative Maintenance Is Evident (Fresh, Or New)	

APPENDIX B **PAVEMENT MANAGEMENT SYSTEM DATA**

DECREASING DIRECTION

SITE 1 I_65 MP 223_224

Road ID	Rd_From	Rd_To	Contract	Elem_ID	IRI	PCR_D	RUT AVG	Rt_ Type	ROAD	Final Cost	Suf Type	Des_No	Let_Date	Inve AADT	Year AADT	No Lane	Lane Mile
I_65	222.86	223.44	R-20369R_I_65	2002_I_65_223.0	74	100	0.07	I	I_65	6965000	R	8719125	1/12/1993	30618	2001	4	2.32
I_65	223.44	224.44	R-20369R_I_65	2002_I_65_224.0	58	87.5	0.1	I	I_65	6965000	R	8719125	1/12/1993	30618	2001	4	4
I_65	224.44	225.44	R-20369R_I_65	2002_I_65_225.0	83	84	0.09	I	I_65	6965000	R	8719125	1/12/1993	30618	2001	4	4
AVERAGE					71.67	90.5	0.08667										

SITE 2 I_65 MP 115.6_118

Road ID	Rd_From	Rd_To	Contract	Elem_ID	IRI	PCR_D	RUT AVG	Rt_ Type	ROAD	Final Cost	Suf Type	Des_No	Let_Date	Inve_AADT	Year_AADT	No_Lane	Lane_Mile
I_65	115.59	115.79	R-22177_I_65	2002_I_65_115.0	119	100	0.1	I	I_65	1.2E+07	J	8350370	11/21/1995	106015	2001	6	1.2
I_65	115.79	115.90	R-22177_I_65	2002_I_65_115.0	119	100	0.1	I	I_65	1.2E+07	J	8350370	11/21/1995	101932	2001	6	0.66
I_65	115.90	116.92	R-22177_I_65	2002_I_65_116.0	149	100	0.04	I	I_65	1.2E+07	J	8350370	11/21/1995	101932	2001	6	6.12
I_65	116.92	117.47	R-22177_I_65	2002_I_65_117.0	94	100	0.05	I	I_65	1.2E+07	J	8350370	11/21/1995	101932	2001	6	3.3
I_65	117.47	117.92	R-22177_I_65	2002_I_65_117.0	94	100	0.05	I	I_65	1.2E+07	J	8350370	11/21/1995	64541	2001	4	1.8
I_65	117.92	118.16	R-22177_I_65	2002_I_65_118.0	89	100	0.05	I	I_65	1.2E+07	J	8350370	11/21/1995	64541	2001	4	0.96
AVERAGE					110.7	100	0.065										

SITE 3 U_421MP 1_3

Road ID	Rd_From	Rd_To	Contract	Elem_ID	IRI	PCR_D	RUT AVG	Rt_ Type	ROAD	Final Cost	Suf Type	Des_No	Let_Date	Inve_AADT	Year_AADT	No_Lane	Lane_Mile
U_421	0.89	0.99	R-24208_U_421	2001_U_421_000.0	180	93	0.18	U	U_421	5348000	J	9300110	5/18/1999	13510	2001	4	0.4
U_421	0.99	1.00	R-24208_U_421	2001_U_421_000.0	180	93	0.18	U	U_421	5348000	J	9300110	5/18/1999	13510	2001	4	0.04
U_421	1.00	1.14	R-24208_U_421	2001_U_421_001.0	53	100	0.09	U	U_421	5348000	J	9300110	5/18/1999	13510	2001	4	0.56
U_421	1.14	1.59	R-24208_U_421	2001_U_421_001.0	53	100	0.09	U	U_421	5348000	J	9300110	5/18/1999	12360	2001	4	1.8
U_421	1.59	1.92	R-24208_U_421	2001_U_421_001.0	53	100	0.09	U	U_421	5348000	J	9300110	5/18/1999	12360	2001	4	1.32
U_421	1.92	2.00	R-24208_U_421	2001_U_421_001.0	53	100	0.09	U	U_421	5348000	J	9300110	5/18/1999	12360	2001	4	0.32
U_421	2.00	2.94	R-24208_U_421	2001_U_421_002.0	43	100	0.09	U	U_421	5348000	J	9300110	5/18/1999	12360	2001	4	3.76
U_421	2.94	3.00	R-24208_U_421	2001_U_421_002.0	43	100	0.09	U	U_421	5348000	J	9300110	5/18/1999	12360	2001	4	0.24
AVERAGE					82.25	98.25	0.1125										

INCREASING DIRECTION

SITE 1 I_65 MP 223_224

Road ID	Rd_From	Rd_To	Contract	Elem_ID	IRI	PCR_D	RUT AVG	Rt_ Type	ROAD	Final Cost	Suf Type	Des_No	Let_Date	Inve AADT	Year AADT	No Lane	Lane Mile
I_65	222.86	223.44	R-20369R_I_65	2002_I_65_223.0	68	99.5	0.15	I	I_65	6965000	R	8719125	1/12/1993	30618	2001	4	2.32
I_65	223.44	224.44	R-20369R_I_65	2002_I_65_224.0	62	89	0.2	I	I_65	6965000	R	8719125	1/12/1993	30618	2001	4	4
I_65	224.44	225.44	R-20369R_I_65	2002_I_65_225.0	91	91.5	0.15	I	I_65	6965000	R	8719125	1/12/1993	30618	2001	4	4
AVERAGE					73.67	93.333	0.16667										

SITE 2 I_65 MP 115.6_118

Road ID	Rd_From	Rd_To	Contract	Elem_ID	IRI	PCR_D	RUT AVG	Rt_ Type	ROAD	Final Cost	Suf Type	Des_No	Let_Date	Inve AADT	Year AADT	No Lane	Lane Mile
I_65	115.59	115.79	R-22177_I_65	2002_I_65_115.0	115	100	0.11	I	I_65	1.2E+07	J	8350370	11/21/1995	106015	2001	6	1.2
I_65	115.79	115.90	R-22177_I_65	2002_I_65_115.0	115	100	0.11	I	I_65	1.2E+07	J	8350370	11/21/1995	101932	2001	6	0.66
I_65	115.90	116.92	R-22177_I_65	2002_I_65_116.0	128	99	0.04	I	I_65	1.2E+07	J	8350370	11/21/1995	101932	2001	6	6.12
I_65	116.92	117.47	R-22177_I_65	2002_I_65_117.0	108	100	0.06	I	I_65	1.2E+07	J	8350370	11/21/1995	101932	2001	6	3.3
I_65	117.47	117.92	R-22177_I_65	2002_I_65_117.0	108	100	0.06	I	I_65	1.2E+07	J	8350370	11/21/1995	64541	2001	4	1.8
AVERAGE					114.8	99.8	0.076										

SITE 3 U_421MP 1_3

Road ID	Rd_From	Rd_To	Contract	Elem_ID	IRI	PCR_D	RUT AVG	Rt_ Type	ROAD	Final Cost	Suf Type	Des_No	Let_Date	Inve AADT	Year AADT	No Lane	Lane Mile
U_421	1.00	1.14	R-24208_U_421	2001_U_421_001.0	58	100	0.17	U	U_421	5348000	J	9300110	5/18/1999	13510	2001	4	0.56
U_421	1.14	1.59	R-24208_U_421	2001_U_421_001.0	58	100	0.17	U	U_421	5348000	J	9300110	5/18/1999	12360	2001	4	1.8
U_421	1.59	1.92	R-24208_U_421	2001_U_421_001.0	58	100	0.17	U	U_421	5348000	J	9300110	5/18/1999	12360	2001	4	1.32
U_421	1.92	2.00	R-24208_U_421	2001_U_421_001.0	58	100	0.17	U	U_421	5348000	J	9300110	5/18/1999	12360	2001	4	0.32
U_421	2.00	2.94	R-24208_U_421	2001_U_421_002.0	46	97	0.15	U	U_421	5348000	J	9300110	5/18/1999	12360	2001	4	3.76
U_421	2.94	3.00	R-24208_U_421	2001_U_421_002.0	46	97	0.15	U	U_421	5348000	J	9300110	5/18/1999	12360	2001	4	0.24
AVERAGE					54	99	0.16333										

APPENDIX C **CORE LOG IN SHEET AND LABORATORY TEST PLAN**

SITE 1- I 65 NORTH OF LAFAYETTE

LOCATION COMMENTS	ID	TOTAL HEIGHT INCHES	SURFACE THICKNESS mm	Gmb PURDUE	| G*| NCSC	|E*| PURDUE	D(t) NCSC	INDIRECT TENSILE STRENGTH NCSC	Gmm NCSC	Pb NCSC	BINDER RECOVERY NCSC	GRADATION NCSC	PEN AT 1 TEMP NCSC	SOFTENING POINT NCSC	DSR AT 5 TEMP. NCSC	DTT AT 2 TEMP NCSC
1																
CRACKED	1	11.5		NOT TAKEN												
CRACKED	2	12		NOT TAKEN												
CRACKED	3	BROKEN		NOT TAKEN												
	4	13	30.25	2.327			Rep1 -20°(	Rep1 -20°C					X	X	X	X
	5	13	31.18	2.34			Rep2 -10°(	Rep2 -10°C					X	X	X	X
	6	9	30.99	2.34			Rep3 0°(	Rep3 0°C					X	X	X	X
	7	13	25.2	2.331					Rep1	Rep1	Rep1	Rep1	X	X	X	X
	8	13	27.6	2.258		X							X	X	X	X
	9	12.5	27.4	2.278					Rep2	Rep2	Rep2	Rep2	X	X	X	X
	10	13	30.82	2.279			Rep1 -20°(	Rep1 -20°C					X	X	X	X
	11	13	27.17	2.266					Rep1	Rep1	Rep1	Rep1	X	X	X	X
	12	13	29.75	2.275		X							X	X	X	X
NOT USED	13	12	23.22	2.232												
	14	12	29.11	2.368		X							X	X	X	X
NOT USED	15	12	27.11	2.347												
2																
CRACKED	16	12		NOT TAKEN												
CRACKED	17	9		NOT TAKEN												
CRACKED	18	14		NOT TAKEN												
	19	10	22.08	2.314					Rep2	Rep2	Rep2	Rep2	X	X	X	X
	20	13	29.26	2.314		X							X	X	X	X
	21	10.3	36.09	2.327	X								X	X	X	X
	22	14	32.17	2.303			Rep2 -10°(	Rep2 -10°C					X	X	X	X
	23	13	25.02	2.292					Rep1	Rep1	Rep1	Rep1	X	X	X	X
	24	10	33.66	2.291	X								X	X	X	X
	25	12.75	29.15	2.297		X							X	X	X	X
NOT USED	26	12	24.5	2.308												
	27	11	25.83	2.311					Rep2	Rep2	Rep2	Rep2	X	X	X	X
	28	11.5	31.31	2.331			Rep3 0°(	Rep3 0°C					X	X	X	X
	29	13.5	28.7	2.318		X										
													1 TEST	2 TESTS	2 TESTS	6 TESTS
Total Samples	23 (29)				2	6	6	(6)	6	(6)	(6)	(6)	20			
Total Mix kg					2.4	7.2	7.2	(7.2)	7.2	(7.2)	(7.2)	(7.2)	24			
Binder Content kg					0.108	0.324	0.324	(0.324)	0.324	(0.324)	(0.324)	(0.324)	1.08			

Rep1-Replicate 1

Rep2-Replicate 2

SITE 2- I 65 NEAR INDIANAPOLIS

LOCATION COMMENTS	ID	TOTAL HEIGHT INCHES	SURFACE THICKNESSmm	Gmb PURDUE	| G*| NCSC	|E*| PURDUE	D(t) NCSC	INDIRECT TENSILE STRENGTH NCSC	Gmm NCSC	Pb NCSC	BINDER RECOVERY NCSC	GRADATION NCSC	PEN AT 1 TEMP NCSC	SOFTENING POINT NCSC	DSR AT 5 TEMP. NCSC	DTT AT 2 TEMP NCSC
1																
CRACKED	1	17		NOT TAKEN												
	2	17	25.26	2.293					Rep1	Rep1	Rep1	Rep1	X	X	X	X
CRACKED	3	17		NOT TAKEN												
	4	18	32.27	2.286			Rep1 -20°	Rep1 -20°C					X	X	X	X
	5	17.5	29.41	2.345		X							X	X	X	X
	6	15	34.31	2.328	X								X	X	X	X
	7	17	28.42	2.34					Rep2	Rep2	Rep2	Rep2	X	X	X	X
	8	13	29.88	2.342		X							X	X	X	X
	9	17	29.22	2.36		X							X	X	X	X
NOT USED	10	15	25.09	2.366												
	11	17	29.97	2.347		X							X	X	X	X
	12	16	27.69	2.342					Rep1	Rep1	Rep1	Rep1	X	X	X	X
NOT USED	13	9	27.71	2.338												
CRACKED	14	17														
SHOULDER	15	18	32.18	2.257												
SHOULDER	16	17.5	29.3	2.3												
2																
CRACKED	17	7.5		NOT TAKEN												
	18	7.5	30.28	2.291			Rep2 -10°	Rep2 -10°C					X	X	X	X
	19	15	29.81	2.301		X							X	X	X	X
CRACKED	20	17		NOT TAKEN												
	21	12.5	32.9	2.3			Rep3 0°	Rep3 0°C					X	X	X	X
	22	7.5	27.65	2.29					Rep2	Rep2	Rep2	Rep2	X	X	X	X
	23	12.5	33.26	2.298	X								X	X	X	X
	24	8	32.86	2.284			Rep1 -20°	Rep1 -20°C					X	X	X	X
	25	8	26.98	2.283					Rep1	Rep1	Rep1	Rep1	X	X	X	X
	26	7.5	30.76	2.3			Rep2 -10°	Rep2 -10°C					X	X	X	X
	27	13	29.62	2.297		X							X	X	X	X
CRACKED	28	13		NOT TAKEN												
	29	8.5	24.11	2.279					Rep2	Rep2	Rep2	Rep2	X	X	X	X
	30	8	30.57	2.281			Rep3 0°	Rep3 0°C					X	X	X	X
SHOULDER	31	13	28.38	2.275												
SHOULDER	32	18	29.44	2.273												
													1 TEST	2 TESTS	2 TESTS	6 TESTS
Total Samples	26 (32)				2	6	6	(6)	6	(6)	(6)	(6)	20			
Total Mix kg					2.4	7.2	7.2	(7.2)	7.2	(7.2)	(7.2)	(7.2)	24			
Binder Content kg					0.108	0.324	0.324	(0.324)	0.324	(0.324)	(0.324)	(0.324)	1.08			

Rep1-Replicate 1
Rep2-Replicate 2

SITE 3- SR 421 MADISON

LOCATION COMMENTS	ID	TOTAL HEIGHT INCHES	SURFACE THICKNES Smm	Gmb PURDUE	| G*| NCSC	|E*| PURDUE	D(t) NCSC	INDIRECT TENSILE STRENGTH NCSC	Gmm NCSC	Pb NCSC	BINDER RECOVERY NCSC	GRADATION NCSC	PEN AT 1 TEMP NCSC	SOFTENING POINT NCSC	DSR AT 5 TEMP. NCSC	DTT AT 2 TEMP NCSC
1																
CRACKED	1	8		NOT TAKEN												
CRACKED	2	7.75		NOT TAKEN												
NOT USED	3	7.75	26.06	2.24												
	4	7.5	31.04	2.233					Rep1	Rep1	Rep1	Rep1	X	X	X	X
	5	8	32.5	2.225					Rep2	Rep2	Rep2	Rep2	X	X	X	X
	6	7.5	38.01	2.226			Rep1 -20°	Rep1 -20°C					X	X	X	X
	7	7.25	33.79	2.233		X							X	X	X	X
	8	7	29.86	2.23					Rep1	Rep1	Rep1	Rep1	X	X	X	X
	9	7	27.72	2.235					Rep2	Rep2	Rep2	Rep2	X	X	X	X
	10	7.75	35.2	2.266		X							X	X	X	X
	11	7.5	33.18	2.245		X							X	X	X	X
NOT USED	12	7.25	30.86	2.239												
	13	7	34.11	2.243		X							X	X	X	X
NOT USED	14	7	31.63	2.24												
SHOULDER	15	10.5	41.21	2.264												
SHOULDER	16	10.5	44.19	2.284												
2																
CRACKED	17	7.5		NOT TAKEN												
CRACKED	18	8		NOT TAKEN												
	19	8.5	38.44	2.163			Rep2 -10°	Rep2 -10°C					X	X	X	X
	20	8.5	47.81	2.183	X								X	X	X	X
CRACKED	21	7.75		NOT TAKEN												
	22	7.5	39.2	2.177			Rep3 0°	Rep3 0°C					X	X	X	X
	23	7.5	49.4	2.185	X								X	X	X	X
	24	7.2	40.26	2.185					Rep1	Rep1	Rep1	Rep1	X	X	X	X
	25	7.5	39.56	2.178			Rep2 -10°	Rep2 -10°C					X	X	X	X
	26	7	40.49	2.179			Rep1 -20°	Rep1 -20°C					X	X	X	X
	27	7.25	35.39	2.227					Rep2	Rep2	Rep2	Rep2	X	X	X	X
	28	6.5	37.35	2.223		X							X	X	X	X
	29	7	38.64	2.224			Rep3 0°	Rep3 0°C					X	X	X	X
	30	7	37.35	2.221		X							X	X	X	X
SHOULDER	31	10	42.6	2.234												
SHOULDER	32	9.75	40.57	2.248												
													1 TEST	2 TESTS	2 TESTS	6 TESTS
Total Samples	25 (32)				2	6	6	(6)	6	(6)	(6)	(6)	20			
Total Mix kg					2.4	7.2	7.2	(7.2)	7.2	(7.2)	(7.2)	(7.2)	24			
Binder Content kg					0.108	0.324	0.324	(0.324)	0.324	(0.324)	(0.324)	(0.324)	1.08			

Rep1-Replicate 1

Rep2-Replicate 2

APPENDIX D **LABORATORY TEST RESULTS**

PERCENTAGE AIR VOIDS

Site 1 I-65 North of Lafayette

SAMPLE ID	Gmb PURDUE	Gmm NCSC	% Air Voids	Average % Air Voids
1	NOT TAKEN	2.486		
2	NOT TAKEN	2.486		
3	NOT TAKEN	2.486		
4	2.327	2.486	6.40	
5	2.340	2.486	5.87	6.10
6	2.340	2.486	5.87	
7	2.331	2.486	6.23	
8	2.258	2.486	9.17	
9	2.278	2.486	8.37	
10	2.279	2.486	8.33	8.64
11	2.266	2.486	8.85	
12	2.275	2.486	8.49	
13	2.232	2.486	10.22	
14	2.368	2.486	4.75	6.85
15	2.347	2.486	5.59	
16	NOT TAKEN	2.486		
17	NOT TAKEN	2.486		
18	NOT TAKEN	2.486		
19	2.314	2.486	6.92	
20	2.314	2.486	6.92	6.74
21	2.327	2.486	6.40	
22	2.303	2.486	7.36	
23	2.292	2.486	7.80	7.65
24	2.291	2.486	7.84	
25	2.297	2.486	7.60	
26	2.308	2.486	7.16	
27	2.311	2.486	7.04	6.80
28	2.331	2.486	6.23	
29	2.318	2.486	6.76	

where:

	LWP	Left Wheel Path
	CENTER	Center
	RWP	Right Wheel Path

Site 2 I-65 Near Indianapolis

SAMPLE ID	Gmb PURDUE	Gmm NCSC	% Air Voids	Average % Air Voids
1	NOT TAKEN	2.502		
2	2.293	2.502	8.35	8.49
3	NOT TAKEN	2.502		
4	2.286	2.502	8.63	
5	2.345	2.502	6.27	6.35
6	2.328	2.502	6.95	
7	2.340	2.502	6.47	
8	2.342	2.502	6.39	
9	2.360	2.502	5.68	
10	2.366	2.502	5.44	6.15
11	2.347	2.502	6.20	
12	2.342	2.502	6.39	
13	2.338	2.502	6.55	
14	NOT TAKEN	2.502		
15	2.257	2.502	9.79	8.93
16	2.300	2.502	8.07	
17	NOT TAKEN	2.502		
18	2.291	2.502	8.43	8.23
19	2.301	2.502	8.03	
20	NOT TAKEN	2.502		
21	2.300	2.502	8.07	8.43
22	2.290	2.502	8.47	
23	2.298	2.502	8.15	
24	2.284	2.502	8.71	
25	2.283	2.502	8.75	
26	2.300	2.502	8.07	8.50
27	2.297	2.502	8.19	
28	NOT TAKEN	2.502		
29	2.279	2.502	8.91	
30	2.281	2.502	8.83	
31	2.275	2.502	9.07	9.11
32	2.273	2.502	9.15	

where:

	LWP	Left Wheel Path
	CENTER	Center
	RWP	Right Wheel Path
	SHOULDER	Shoulder

Site 3 SR421 Madison

ID	Gmb PURDUE	Gmm NCSC	% Air Voids	Average % Air Voids
1	NOT TAKEN	-		
2	NOT TAKEN	-		
3	2.240	2.458	8.87	
4	2.233	2.458	9.15	9.32
5	2.225	2.458	9.48	
6	2.226	2.458	9.44	
7	2.233	2.458	9.15	
8	2.230	2.458	9.28	8.95
9	2.235	2.458	9.07	
10	2.266	2.458	7.81	
11	2.245	2.458	8.67	
12	2.239	2.458	8.91	8.81
13	2.243	2.458	8.75	
14	2.240	2.458	8.87	
15	2.264	2.458	7.89	7.49
16	2.284	2.458	7.08	
17	NOT TAKEN	-		
18	NOT TAKEN	-		
19	2.163	2.458	12.00	11.59
20	2.183	2.458	11.19	
21	NOT TAKEN			
22	2.177	2.458	11.43	
23	2.185	2.458	11.11	
24	2.185	2.458	11.11	11.28
25	2.178	2.458	11.39	
26	2.179	2.458	11.35	
27	2.227	2.458	9.40	
28	2.223	2.458	9.56	9.53
29	2.224	2.458	9.52	
30	2.221	2.458	9.64	
31	2.234	2.458	9.11	8.83
32	2.248	2.458	8.54	

where:

	LWP	Left Wheel Path
	CENTER	Center
	RWP	Right Wheel Path
	SHOULDER	Shoulder

EXTRACTION OF BINDER CONTENT (AASHTO TP 2)

REPLICATE	SITE 1 I-65 NORTH	SITE2 I-65 INDIANAPOLIS	SITE3 US-421 MADISON
1	4.90	5.90	6.30
2	5.30	6.30	6.10
3	5.80	5.30	6.40
4	5.50	6.00	6.20
Average	5.38	5.88	6.25
Std Dev	0.38	0.42	0.13
CV%	7.0	7.1	2.1

GRADATION DATA (AASHTO TP 11, 27)

SIZE		SITE 1			SITE 2			SITE 3		
inch	mm	R 1	Rp 2	Avg.	R 1	R 2	Avg.	R 1	R 2	Avg.
3/4	**19**	100.0	100.0	100.0	100.0	100.0	100.0	100.0	100.0	100.0
1/2	**12.5**	96.7	100.0	98.3	100.0	100.0	100.0	100.0	100.0	100.0
3/8	**9.5**	87.7	94.2	90.9	94.7	91.7	93.2	95.7	94.9	95.3
# 4	**4.75**	51.0	61.8	56.4	63.0	56.7	59.8	66.6	63.3	64.9
# 8	**2.36**	35.5	44.9	40.2	47.4	41.7	44.6	48.1	44.3	46.2
#16	**1.18**	29.0	35.7	32.3	30.5	27.7	29.1	34.5	31.1	32.8
#30	**0.6**	23.2	27.3	25.2	20.8	19.3	20.0	20.6	18.6	19.6
#50	**0.3**	12.3	12.3	12.3	14.6	13.4	14.0	7.8	7.3	7.6
#100	**0.15**	5.0	4.5	4.8	9.4	9.0	9.2	3.9	3.1	3.5
# 200	**0.075**	3.1	2.7	2.9	5.8	5.8	5.8	2.9	2.0	2.5

APPENDIX E **DYNAMIC SHEAR RHEOMETER (DSR) TEST**

Site 1 I-65 North of Lafayette

	15°C		25°C		35°C		40°C		52°C		64°C		76°C	
Freq. Hz	δ °	|G*|, Pa	δ °	|G*|, Pa	δ °	|G*|, Pa	δ °	|G*|, Pa	δ °	|G*|, Pa	δ °	|G*|, Pa	δ °	|G*|, Pa
0.1	43.8	7.72E+06	55.2	1.46E+06	64.4	2.31E+05	45.7	1.67E+06	65.3	3.32E+05	74.6	6.34E+04	81.1	1.47E+04
0.1	43	8.66E+06	54.4	1.69E+06	63.8	2.74E+05	47.3	1.50E+06	65.8	2.87E+05	75.1	5.34E+04	81.2	1.22E+04
0.2	42.1	9.59E+06	53.4	1.91E+06	63.1	3.21E+05	49	1.32E+06	66.6	2.39E+05	75.5	4.39E+04	81.4	9.65E+03
0.2	41.2	1.06E+07	52.6	2.19E+06	62.4	3.81E+05	50.8	1.16E+06	67.3	2.02E+05	75.8	3.63E+04	82	7.92E+03
0.3	40.5	1.18E+07	51.9	2.50E+06	61.7	4.42E+05	52.3	1.01E+06	67.8	1.69E+05	76.3	2.98E+04	82.3	6.42E+03
0.3	40	1.31E+07	51.3	2.86E+06	61.1	5.21E+05	53.8	8.84E+05	68.6	1.41E+05	76.9	2.46E+04	82.8	5.27E+03
0.4	39.1	1.44E+07	50.4	3.23E+06	60.4	6.12E+05	55.3	7.63E+05	69.3	1.18E+05	77.5	2.01E+04	83	4.26E+03
0.5	38.5	1.58E+07	49.8	3.65E+06	59.8	7.14E+05	56.4	6.62E+05	70.1	9.83E+04	77.9	1.65E+04	83.4	3.38E+03
0.6	37.8	1.74E+07	49	4.13E+06	59.2	8.37E+05	58.3	5.73E+05	71	8.11E+04	78.6	1.35E+04	83.9	2.72E+03
0.8	37.1	1.92E+07	48.2	4.68E+06	58.5	9.70E+05	59.1	4.90E+05	71.3	6.72E+04	79.1	1.10E+04	84.1	2.17E+03
1.0	36.6	2.10E+07	47.5	5.30E+06	57.9	1.12E+06	60.3	4.21E+05	71.7	5.58E+04	79.7	8.97E+03	84.6	1.74E+03
1.3	35.9	2.30E+07	46.9	5.96E+06	57.2	1.29E+06	62.1	3.59E+05	72.7	4.67E+04	80.4	7.33E+03	84.7	1.38E+03
1.6	35.3	2.51E+07	46.2	6.71E+06	56.6	1.50E+06	63.1	3.06E+05	73.6	3.83E+04	81	5.96E+03	84.9	1.10E+03
2.0	34.8	2.73E+07	45.5	7.51E+06	55.9	1.72E+06	63.6	2.60E+05	74	3.15E+04	81.4	4.83E+03	85.3	8.78E+02
2.5	34.2	2.98E+07	44.9	8.40E+06	55.4	1.97E+06	64.2	2.19E+05	74.5	2.61E+04	81.8	3.89E+03	85.6	7.01E+02
3.2	33.7	3.24E+07	44.3	9.40E+06	54.8	2.26E+06	70.7	1.58E+05	75.3	2.14E+04	82.4	3.17E+03	86.1	5.64E+02
4.0	33.3	3.50E+07	43.8	1.04E+07	54.2	2.58E+06	66.1	1.44E+05	75.9	1.78E+04	83	2.55E+03	85.8	4.56E+02
5.1	32.8	3.80E+07	43.3	1.16E+07	53.7	2.97E+06	66.5	1.21E+05	76.8	1.48E+04	83.7	2.07E+03	86.5	3.70E+02
6.4	32.5	4.09E+07	42.8	1.29E+07	53.2	3.37E+06	68	1.03E+05	77.6	1.19E+04	84.3	1.66E+03	86.1	2.97E+02
8.1	32.2	4.41E+07	42.5	1.42E+07	52.8	3.83E+06	68.5	8.64E+04	78.1	9.78E+03	84.2	1.35E+03	87	2.37E+02
10.0	32.1	4.69E+07	42.3	1.55E+07	52.5	4.28E+06	69.5	7.38E+04	79.1	8.07E+03	85	1.07E+03	86.7	1.92E+02

Site 2 I-65 Loop near Indianapolis

	15°C		25°C		35°C		40°C		52°C		64°C		76°C	
Freq. Hz	δ °	|G*|, Pa	δ °	|G*|, Pa	δ °	|G*|, Pa	δ °	|G*|, Pa	δ °	|G*|, Pa	δ °	|G*|, Pa	δ °	|G*|, Pa
0.1	52.1	5.47E+06	65.7	8.27E+05	75.5	1.10E+05	54.5	1.43E+06	73.8	2.57E+05	82	43663	85.6	9211.4
0.1	50.8	6.29E+06	64.7	9.81E+05	74.8	1.34E+05	56.3	1.25E+06	74.5	2.17E+05	82.4	36178	86	7558.4
0.2	49.7	7.13E+06	63.8	1.15E+06	74	1.62E+05	58.3	1.07E+06	75.3	1.81E+05	82.6	29195	86.3	6014.3
0.2	48.7	8.11E+06	62.6	1.36E+06	73.3	1.97E+05	60.1	9.20E+05	75.9	1.49E+05	83.1	23782	86.5	4849.2
0.3	47.6	9.14E+06	61.7	1.59E+06	72.5	2.38E+05	61.9	7.84E+05	76.4	1.22E+05	83.3	19012	86.8	3847.9
0.3	46.5	1.04E+07	60.8	1.87E+06	71.8	2.85E+05	63.6	6.67E+05	77.1	1.01E+05	83.5	15573	87.2	3102.6
0.4	45.6	1.16E+07	59.8	2.17E+06	70.9	3.46E+05	65.2	5.61E+05	77.8	8.24E+04	84.3	12447	87.2	2455.8
0.5	44.7	1.30E+07	58.8	2.51E+06	70.2	4.20E+05	66.9	4.72E+05	78.5	6.84E+04	84.7	10094	87.7	1953.2
0.6	43.8	1.46E+07	57.9	2.91E+06	69.4	5.03E+05	67.6	3.94E+05	79.2	5.54E+04	84.9	8061.8	87.5	1568.4
0.8	42.8	1.63E+07	56.7	3.39E+06	68.7	5.98E+05	69.5	3.34E+05	79.8	4.49E+04	85.3	6513.5	87.7	1255.6
1.0	41.9	1.81E+07	56.1	3.91E+06	67.8	7.05E+05	70.3	2.78E+05	80.6	3.61E+04	85.5	5160.7	87.7	1008
1.3	41	2.00E+07	55	4.51E+06	67.1	8.40E+05	71.4	2.30E+05	81.6	2.92E+04	86.6	4157.4	88.3	801.78
1.6	40.2	2.22E+07	54.1	5.20E+06	66.3	9.89E+05	72.6	1.79E+05	82.1	2.34E+04	85.8	3294.3	88.3	638.24
2.0	39.2	2.45E+07	53.2	5.93E+06	65.5	1.18E+06	73.4	1.51E+05	82.3	1.84E+04	86.7	2655.2	88.2	504.8
2.5	38.6	2.70E+07	52.2	6.77E+06	64.7	1.39E+06	74.2	1.31E+05	82.9	1.51E+04	86.9	2111.6	87.6	402.66
3.2	37.8	2.97E+07	51.3	7.76E+06	64	1.64E+06	76	1.06E+05	83.3	1.20E+04	87.2	1696.7	87.7	322.85
4.0	37.2	3.24E+07	50.5	8.79E+06	63.1	1.92E+06	75.8	8.58E+04	84	9.46E+03	87.7	1343.8	89.3	257.37
5.1	36.5	3.56E+07	49.7	1.00E+07	62.3	2.26E+06	76.8	6.97E+04	84.2	7.74E+03	88.2	1081	88.4	202.55
6.4	35.9	3.87E+07	49	1.13E+07	61.5	2.63E+06	77.7	5.83E+04	84.4	6.26E+03	87.9	872.54	88.1	162.23
8.1	35.4	4.23E+07	48.3	1.28E+07	60.8	3.06E+06	79	4.72E+04	84.9	5.02E+03	88.2	693.19	87.3	129.39
10.0	35	4.56E+07	47.8	1.42E+07	60.2	3.51E+06	79.4	3.91E+04	85.3	4.09E+03	88.1	551.22	85.7	107.74

Site 3 SR 421 Madison

	15°C		25°C		35°C		40°C		52°C		64°C		76°C	
Freq. Hz	δ °	|G*|, Pa	δ °	|G*|, Pa	δ °	|G*|, Pa	δ °	|G*|, Pa	δ °	|G*|, Pa	δ °	|G*|, Pa	δ °	|G*|, Pa
0.1	50.1	6.45E+06	60	1.07E+06	65.2	1.88E+05	54.7	7.19E+05	65.9	3.17E+05	73.9	6.97E+04	79.3	1.60E+04
0.1	48.9	7.30E+06	59.3	1.26E+06	66.5	2.16E+05	53.1	1.06E+06	66.4	2.75E+05	74.2	5.90E+04	79.5	1.33E+04
0.2	48.3	8.33E+06	58.6	1.46E+06	65	2.58E+05	56.2	7.65E+05	67	2.32E+05	74.5	4.91E+04	79.9	1.08E+04
0.2	47.5	9.34E+06	58	1.71E+06	65.8	3.03E+05	55.9	8.56E+05	67.6	1.96E+05	74.9	4.08E+04	80.3	8.95E+03
0.3	46.7	1.06E+07	57.3	1.97E+06	64.9	3.59E+05	55.2	8.29E+05	68.2	1.64E+05	75.3	3.32E+04	80.8	7.17E+03
0.3	45.7	1.18E+07	56.9	2.28E+06	64.1	4.25E+05	56	7.44E+05	68.7	1.38E+05	75.8	2.73E+04	81.2	5.87E+03
0.4	45	1.33E+07	56.1	2.65E+06	63.6	5.00E+05	57.5	6.44E+05	69.3	1.16E+05	76.3	2.25E+04	81.5	4.68E+03
0.5	44.3	1.49E+07	55.2	3.07E+06	63.6	5.86E+05	58.9	5.53E+05	70	9.65E+04	76.8	1.88E+04	82.1	3.75E+03
0.6	43.5	1.66E+07	54.8	3.55E+06	63.3	6.92E+05	60	4.74E+05	70.6	8.07E+04	77.3	1.53E+04	82.3	3.04E+03
0.8	42.8	1.85E+07	54.1	4.08E+06	62.7	8.13E+05	61.1	4.05E+05	71.1	6.74E+04	77.9	1.24E+04	82.8	2.46E+03
1.0	41.9	2.05E+07	53.3	4.64E+06	62.1	9.49E+05	62.2	3.46E+05	71.8	5.62E+04	78.6	1.02E+04	83.2	1.97E+03
1.3	41.2	2.28E+07	52.6	5.31E+06	61.6	1.11E+06	63.2	2.95E+05	72.4	4.67E+04	79.1	8.29E+03	83.8	1.58E+03
1.6	40.4	2.52E+07	51.9	6.06E+06	61	1.30E+06	64.1	2.50E+05	73	3.87E+04	79.6	6.75E+03	84.6	1.27E+03
2.0	39.6	2.79E+07	51.3	6.90E+06	60.7	1.52E+06	65.1	2.11E+05	73.6	3.21E+04	80.3	5.44E+03	84.3	1.02E+03
2.5	39	3.08E+07	50.5	7.83E+06	60.1	1.78E+06	65.3	1.79E+05	74.3	2.66E+04	80.8	4.48E+03	85.4	8.28E+02
3.2	38.3	3.39E+07	49.8	8.89E+06	59.5	2.08E+06	66.2	1.50E+05	75	2.20E+04	81.4	3.62E+03	85.9	6.55E+02
4.0	37.6	3.71E+07	49.2	1.00E+07	59.1	2.41E+06	66.5	1.27E+05	75.5	1.83E+04	82	2.96E+03	85.6	5.28E+02
5.1	37.1	4.08E+07	48.6	1.14E+07	58.6	2.81E+06	68.2	1.07E+05	76.1	1.52E+04	82.8	2.42E+03	86.1	4.25E+02
6.4	36.6	4.45E+07	48.1	1.28E+07	58.2	3.24E+06	69.1	9.08E+04	77	1.25E+04	83.3	1.94E+03	86	3.38E+02
8.1	36.1	4.86E+07	47.5	1.44E+07	57.6	3.76E+06	70	7.56E+04	77.3	1.02E+04	83.5	1.56E+03	85.8	2.68E+02
10.0	35.8	5.25E+07	47.2	1.60E+07	57.3	4.27E+06	70	6.27E+04	78.4	8.33E+03	84	1.25E+03	85.4	2.18E+02

APPENDIX F **DIRECT TENSION TEST (DTT) RESULTS**

SITE 1: Temperatures -12C and -18C

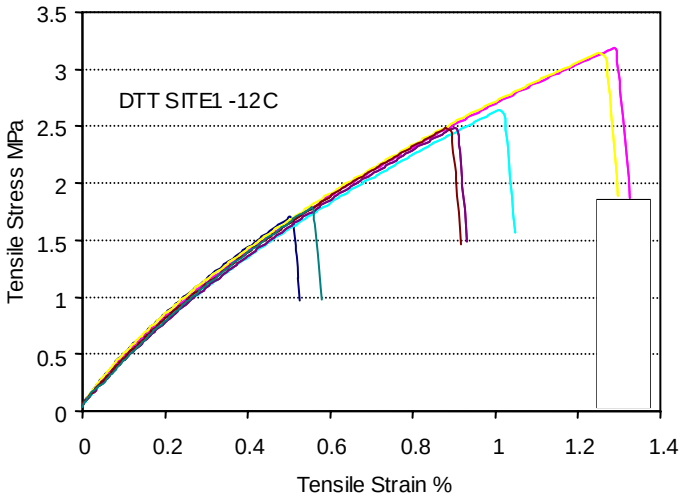

SITE 1 I-65 North		
ID at Temp -12C	Failure Stress MPa	Failure strain %
1	1.703294	0.502797
2	3.187621	1.287613
3	3.147023	1.252174
4	2.645618	1.010377
5	2.490269	0.901994
6	2.490352	0.881179
7	1.79721	0.555919
Mean	2.494484	0.913151

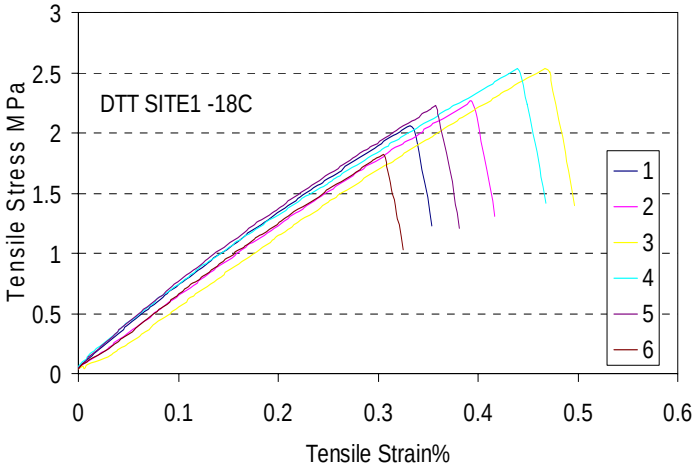

SITE 1 I-65 North		
ID at Temp -18C	Failure Stress MPa	Failure strain%
1	2.059681	0.33165
2	2.262697	0.393433
3	2.537155	0.466703
4	2.533204	0.439791
5	2.225107	0.357509
6	1.822014	0.305531
Mean	2.239976	0.382436

SITE 2 Temperatures -6C, -12C, -18C

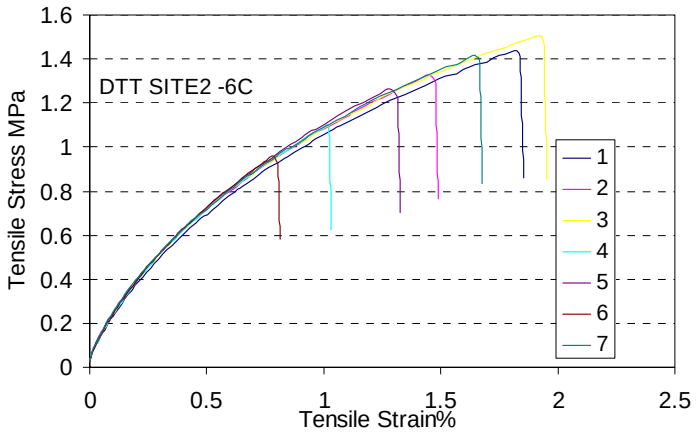

SITE 2 I-65 Near Indianapolis		
ID at Temp -6C	Failure Stress MPa	Failure strain%
1	1.435298	1.825386
2	1.325078	1.450567
3	1.504072	1.921219
4	1.103136	1.017019
5	1.263794	1.283285
6	0.961639	0.785552
7	1.415897	1.647857
Mean	1.286988	1.418698

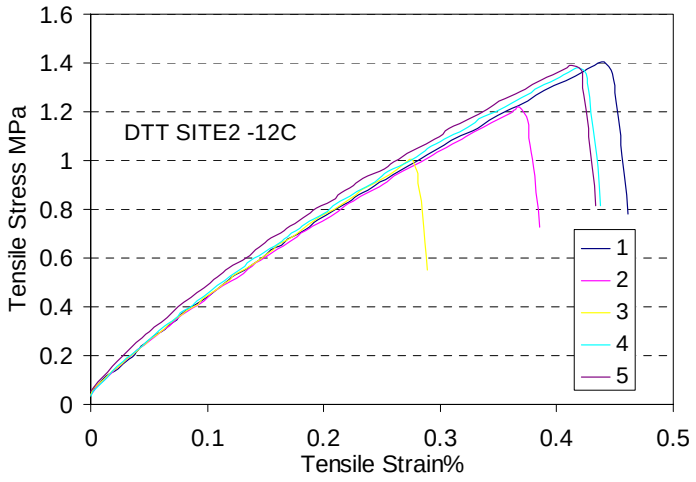

SITE 2 I-65 Near Indianapolis		
ID at Temp -12C	Failure Stress MPa	Failure strain %
1	1.407077	0.440505
2	1.217456	0.368083
3	1.003811	0.275518
4	1.382099	0.419399
5	1.39263	0.413386
Mean	1.280615	0.383378

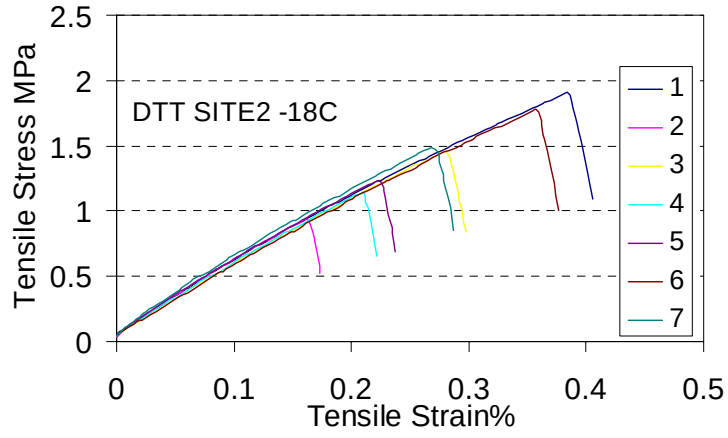

SITE 2 I-65 Near Indianapolis		
ID at Temp -18C	Failure Stress MPa	Failure strain %
1	1.910702	0.384306
2	0.94328	0.162486
3	1.46094	0.280168
4	1.150818	0.209945
5	1.236903	0.222403
6	1.776509	0.357244
7	1.489895	0.268611
Mean	1.42415	0.269309

SITE 3 Temperatures -6C, -12C

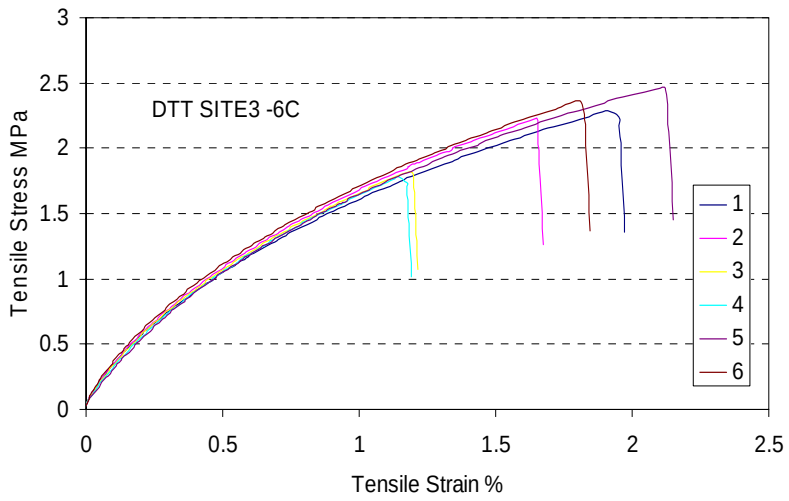

SITE 3 US 421 Madison		
ID at Temp -6C	Failure Stress MPa	Failure strain %
1	2.285131	1.910515
2	2.229543	1.649013
3	1.825678	1.185909
4	1.781526	1.143525
5	2.470648	2.116252
6	2.361202	1.807163
Mean	2.158955	1.635396

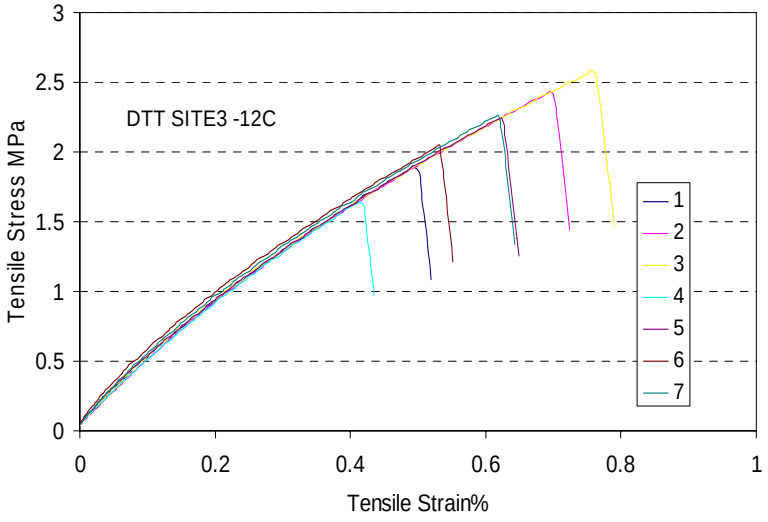

SITE 3 US421 Madison		
ID at Temp -12C	Failure Stress MPa	Failure strain %
1	1.895401	0.492446
2	2.431826	0.696413
3	2.581209	0.756
4	1.643681	0.413199
5	2.248731	0.622951
6	2.049198	0.531916
7	2.266441	0.618468
Mean	2.159498	0.590199

APPENDIX G **SST SHEAR FREQUENCY SWEEP TEST RESULTS**

SITE 1: I-65 North of Lafayette

	4°C		10°C		20°C		40°C		55°C	
Freq. Hz	δ °	|G*|, psi	δ °	|G*|, psi	δ °	|G*|, psi	δ °	|G*|, psi	δ °	|G*|, psi
10.0	10.48	724,741	13.25	595,315	16.74	407,709	40.50	107,257	56.48	22,796
5.0	8.44	672,737	10.40	584,442	16.64	359,649	41.38	80,366	56.17	15,674
2.0	7.83	628,966	10.13	533,659	17.98	307,964	43.77	53,696	52.39	9,600
1.0	8.18	593,639	10.97	497,431	19.11	270,712	45.45	38,466	50.39	6,818
0.5	9.00	559,966	12.31	454,695	20.92	233,436	46.69	27,402	44.81	4,910
0.2	9.86	506,277	13.88	399,016	24.20	188,688	47.25	17,193	42.05	3,718
0.1	11.36	467,858	15.30	358,439	25.94	157,593	46.21	12,560	37.67	2,896
0.1	12.79	430,027	17.65	318,891	28.44	129,586	45.30	8,673	32.07	2,203
0.0	14.53	375,715	19.79	267,113	32.19	97,115	42.26	5,577	20.70	2,274
0.0	15.85	340,502	22.57	230,749	35.58	74,691	40.06	4,384	33.28	1,799

Site 2 I-65 Loop near Indianapolis

	4°C		10°C		20°C		40°C		55°C	
Freq. Hz	δ °	|G*|, psi	δ °	|G*|, psi	δ °	|G*|, psi	δ °	|G*|, psi	δ °	|G*|, psi
10.0	14.59	435,557	13.20	565,666	16.78	417,768	36.47	128,729	53.50	29,214
5.0	13.03	397,557	11.38	500,808	16.17	364,422	37.06	101,815	53.20	21,302
2.0	13.94	365,362	10.45	466,784	16.91	315,189	39.73	72,612	51.12	13,682
1.0	13.42	340,389	10.96	434,096	18.58	275,303	41.46	54,848	46.99	9,885
0.5	13.03	318,603	11.83	405,033	20.04	240,363	41.87	40,489	43.66	7,438
0.2	13.51	291,933	13.46	356,753	22.80	196,178	41.63	27,662	38.82	5,377
0.1	13.89	273,537	14.83	320,474	24.94	164,752	40.65	20,493	26.31	3,711
0.1	15.28	254,097	16.66	286,045	26.59	136,356	37.97	16,171	27.70	3,717
0.0	16.31	234,206	19.55	239,716	31.26	102,306	37.34	10,810	29.13	3,325
0.0	17.93	220,674	22.26	203,255	33.84	78,877	35.12	8,668	20.16	2,002

Site 3 SR 421 Madison

	4°C		10°C		20°C		40°C		55°C	
Freq. Hz	δ °	|G*|, psi	δ °	|G*|, psi	δ °	|G*|, psi	δ °	|G*|, psi	δ °	|G*|, psi
10.0	16.37	689,877			18.22	410,118	39.73	117,006	61.55	17,031
5.0	13.43	626,917			17.10	365,835	41.68	91,748	59.52	12,158
2.0	11.74	575,704			17.84	312,822	45.38	64,468	60.49	7,377
1.0	11.45	543,231			19.73	274,874	48.92	46,224	57.05	5,091
0.5	11.93	509,581			21.87	242,152	51.67	32,515	57.79	3,460
0.2	13.41	463,449			25.29	197,403	51.97	21,051	55.95	2,374
0.1	14.67	425,805			28.01	165,699	51.53	15,140	47.26	1,550
0.1	16.58	385,473			31.48	136,119	51.12	10,786	45.28	1,176
0.0	18.79	333,039			36.23	101,518	50.91	7,106	41.37	1,217
0.0	20.86	291,964			39.85	77,924	47.41	4,899	41.66	903